# PHOTODISINTEGRATION OF HELIUM-3 AT ENERGIES BETWEEN 200 AND 600 MEV

Thesis by

Kirk T. McDonald

In Partial Fulfillment of the Requirements

for the Degree of

Doctor of Philosophy

California Institute of Technology

Pasadena, California

1972

(Submitted May 24, 1972)

ACKNOWLEDGEMENTS

One of the pleasures of this experiment has been the opportunity to work together with many outstanding people.

My greatest debt is to Clemens Heusch who, as my adviser, has had a pervasive and salutary influence on all aspects of this long experiment, from its conception to the final analysis.

The business of conducting an experiment was taught to me by Charles Prescott.

The construction of the apparatus was primarily due to the craftsmanship of Walter Nilsson. The experiment also benefitted from the advice and services of engineers Bill Friedler, Hans Grau, Dan Sell and Joe Ungerer. Barry Lieberman assisted in the construction of special electronics.

The happy tedium of collecting the data was shared by my colleagues Steve Cheng, Bob Kline, Bill McNeely, Bruce Winstein and Steve Yellin.

The contributions of Steve Cheng, Charles Prescott and Leon Rochester to the data analysis are mentioned in the text. Duane Edgington and Greg Stewart assisted in computer programming. Abe Seiden has made important contributions to the interpretation of the results. The spirit of liberation was brought to the data analysis by Ms. Phyllis Nilsson.

This experiment was performed at the Caltech synchrotron during the final months of its life. The machine was successfully nursed through this period by the operators: Al Neubeiser, Joe Laurinovics, Frank

Scarlino and George Ynclan, and by the maintenance crew: Paul Van-Ligten, Danny Heffington, Art Schmidt and George Talbert.

The $He^3$ target was provided by Victor Perez-Mendez with the technical assistance of Don Hunt. It was kept running smoothly by Earl Emery and Dick Wileman.

The production of the thesis was aided by Judi Laurence.

For financial support, I am indebted to the Atomic Energy Commission, the National Science Foundation, and the United States Steel Foundation.

Concurrent for me with this experiment was another, with Nancy Schaefer. Are they not of the same conception? To be alive one must feel the irreversibility of time. "There are moments when you think you see her grow old and feel yourself growing old with her...If I remember correctly, they call that the irreversibility of time." (Jean-Paul Sartre)

## ABSTRACT

We have measured differential cross-sections for the two-body photodisintegration of Helium-3, $\gamma + He^3 \rightarrow p + d$, between incident photon energies of 200 and 600 MeV, and for center of mass frame angles between $30^\circ$ and $150^\circ$. Both final state particles were detected in arrays of wire spark chambers and scintillation counters; the high momentum particle was analyzed in a magnet spectrometer. The results are interpreted in terms of amplitudes to produce the $\Delta(1236)$ resonance in an intermediate state, as well as non-resonant amplitudes. This experiment, together with an (unfinished) experiment on the inverse reaction, $p + d \rightarrow He^3 + \gamma$, will provide a reciprocity test of time reversal invariance.

TABLE OF CONTENTS

# LIST OF FIGURES

# LIST OF TABLES

To the memory of my father, James E. McDonald.

# I. INTRODUCTION

We have measured the differential cross-section for the two body photodisintegration of Helium-3, $\gamma + He^3 \rightarrow p + d$. The incident photon energy was between 200 and 600 MeV and the scattering angles varied from $30^\circ$ to $150^\circ$ in the center of mass frame. The energy range includes the region in which the first nucleon resonance, the $\Delta(1236)$, can be produced in an intermediate state.

Past studies of this reaction have been conducted almost exclusively at photon energies below 150 MeV. This work is reviewed in Appendix A. Data on the related process, the electrodisintegration of $He^3$, are discussed in Appendix B.

The present experiment on $\gamma + He^3 \rightarrow p + d$ is intimately related to a study of the inverse reaction, $p + d \rightarrow He^3 + \gamma$. The cross-sections for these two reactions must obey a simple relation (given below) in their center of mass frame as a consequence of time reversal invariance.

The discovery [1] in 1964 of a violation of the combined symmetry CP (charge conjugation and parity) in the decays of the neutral K mesons has stimulated the search for a violation of time reversal invariance (T). Such a violation is to be expected, given a CP violation, according to the CPT Theorem [2] which claims that all physical processes are invariant under the combined transformation of C, P, and T. In particular, Bernstein, Feinberg and Lee [3] noted that the experimental evidence for T-invariance in the electromagnetic interaction was very scanty. This is partly due to the fact that in many experiments a time

reversal violation would also imply a parity violation, or non-hermiticity or non-conservation of the electromagnetic current. The evidence against these effects is considerably greater [4]. We shall not review the present experimental status nor the variety of experiments proposed to test T-invariance. A comprehensive review through 1969 has been given by Henley [5].

The method of investigation of T-invariance which concerns this experiment is a test of detailed balance. In general, if T-invariance is true, then the cross-sections of the forward and reverse reactions $a + b \leftrightarrow c + d$ must be related by

$$\frac{d\sigma}{d\Omega_c}(a + b \to c + d) = \frac{(2S_c + 1)(2S_d + 1)}{(2S_a + 1)(2S_b + 1} \frac{P_c^2}{P_a^2} \frac{d\sigma}{d\Omega_a}(c + d \to a + b)$$

evaluated in the center of mass frame. Barshay [6] in 1966 suggested that the reaction $\gamma + d \to n + p$ would be a good place to look for a T-violation. The source of any potential T-violation would involve a $\gamma N\Delta(1236)$ vertex. This is known to contribute strongly to $\gamma + d \to n + p$ as a resonance 'bump' appears in the cross-section near photon energies of 300 MeV. It is necessary to consider the $\gamma N\Delta$ vertex rather than the simpler $\gamma NN$ vertex because the requirements that the electromagnetic current is conserved, and that it conserves parity, forbid any T-violation here.

A time reversal violation at the $\gamma N\Delta$ vertex might manifest itself in either (or both) of two ways. If the magnitude of the coupling constant is different for $\gamma + N \to \Delta$ than for $\Delta \to \gamma + N$, then the total cross-sections of the forward and reverse reactions will be

different. However, the experimental difficulty in making a precise absolute normalization of a photon beam intensity might simulate such an effect. Any evidence for an electromagnetic T-violation based solely on a discrepancy between total cross-sections should be regarded warily.

The second possibility is that the phase of the coupling constant may be different for $\gamma + N \rightarrow \Delta$ than for $\Delta \rightarrow N + \gamma$. Then if the amplitude to produce the $\Delta$ interferes with a T-invariant amplitude, such as one involving the $\gamma NN$ vertex, the shape of the differential cross-section may be noticeably different for the forward and reverse reactions. Experiments which investigate this possibility are not sensitive to errors in the absolute normalization of the cross-sections.

Barshay proposed a search for this type of effect. He noted that the cross-section for $\gamma + d \rightarrow n + p$ in the region of the $\Delta$ resonance has contributions of about 60% from the transition $E1 \rightarrow {}^3P_0$, 36% from $M1 \rightarrow {}^1D_2$ and 4% from $M1 \rightarrow {}^1S_0$. The $\Delta$ is produced in the $M1 \rightarrow {}^1D_2$ transition, which can interfere with any non-resonant part of the same amplitude, or also with the $M1 \rightarrow {}^1S_0$ amplitude. However, it cannot interfere with the strong $E1 \rightarrow {}^3P_0$ transition as the total spins of the final states are different. Thus, any T-violation is somewhat suppressed as it must appear in the interference between a strong T-violating amplitude and a weak T-conserving amplitude. Nonetheless, a maximal violation could cause the ratio $A_2/A_0$ to differ by as much as 0.3 between the forward and reverse reactions, presuming the differential

cross-section to be of the form

$$A_0 + A_2 P_2 (\cos\theta).$$

$P_2$ is the second order Legendre polynomial.

For completeness, we note that there exist models of a possible T-violation of the electromagnetic current which suggest that the $\gamma N\Delta$ vertex will be T-invariant, the violation appearing elsewhere. Lee [7] and later Okun [8] consider that the T-violation is due to the existence of certain as yet unobserved particles whose strong interactions are not charge conjugation invariant. This leads to an electromagnetic T-violation which, however, conserves isotopic spin. Since the $\gamma N\Delta$ vertex involves a change by one of the hadron isospin, it would be T-invariant. The second argument, due to Frazer [9], is that the static model bootstrap description of the reaction $\gamma N \to \Delta \to N\pi$ requires it to be T-invariant. This reaction appears as part of the most reasonable mechanism for $\Delta$ production in $\gamma + d \to n + p$, so the latter reaction should be T-invariant also.

Turning to the experimental situation regarding $\gamma + d \leftrightarrow n + p$, we find that the forward reaction has been reasonably well-studied at energies suitable for $\Delta$ production [10-14]. Investigation of the inverse reaction was stimulated by Barshay's work. The reaction is difficult because of the background reaction $n + p \to d + \pi^o \to d + \gamma + \gamma$, which has a cross-section roughly seventy times that of $n + p \to d + \gamma$. The first $n + p$ experiment [15] claimed a 2.5 standard deviation effect in the discrepancy of the ratio $A_2/A_0$ compared to the $\gamma + d$ reaction. At

the time the present experiment was proposed (1969), the preliminary analysis of a second n + p experiment[16] showed a similar, if slightly smaller effect. Since that time, the first experiment has been redone[17], reducing troublesome spark chamber inefficiencies, and the analysis completed on the second[18]; as a result, the effect has disappeared. The latter experiment reports the T-violating phase as 4 ± 10 degrees.

Within the last year, the interest in reciprocity tests of T-invariance has shifted from reactions $\gamma + d \leftrightarrow n + p$ to $\gamma + n \leftrightarrow p + \pi^-$. While the latter are perhaps conceptually simpler than the former, they are more difficult experimentally. The $\gamma$+ n reaction must be performed with a deuterium target and corrections made for the 'spectator' proton. The $\pi^- + p$ reaction has an all neutral final state, and is subject to large backgrounds from $n + \pi^o$ final states. There are sizable discrepancies between the data on the forward and reverse reactions, which might indicate a T-violation. The difficulty of the experiments makes it hard to draw firm conclusions at present, and more precise data are needed to clarify the situation. Donnachie[19] has given a recent review of this complex problem, including a good bibliography.

We come at length to consider the present experiment. In 1969, when the data on $\gamma + d \rightarrow n + p$ were consistent with a T-violation, the reactions $\gamma + He^3 \leftrightarrow p + d$ were proposed as a good place to verify or disprove the effect.

The reaction $\gamma + He^3 \rightarrow p + d$ is slightly more complicated than $\gamma + d \rightarrow n + p$ because there exists the 3-body breakup reaction $\gamma + He^3 \rightarrow p + p + n$. This can be suppressed by requiring a deuteron to be observed

in the final state. An actual advantage is that both final state particles are charged and can easily be detected, allowing the elimination of backgrounds due to pion production, such as $\gamma + He^3 \rightarrow d + n + \pi^+$.

The inverse reaction, $p + d \rightarrow He^3 + \gamma$ is studied with a charged proton (or deuteron!) beam which can be made with good momentum definition. This provides an important additional constraint to eliminate the background process $p + d \rightarrow He^3 + \pi^o$, $(\pi^o \rightarrow \gamma\gamma)$. The lack of the extra constraint is a weak point of the $n + p \rightarrow d + \gamma$ experiments (which was, however, somewhat rectified in the second Princeton experiment[17]).

A kinematic disadvantage of the p + d reaction is that the $He^3$ is produced with fairly low kinetic energies. Since it is doubly charged, it subsequently loses energy rapidly via multiple Coulomb scattering. If a deuteron beam and a proton target were used, the $He^3$ kinetic energies would be much greater in the laboratory for a given center of mass frame energy (see Appendix I for a more complete discussion).

Some additional features of the reactions $\gamma + He^3 \leftrightarrow p + d$ which must be considered are as follows. First, the cross-section[78] is about a factor of ten lower than that for $\gamma + d \leftrightarrow n + p$, requiring more time to reach a given accuracy. Second, $He^3$ might have an excited state, $He^{3*}$, which would decay to the ground state with the emission of a photon. Such a state could be produced by $p + d \rightarrow He^{3*} + \gamma$ with roughly equal probability as $p + d \rightarrow He^3 + \gamma$. The $He^{3*}$, or subsequent $He^3$ after decay, might lead to a final configuration indistinguishable in the experimental apparatus from an $He^3$ produced in the desired reaction. Thus the recipro-

city between the forward and reverse reactions could be destroyed without a T-violation. Apparently, the three nucleon system is the only multi-nucleon system with no known excited states, either bound or virtual.[20]

A third significant feature is that the excitation of the $\Delta(1236)$ does not appear to have such a pronounced effect on $\gamma + He^3 \leftrightarrow p + d$ as on $\gamma + d \leftrightarrow n + p$. The only existing data[78] at energies above 200 MeV are $90^o$ (c.m.) differential cross-sections. These are shown in Figure 1.1 and indicate at most a broad rise near 300 MeV above the cross-section as extrapolated from lower energies. It is of course possible that the $\Delta$ contribution to the $90^o$ cross-section is small. The lack of a 'bump' can also be attributed to the fact that isospin conservation requires any intermediate state which contains a $\Delta$ to have all three baryons unbound with respect to one another; that is, the two non-resonant nucleons may not form a spectator deuteron. The relative kinetic energies of the three baryons smear the cross-section for $\Delta$ production towards higher photon energies. As discussed in more detail in Appendix C, the smearing might be as much as 100 MeV.

Recall that for the reciprocity test to have significance independent of absolute normalizations of the cross-sections, the interference between the $\Delta$-producing amplitude and some T-invariant amplitude must be large. As discussed in Appendix C, even at energies near threshold several amplitudes contribute to $\gamma + He^3 \rightarrow p + d$. Likewise, a $\Delta$ could be produced in several amplitudes. This is a favorable situation in that there are more possibilities for interference. Specific models (Appendix C) predict the most likely amplitudes for $\Delta$ production are magnetic dipole

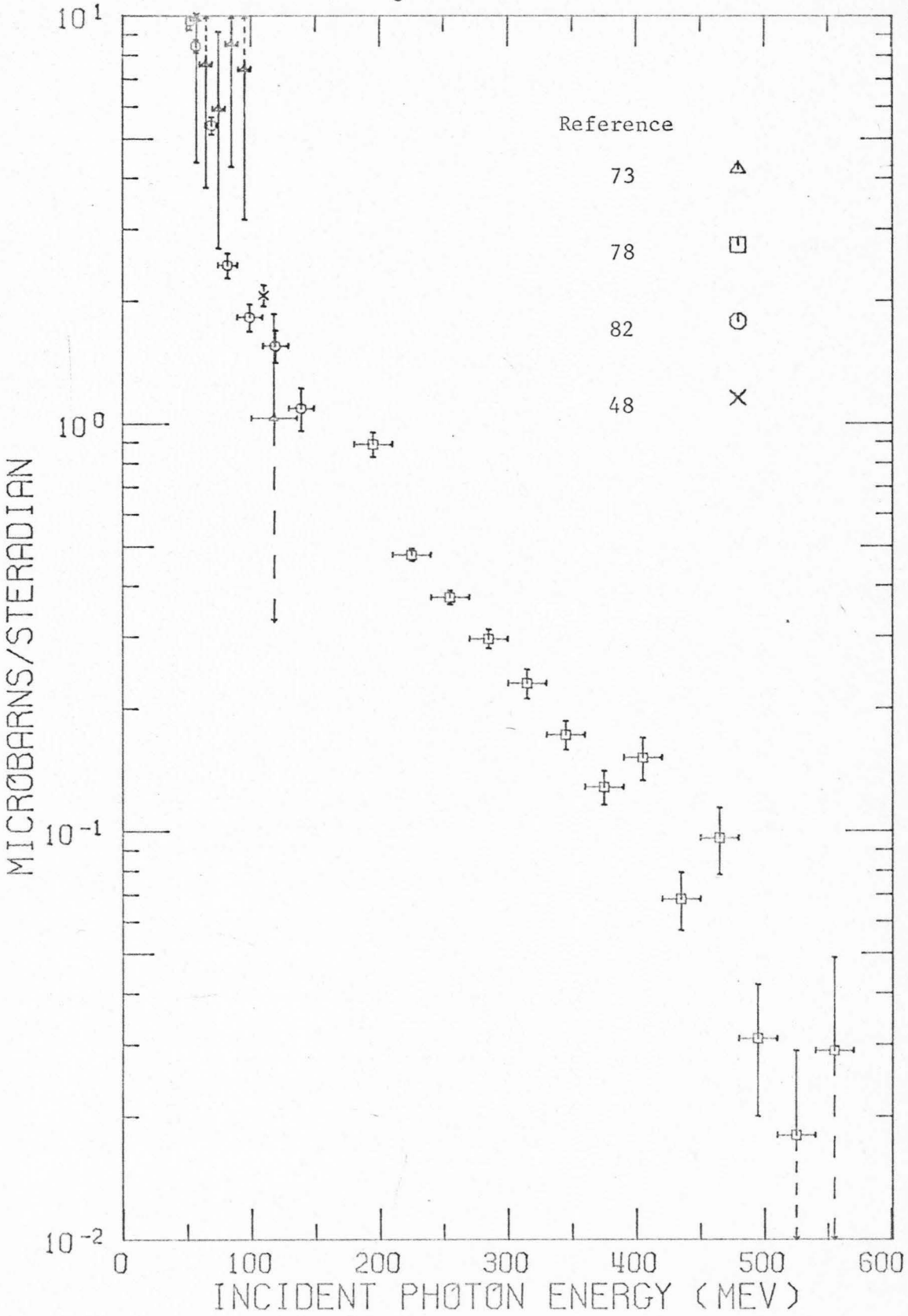


Figure 1.1 Existing Cross-Section Data on $\gamma + He^3 \rightarrow p + d$ at $90^o$(c.m.)

transitions leading to either a $^4S_{3/2}$ or a $^2D_{3/2}$ state of the p + d system. Most of the cross-section at energies below 200 MeV is due to transitions to doublet final spin states. If this trend applies to the T-invariant part of the cross-section above 200 MeV, the transition to the $^2D_{3/2}$ could be small and still have a large interference term. Indeed, the interference effect in $\gamma + He^3 \rightarrow p + d$ might well be stronger than in $\gamma + d \rightarrow n + p$.

At the time this experiment was proposed, other groups had stated their plans to restudy $n + d \rightarrow d + \gamma$. Rather than duplicate these efforts, we desired to provide an independent check on the then currently observed failure of the reciprocity test. The reactions $\gamma + He^3 \leftrightarrow p + d$ have qualitatively equal, and perhaps even greater, sensitivity to a possible T-violation. They also enjoy the advantage of cleaner background separation in both the forward and reverse reactions.

Independent of any considerations of T-invariance, measurement of $\gamma + He^3 \leftrightarrow p + d$ at $\Delta$ production energies would extend the study of the three-nucleon problem to a new kinematic region. While this problem is sufficiently complicated at low energies, we may hope for simplifications when the energy of the probe (i.e., photon) is large compared to the binding energy of the nucleons.

We have therefore investigated both reactions $\gamma + He^3 \leftrightarrow p + d$ at energies near 300 MeV above threshold (in the center of mass frame). This thesis reports the measurement of the differential cross-section of the reaction $\gamma + He^3 \rightarrow p + d$ for incident photon energies between 200

and 600 MeV. The experiment was performed at the Caltech 1.5 GeV electron synchrotron. The inverse experiment has been performed at the 184 inch cyclotron of the Lawrence Berkeley Laboratory*. The data from the inverse reaction are not yet completely analyzed and will be reported elsewhere.

* Formerly the Lawrence Radiation Laboratory.

## II. EXPERIMENTAL METHOD

In this experiment we wished to measure the differential cross-section of the reaction $\gamma + He^3 \rightarrow p + d$ at energies such that an intermediate state might contain the $\Delta(1236)$ nucleon resonance. This could occur with photons of energies around 300 MeV hitting a stationary $He^3$ target. In view of time and cost limitations, we measured cross-sections at center of mass angles $30^o$, $60^o$, $90^o$, $120^o$ and $150^o$, and to lesser precision, at $75^o$ and $105^o$, for incident photon energies between 200 and 600 MeV.

The main features of the experimental method were:

1. High energy bremsstrahlung photons were produced at the Caltech 1.5 GeV electron synchrotron.

2. The photons were incident on a target of liquid $He^3$.

3. Both the proton and the deuteron produced by the reaction $\gamma + He^3 \rightarrow p + d$ were observed in wire spark chamber arrays.

4. The spark chambers were triggered by an appropriate coincidence of signals from scintillation counters interspersed among the spark chambers.

5. One of the arrays also contained a bending magnet, yielding a precise measurement of the momentum of the detected particle; also measured was the time of flight of the particle in the array.

6. The data were recorded on magnetic tape using an on-line PDP 5 computer.

Section A of this chapter contains a discussion of the motivation

of the choice of technique, followed by a more detailed description of the apparatus and procedures in Sections B and C. The data collected are summarized in Section D.

A. The Choice of Techniques

The only copious source of high energy photons is the bremsstrahlung of high energy charged particles, which produces a beam of intensity inversely proportional to the photon energy. We used the bremsstrahlung beam of the Caltech synchrotron.

As the cross-section of $\gamma + He^3 \rightarrow p + d$ was expected to be low, it was important to take advantage of the greater density of a liquid target as opposed to a gaseous one. This involves some technical difficulty as $He^3$ has the lowest liquefying temperature of any known substance. We were fortunate in obtaining a condensation-type liquid $He^3$ target on loan from the Lawrence Berkeley Laboratory.

The final state of our reaction contains two particles. As the energy of the photon initiating the reaction was not known, two quantities must be measured in the final state to provide a complete description of the reaction (assuming definite masses for the final state particles). Rather than observe the energy and angle of only one of the particles, both particles were observed. This is important more for the suppression of backgrounds due to three particle final states than for measurement of the desired reaction.

The laboratory production angles of both particles and the momentum of one were measured, thus over-determining the description of a two-particle final state by one quantity. The particles' azimuthal angles play no part in the description of a two-body final state except that they must differ by $180^{\circ}$. This need not be so when only two particles are detected out of a three-body state.

The angles were measured in wire chamber arrays, one for each particle. This technique offered the advantages of good angular resolution and computerized processing of the data. One particle was momentum analyzed in a magnet placed behind the wire chambers. To make full use of the magnet's aperture, a second set of wire chambers was placed behind the magnet. With the observation of two angles and a momentum, there are two independent constraints which can be used to eliminate backgrounds.

Scintillation counters were used to trigger the spark chambers and to help identify the particles. For the latter purpose, the pulse heights of the signals from several of the counters were measured for each event. Additionally, the length of the magnet and its array of chambers and counters was sufficient for a measurement of the time of flight of the particle through this array.

A very important feature of the experimental method outlined above was that all of the data could be processed by an on-line computer and recorded onto magnetic tape. A detailed description of each event was obtained without photographic techniques, making it possible for subsequent data analysis to be performed by only one person.

B. Apparatus

This experiment was performed in the 'south' beam of the synchrotron. The photon beam was produced by the bremsstrahlung of the 700 MeV circulating electron beam striking an internal target of 0.2 radiation lengths of tantalum. The details of the photon beam spectrum are discussed in Appendix D. There were two beam pulses per second with a duty cycle of 12%.

Figure 2.1 shows the layout of the beam. The beam was collimated to a cone of angle roughly three milliradians by the two lead collimators. Charged particles were removed from the beams by two magnets: the "radar" magnet, which deflected particles vertically, followed by the "sweep" magnet, which deflected horizontally. The sweep magnet was immediately followed by a four inch lead wall to absorb the swept particles. A helium bag (to reduce pair production) extended from the first lead wall to a second lead wall eighteen inches before the $He^3$ target. The apertures of the lead walls were considerably larger than the beam cross-section. For runs with the magnet spectrometer at the most forward angles, a lead pipe three inches in diameter was placed between the second lead wall and the target to suppress the spray of charged particles, mostly electrons, at small angles.

The length of this beam was thirty-three feet from the tantalum target to the $He^3$ target. The beam spot at the target was 2-3/8 inches in diameter. The beam was thus 5.9 milliradians in diameter.

The beam was continuously monitored by observing the current output of a thick plate ion chamber intercepting the beam about thirty

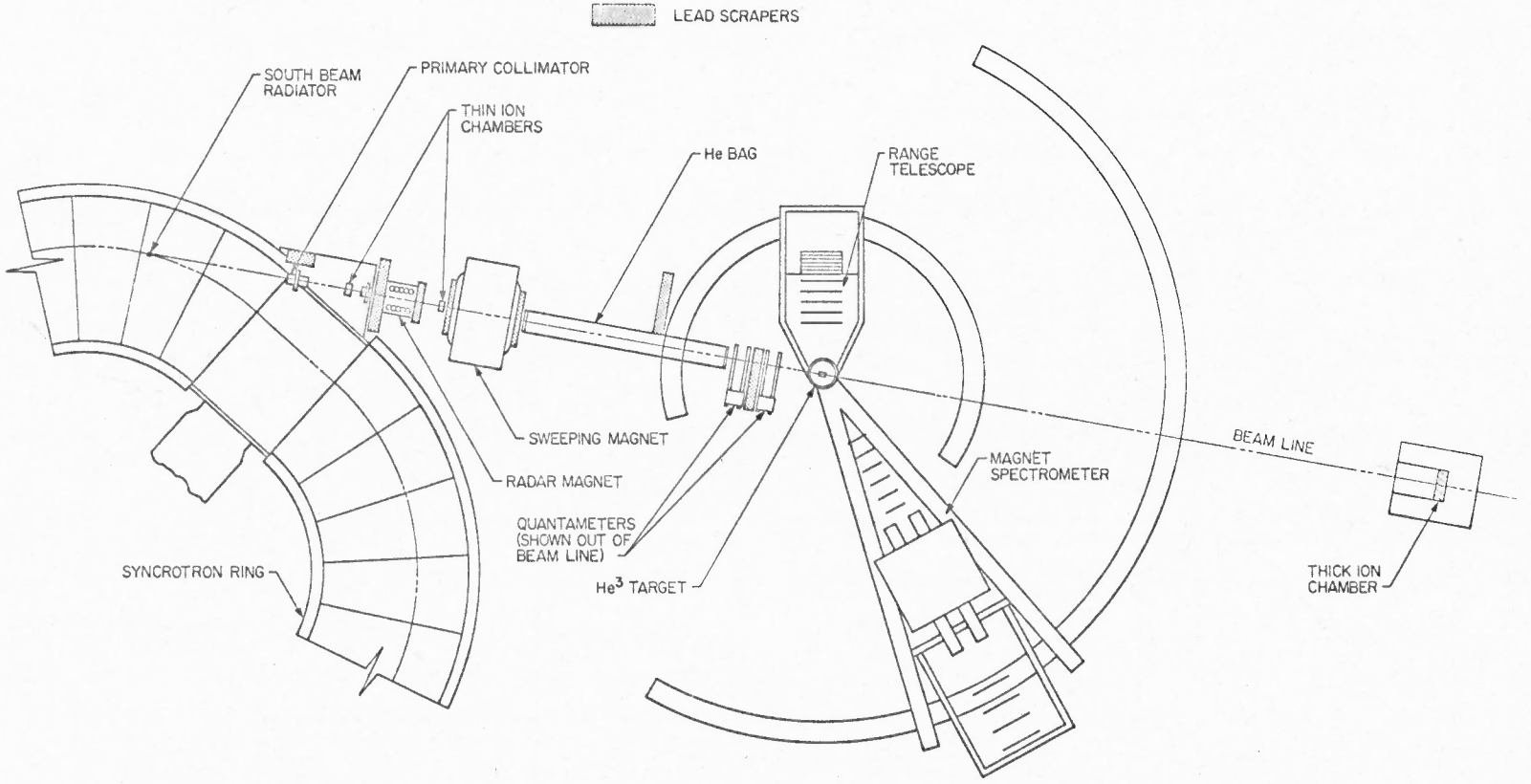


Figure 2.1 Layout of the Experiment

feet downstream of the $He^3$ target. A detailed discussion of the use and calibration of this beam monitor is given in Appendix E.

The target was a cylinder four inches long and three inches in diameter containing liquid $He^3$. Its axis was along the beam line. The $He^3$ was condensed at the expense of evaporation of liquid $He^4$. Details of the operation and monitoring of the target are given in Appendix F.

As outlined above, the final state particles were detected in two arrays of wire spark chambers and scintillation counters. They are called the magnet and range[21] arrays and are illustrated in Figures 2.2 and 2.4 respectively. The measurement of the complete angular distribution of the reaction $\gamma + He^3 \rightarrow p + d$ required the detectors to be placed at angles ranging from $20^o$ to $145^o$ to the beam. The magnet array was limited by space to angles less than $90^o$. It was used to detect whichever of the proton or deuteron had the smaller laboratory angle. The range array was used to detect the other particle, be it deuteron or proton, produced at large angles.

The elements of the magnet array were four scintillation counters (made of NE102) and ten wire chambers, mounted six in front of and four behind the magnet. A lead wall shielded all but the central region of the detectors from the spray of particles emanating from the target. At times, a plastic absorber was placed over the cutout in the lead wall to further reduce the spray. Various dimensions of the array elements are listed in Table 2.1.

The bending magnet deflected positively charged particles down-

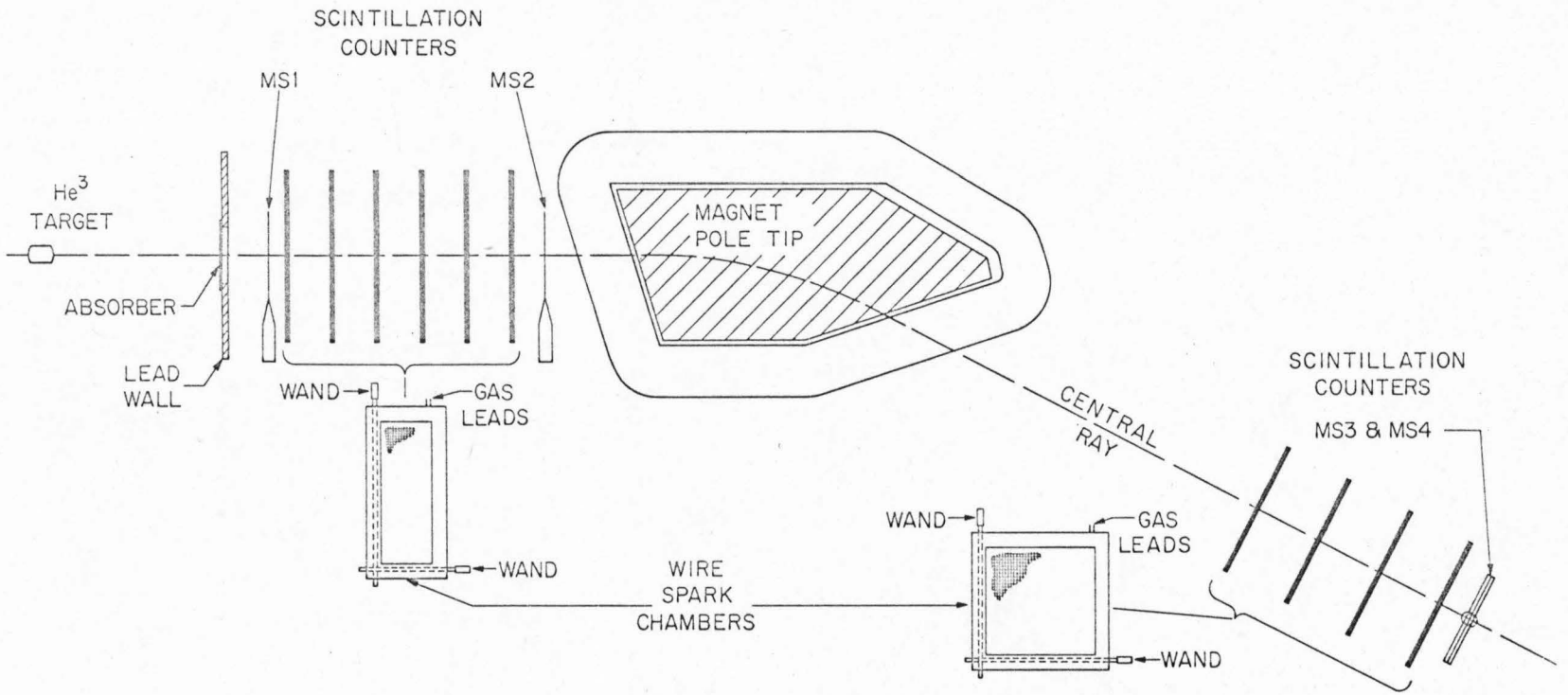


Figure 2.2 The Magnet Array

Table 2.1

Elements of the Magnet Array

| | Height (inches) | Width (inches) | Thickness (inches) | Distance From $He^3$ Target (inches) |
|---|---|---|---|---|
| Plastic Absorber | 10 | 6 | 0, ¼, ½ | 31 |
| Lead Wall Cutout | 10 | 6 | 1 | 32 |
| Scintillator MS1 | 15 | 15 | ¼ | 40 |
| Wire Chamber 1 | 25 | 9 | 0.34 | 43 |
| Wire Chamber 2 | " | 9 | " | 51 |
| Wire Chamber 3 | " | 9 | " | 59 |
| Wire Chamber 4 | " | 9 | " | 67 |
| Wire Chamber 5 | " | 9 | " | 75 |
| Wire Chamber 6 | " | 9 | " | 83 |
| Scintillator MS2 | 16 | 4 | ¼ | 90 |
| Wire Chamber 7 | 19 | 19 | 0.34 | 177 |
| Wire Chamber 8 | " | 19 | " | 189 |
| Wire Chamber 9 | " | 19 | " | 201 |
| Wire Chamber 10 | " | 19 | " | 213 |
| Scintillator MS3 | 19 | 19 | 3/4 | 217 |
| Scintillator MS4 | " | 19 | " | 218 |

ward in the laboratory. The angle of bend of the central ray was $27^{o}$. The gap between the magnet pole tips was four inches wide. The magnet and its array of chambers were mounted on a trolley which could be rotated about a vertical axis through the $He^{3}$ target (see Figure 2.1). During the experiment, the trolley was placed at twenty settings ranging from $23^{o}$ to $82^{o}$ with respect to the photon beam.

The signature of a particle in the magnet array was a coincidence of pulses from all four magnet scintillations counters, with appropriate allowance for the time of flight of the particle. However, the kinetic energies of the protons and deuterons were low, so that in certain cases, generally at larger angles, the particles may be absorbed in counter MS3. A coincidence of only counters MS1, 2 and 3 was required in these cases.

As a check on the identity of the particle in the magnet array, its time of flight between counters MS1 and MS3 was measured. An appropriate bias on the time of flight excluded pions, and clearly distinguished protons from deuterons. Figure 2.3 shows a typical time of flight spectrum for a run in which both protons and deuterons were observed in the magnet.

For further identification of the particles, the signal pulse heights in counters MS3 and MS4 were digitized and recorded (cf. Section C).

The spark chambers consisted of two planes of wires, yielding x-y coordinate information. The wires were spaced twenty-five to the

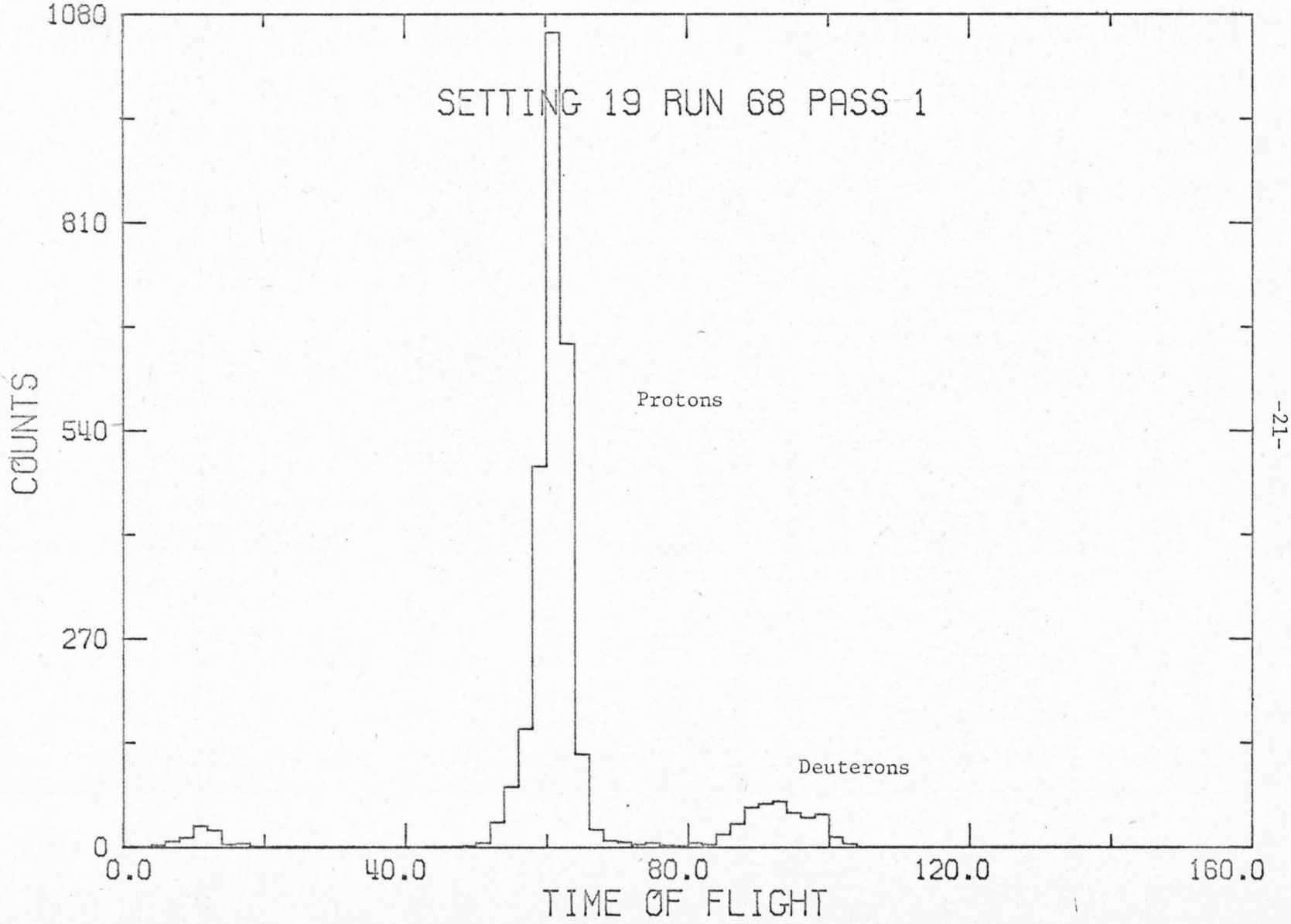


Figure 2.3 A Typical Time-of-Flight Spectrum

inch, with a gap of 0.34" between planes. They were operated at 10 KV with a gas mixture of 90% neon-10% helium and a small amount of alcohol as a quenching agent. The gas was purified and recirculated by two Lawrence Berkeley Laboratory spark chamber gas purifiers. The sparks in the wire chambers in front (i.e., upstream) of the magnet served to define a straight line along a particle's trajectory, thus determining its polar and azimuthal angle with respect to the photon beam. The additional chambers behind the magnet defined a second line. These two lines, together with the magnetic field strength, determined the particle's momentum. Multiple Coulomb scattering limited the accuracy to 0.5 - 1.5%, depending on the setting. The method of the momentum calibration is described in Appendix G.

The second particle in the final state was detected in the range array. This array was also mounted on a trolley, and was set at angles from $75^{\circ}$ to $145^{\circ}$ to the photon beam in the course of the experiment. A lead wall with a square aperture was followed by five wire spark chambers and three scintillation counters. The wire chambers were identical to those behind the magnet. Various dimensions of the array elements are listed in Table 2.2.

The signature of a particle in the range array depended on the particle's kinetic energy. When low, only RS1 or RS1·RS2 was required for a trigger. To insure that there were sufficient sparks to form a reliable line, counter RS1 was mounted after the fourth chamber.

To identify the particles in the range array, the pulse heights

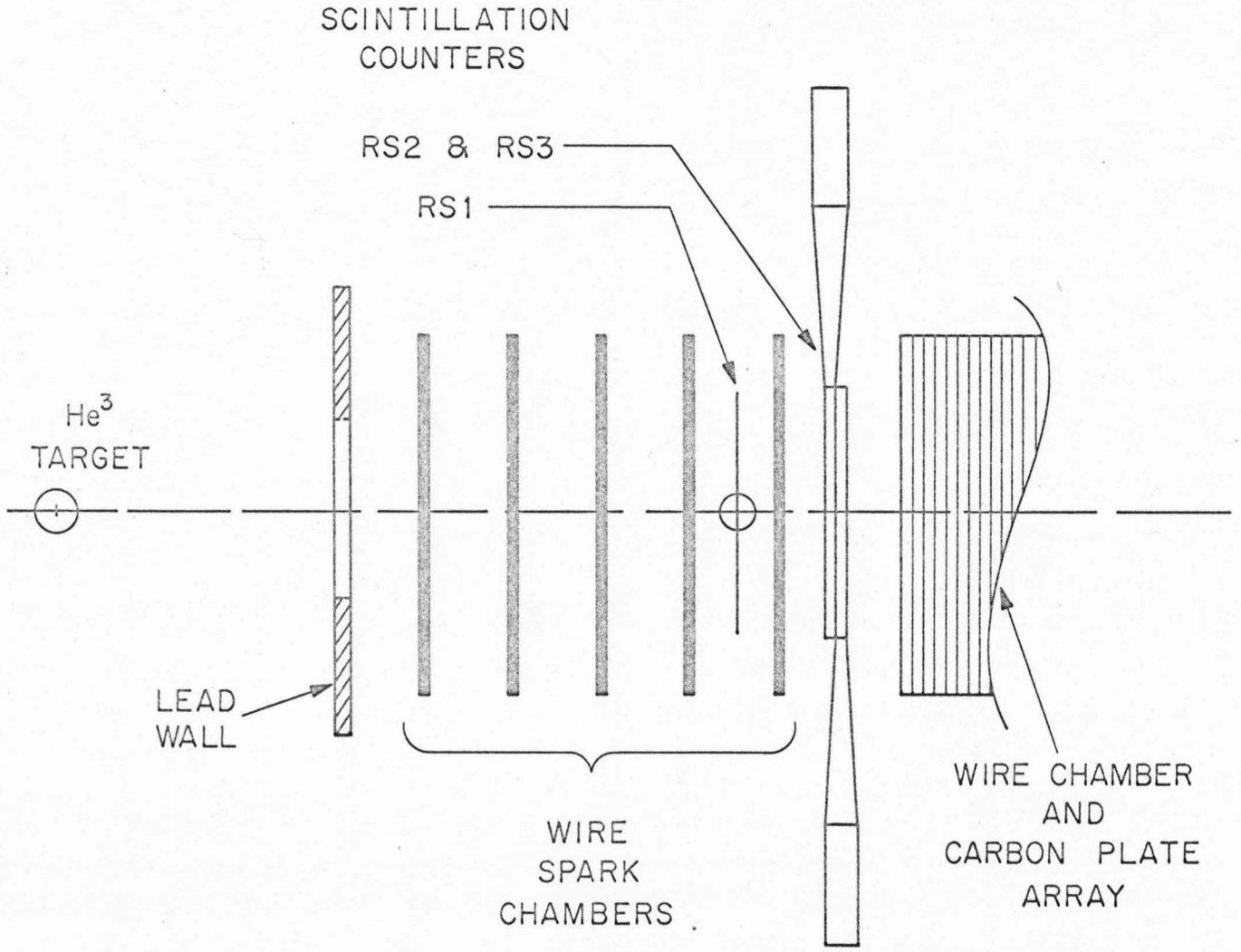


Figure 2.4 The Range Array

Table 2.2

Elements of the Range Array

| | Height (inches) | Width (inches) | Thickness (inches) | Distance From $He^3$ Target (inches) |
|---|---|---|---|---|
| Plastic Absorber | 12 | 12 | 0, 1/8, ¼ | 19 |
| Lead Wall Cutout | 12 | 12 | 1 | 20 |
| Wire Chamber 1 | 19 | 19 | 0.34 | 25 |
| Wire Chamber 2 | " | 19 | " | 31 |
| Wire Chamber 3 | " | 19 | " | 37 |
| Wire Chamber 4 | " | 19 | " | 43 |
| Scintillator RS1 | 17 | 17 | ¼ | 47 |
| Wire Chamber 5 | 19 | 19 | 0.34 | 49 |
| Scintillator RS2 | 19 | 19 | 3/4 | 53 |
| Scintillator RS3 | " | 19 | " | 54 |

of the signals of all three counters were measured and recorded.

The signature of an event, for which the chambers were pulsed, was the coincidence of the separate signatures described above.

C. Electronics

The electronics used in this experiment served two purposes: to indicate the presence of candidates for a $\gamma + He^3 \rightarrow p + d$ event and to record onto magnetic tape the data associated with such an event.

A block diagram of the electronics used to define an event is shown in Figure 2.5. Most of the circuits, labelled LIM, DISC, etc., were designed and built at Caltech. Table 2.3 relates the abbreviations used in Figure 2.5 (and Figure 2.6) to the names of the circuits as described in references 22 and 23.

The basic signature of an event is the coincidence of signals from the seven scintillation counters RS1-3 and MS1-4. As mentioned above in Section B, counters RS2, RS3 and MS4 were not used in some runs, and hence left out of the coincidence. Two more signals were required to complete this coincidence. The 'beam gate' signal was used to suppress events of cosmic ray origin. Finally, a 'veto' signal indicated that an event had not occurred within the last 0.2 seconds, allowing the spark chambers time to recover. As the beam gate signal was only about 0.1 second long, the electronics allowed at most one coincidence per beam pulse of the synchrotron.

The output signal from a master coincidence initiated the recording of an event: it triggered the spark chambers, pulse height analyzers, and the computer. It also inhibited the scalers observing the scintillation counting rates and the beam monitors during the mandatory 0.2 second dead-time following an event. Therefore, no corrections were needed for this dead-time.

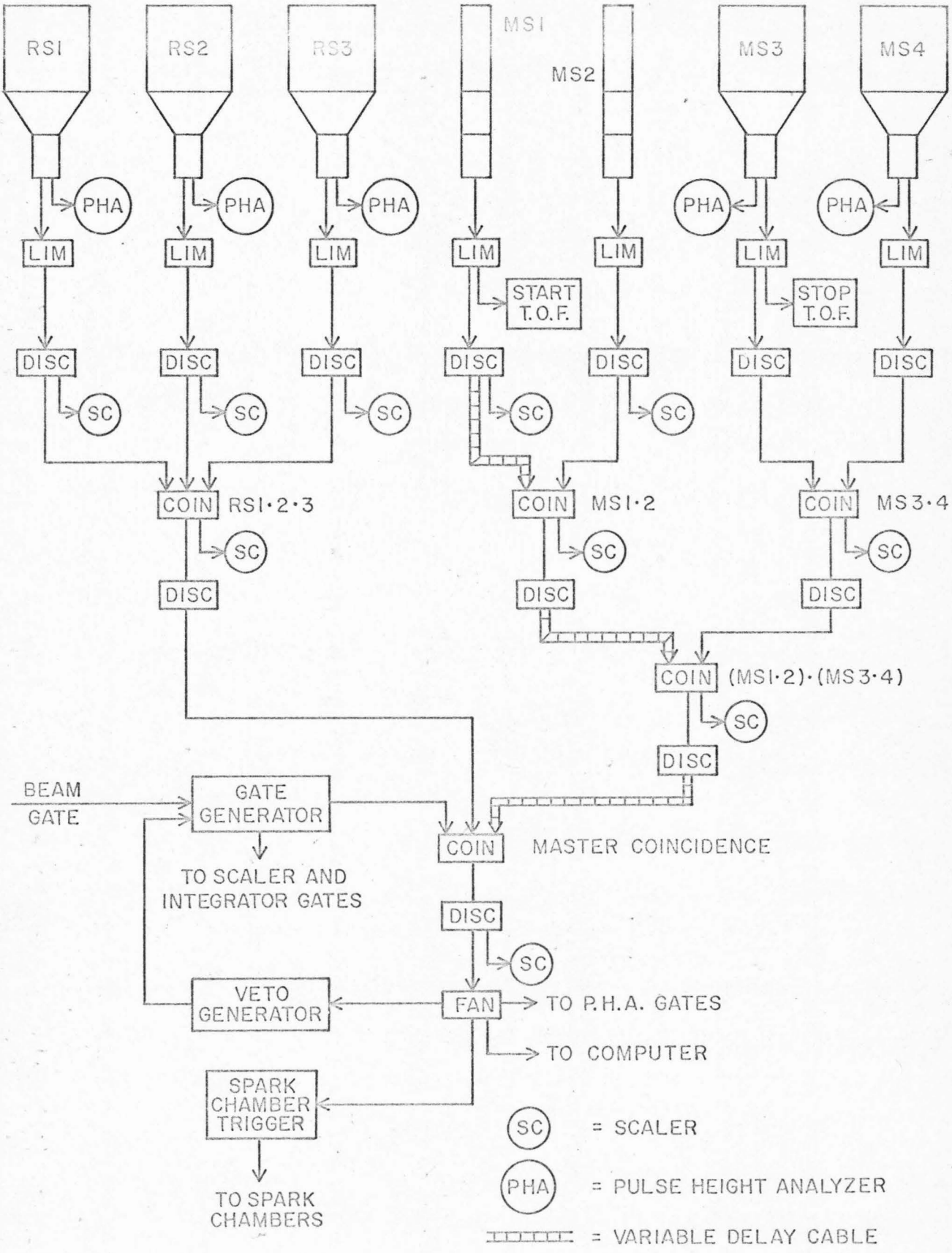


Figure 2.5 The Trigger Electronics

Table 2.3

Caltech-Designed Electronics
Used in This Experiment

| Name in Figures 2.8, 2.9 | Name in References |
|---|---|
| LIM | Limiter-3 |
| DISC | TVD-3B |
| COIN | TC-6 |
| FAN | Limiter-3 |
| Spark Chamber Trigger | SCT-1 |
| SPHA | SPHA-1 |
| GATE | T6-3 |
| Fast AMP | FA-1 |
| Veto Generator | not described |
| Gate Generator | not described |

The data were recorded onto magnetic tape via a PDP 5 computer. For each event, 183 12-bit words constituted a 'record'.

| Word | Data |
|---|---|
| 1 | Run # |
| 2-3 | Event # |
| 4 | Setting # |
| 5-10 | Pulse Heights |
| 11-13 | Beam Monitors |
| 14-183 | Spark Coordinates |

At the end of each run, three additional records were written. Two contained summary distributions of the pulse heights and the third was a comment record, stored in BCD characters.

The analog to digital conversion of the signals from the scintillation counters in the electronics is diagrammed in Figure 2.6. The pulses from counters RS1, 2, 3 and MS4 were shaped into pulses of standard voltage with duration proportional to the area (charge) of the input pulse in the SPHA-1 circuits. The output pulses were digitized by a LeCroy Model 151 quad digitizer, and then transmitted to the computer. The pulse height from counter MS3 and the time of flight of particles between counters MS1 and MS3 were processed in a Nuclear Data Model 160-F, 150-M analogue to digital converter. A TVD-3B circuit in its start-reset mode was used to produce a pulse of standard voltage and of duration proportional to the time difference between signals from counters MS1 and MS3.

During each run, the computer accumulated distributions of the pulse heights and displayed them on an oscilloscope. Figure 2.7 shows such a display for a run in which it was possible to detect deuterons

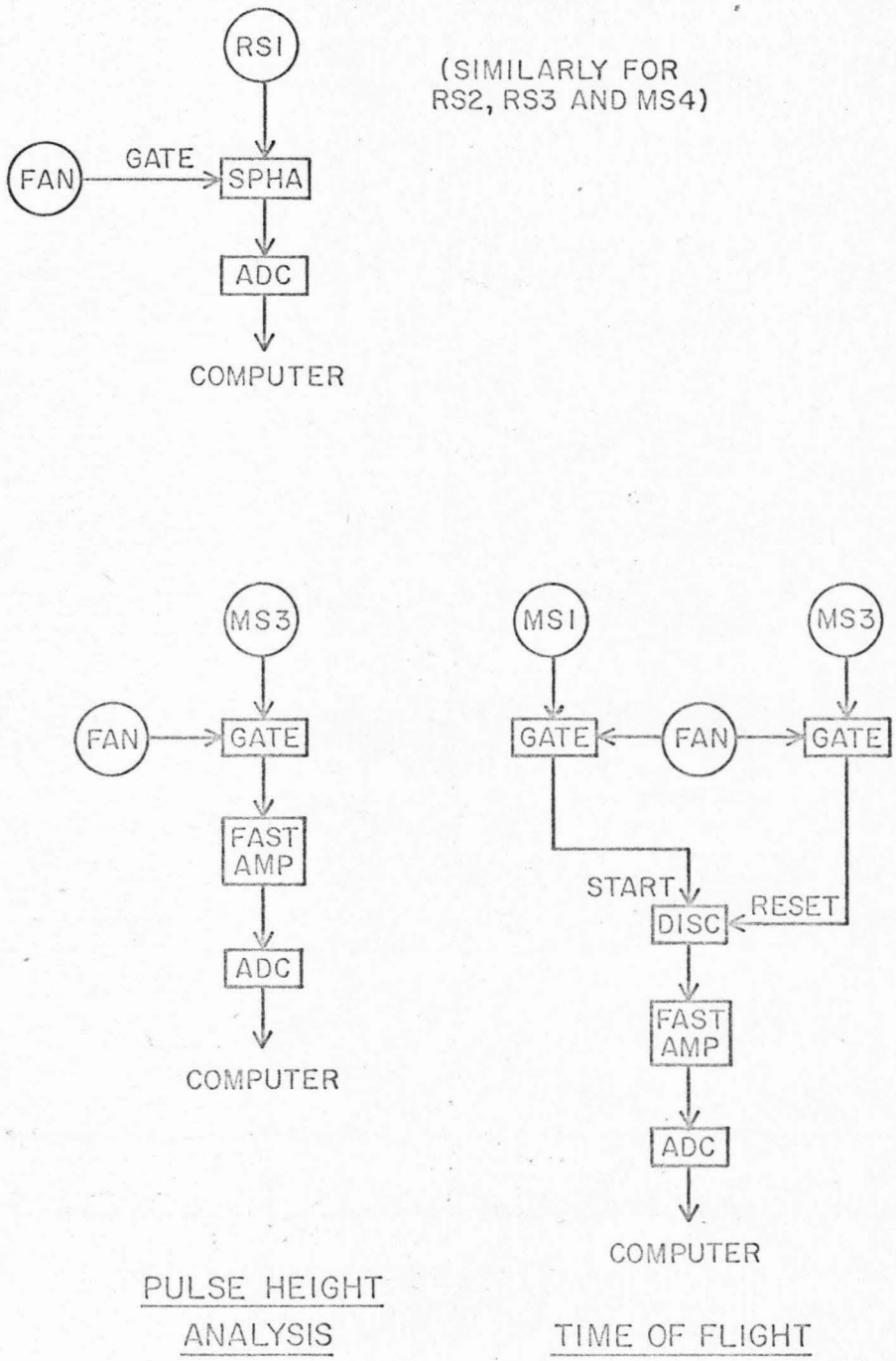


Figure 2.6 The Pulse Height Analysis Electronics

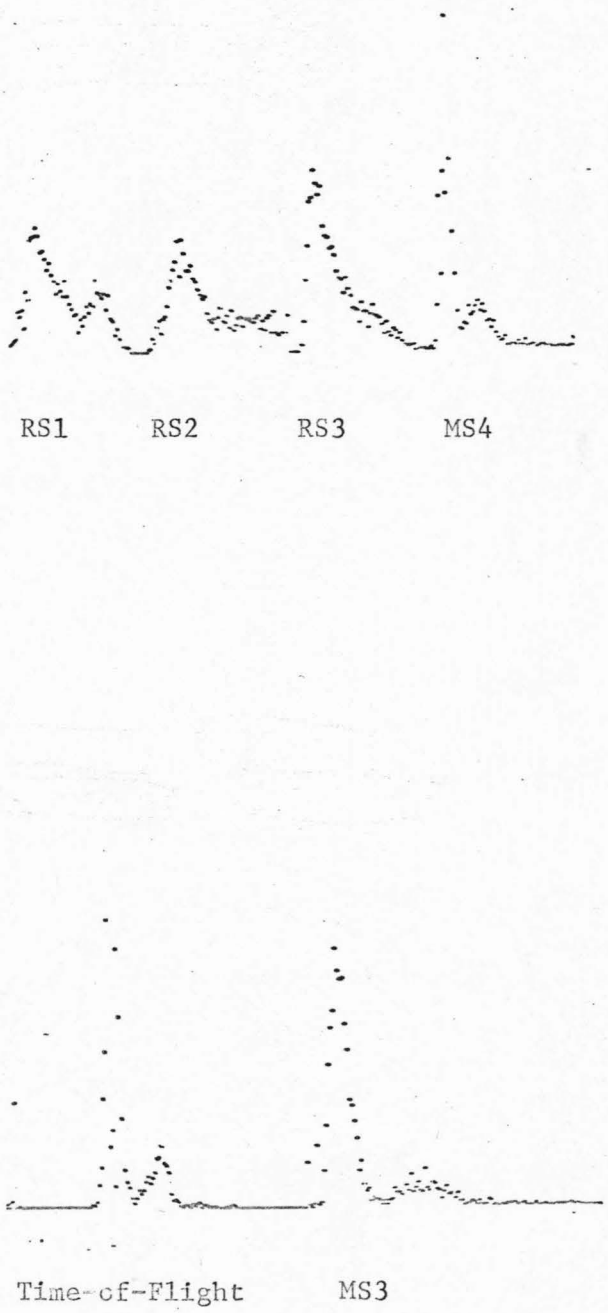


Figure 2.7 Examples of the Pulse Height Spectra Display

in both the magnet and range arrays. The large peak in the time of flight spectrum is due to protons, with a smaller peak due to deuterons at later times. The other five displays are scintillation counter pulse height spectra. They also show the expected double peaked structure, protons having lower pulse heights than deuterons.

For each event, the cumulative outputs of three beam monitors were recorded. Specifically, they were the thick plate ion chamber and the two thin plate ion chambers, discussed in Appendix E. A special circuit was built to interrogate the output of the ion chamber current integrators and transmit this information to the computer. These data were not used extensively in the later analysis of the experiment.

The last block of electronics was for the purpose of converting the signals from the wire chambers to digital form and transmitting the results to the computer. These circuits and their operation have been described in detail by Charles Prescott[24].

For each event, the computer displayed the coordinates of the digitized sparks on an oscilloscope. Figure 2.8a shows this display from a good event. (However, some of the second fiducials are missing.) The particles' directions are from left to right. The y view is a top view, the x a side view. The first six columns of sparks are from the front magnet chambers; the next four are from the rear magnet chambers; the next five are the front range chambers; and the last ten are the (little used) rear range chambers. Figure 2.8b shows a multiple exposure of several events, illustrating the spread of tracks in the chambers.

a. An Event

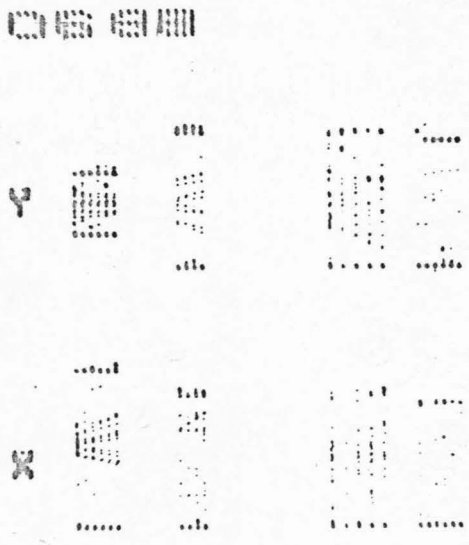

b. Multiple Exposure of Several Events

Figure 2.8 Examples of the Spark Chamber Display

D. Summary of Data Collected

Approximately 300,000 triggers were collected in two months of running. There were 135 runs at a total of thirty-four settings of the apparatus. The data occupy nearly fifty 2400 foot magnetic tapes, recorded at 200 bytes per inch.

Table 2.4 summarizes the basic parameters of the various settings, and the number of events collected at each. The parameter listed are:

$\theta$ c.m. = center of mass angle of final proton,

$E\gamma$ = average incident photon energy,

$\theta$ Magnet = lab angle of the magnet array,

$\theta$ Range = lab angle of the range array.

Protons were detected in the magnet array at settings 1 - 18, while deuterons were detected at the other settings.

In addition, a short run was made at each setting in which the $He^3$ target was empty, in order to investigate the possible origin of events in the target walls.

Table 2.4

Summary of Data Collected

| Setting | $E_\gamma$ (MeV) | $\theta$ c.m. | $\theta$ Magnet | $\theta$ Range | Events |
|---|---|---|---|---|---|
| 1 | 250 | $30^o$ | $26.4^o$ | $140.5^o$ | 13,527 |
| 2 | 250 | $30^o$ | $26.4^o$ | $140.5^o$ | 5,718 |
| 3 | 300 | $30^o$ | $25.4^o$ | $138.0^o$ | 10,145 |
| 4 | 300 | $30^o$ | $25.4^o$ | $138.0^o$ | 18,800 |
| 5 | 400 | $30^o$ | $25.0^o$ | $135.9^o$ | 8,578 |
| 6 | 400 | $30^o$ | $25.0^o$ | $135.9^o$ | 19,676 |
| 7 | 200 | $60^o$ | $53.4^o$ | $105.5^o$ | 12,919 |
| 8 | 300 | $60^o$ | $51.9^o$ | $102.5^o$ | 12,116 |
| 9 | 300 | $60^o$ | $51.9^o$ | $102.5^o$ | 9,709 |
| 10 | 400 | $60^o$ | $50.7^o$ | $99.8^o$ | 3,911 |
| 11 | 450 | $60^o$ | $50.7^o$ | $99.8^o$ | 6,269 |
| 12 | 300 | $75^o$ | $46.8^o$ | $91.6^o$ | 11,264 |
| 13 | 200 | $90^o$ | $82.0^o$ | $75.6^o$ | 7,680 |
| 14 | 250 | $90^o$ | $82.0^o$ | $75.6^o$ | 5,119 |
| 15 | 300 | $90^o$ | $80.3^o$ | $72.7^o$ | 4,162 |
| 16 | 300 | $90^o$ | $80.3^o$ | $72.7^o$ | 6,395 |
| 17 | 350 | $90^o$ | $78.3^o$ | $70.5^o$ | 4,142 |
| 18 | 400 | $90^o$ | $78.3^o$ | $70.5^o$ | 2,490 |
| 19 | 350 | $90^o$ | $72.7^o$ | $80.0^o$ | 4,600 |
| 20 | 400 | $90^o$ | $72.7^o$ | $80.0^o$ | 4,097 |
| 21 | 400 | $90^o$ | $70.6^o$ | $78.2^o$ | 7,121 |
| 22 | 450 | $90^o$ | $70.6^o$ | $78.2^o$ | 1,081 |
| 23 | 300 | $105^o$ | $59.3^o$ | $95.1^o$ | 16,015 |
| 24 | 250 | $120^o$ | $48.7^o$ | $112.3^o$ | 7,172 |
| 25 | 300 | $120^o$ | $46.8^o$ | $110.7^o$ | 12,975 |
| 26 | 350 | $120^o$ | $46.8^o$ | $110.7^o$ | 4,693 |
| 27 | 350 | $120^o$ | $45.3^o$ | $108.7^o$ | 762 |
| 28 | 500 | $120^o$ | $45.3^o$ | $108.7^o$ | 5,412 |

Table 2.4

(Continued)

| Setting | $E_\gamma$ (MeV) | $\theta$ c.m. | $\theta$ Magnet | $\theta$ Range | Events |
|---|---|---|---|---|---|
| 29 | 250 | $150^o$ | $24.0^o$ | $145.3^o$ | 2,727 |
| 30 | 250 | $150^o$ | $24.0^o$ | $145.3^o$ | 6,397 |
| 31 | 300 | $150^o$ | $22.9^o$ | $144.1^o$ | 8,971 |
| 32 | 350 | $150^o$ | $22.9^o$ | $144.1^o$ | 4,794 |
| 33 | 400 | $150^o$ | $22.2^o$ | $142.9^o$ | 5,107 |
| 34 | 450 | $150^o$ | $22.2^o$ | $142.9^o$ | 6,755 |

# III. DATA ANALYSIS

The task of analyzing the data in this experiment involves two separate problems. First, true $\gamma + He^3 \rightarrow p + d$ events must be extracted from all the events collected, and second, the efficiency of the apparatus for collecting such events must be determined.

Prior to the selection of good events, the tracks of the particles must be reconstructed from the spark coordinates in the wire chambers as described in Section A below. The tracks then are used to calculate various quantities needed to complete the experimental description of an event (Section B). The procedure for separating good events from bad is discussed in Section C.

The most important efficiency is the geometric efficiency (solid angle) of the apparatus, including the acceptance of the magnet. This was calculated with a Monte Carlo computer program, discussed in Section D. Other efficiences, such as that of the spark chambers and electronics, are also considered in Section D. The conversion of the preceding results into cross-sections is described in Section E and the systematic errors and resolution are treated in Section F.

A. Track Reconstruction

For each event there were three straight tracks to be found in the wire chambers: one in the six front magnet array chambers, another in the four rear magnet chambers, and the third in the five range array chambers. Each chamber provided x and y coordinate information on the sparks within.

The basic approach to the track fitting follows that of S. Cheng and C. Prescott in an earlier experiment with the present wire chamber system[25]. Taking the z axis as perpendicular to the planes of the chambers, straight track projections were found in the x-z plane and y-z plane independently. If more than one such projection is found in either plane, there is an ambiguity to be resolved as to what is the real track in space. We did not utilize the common solution to this problem which is to include chambers in the array with wires running at, say, $45^{o}$, to the x and y axes.

Consider first the problem of finding a track projection in a single view. Depending on the array, there were 4, 5 or 6 chambers with up to four sparks in each. Any pair of sparks in different chambers forms a line segment which potentially belongs to an actual track projection. The procedure was to extend each such line segment into the other chambers and check if any sparks were within 0.1" of the resulting points of intersection. If not, the line segment was rejected as a possible candidate. If so, there were three or more sparks lying in a strip of width 0.2", and it was assumed that a real track projection

was to be found therein. A straight line was fitted to each group of three or more sparks within the strip, and that line with the minimum chi-square per degree of freedom was taken as the true one.

This procedure was tested by comparing the results with a visual scan of the spark data as displayed on an oscilloscope by special playback program on a PDP 8 computer. There was less than 1% disagreement in whether or not a track projection was present, and in the disputed cases, I judge the above procedure to be more reliable than a visual scan. Thus I estimate the track finding algorithm to be better than 99% efficient at finding tracks, if they can be found. I believe many of the disputes were caused by events in with a phantom 'spark' occurred before the first fiducial, which has the effect of shifting the coordinates of real sparks. The eye tends to be more lenient than the computer in accepting these spurious shifts. This effect also complicated the estimation of the spark efficiency of the chambers, as discussed in Section D below.

The relations between the front and rear magnet tracks discussed in Appendix G allow events to be saved if tracks are missing due to chamber inefficiencies in one or the other region (but not both). Because the magnetostrictive wands can suffer inefficiencies, sparks missing in the x-z and y-z views are not always correlated. As noted in Appendix G, the x-y and y-z views of a track in front of the magnet are independently related to the corresponding views of the track behind the magnet. Thus, if there were not enough sparks to define a track projection in the y-z view in front of the magnet, but a y-z view

track projection is present behind it, the front track projection can be extrapolated from the rear. To insure this process did not invent spurious tracks, it was required that there be two sparks in the front chambers along the extrapolated track. For the x-z view, the relation between the front and rear track projections depends on the particle's momentum. It is possible to determine the momentum given only a track projection on one side of the magnet and one spark on the other. Again, it was required that two sparks could be found that yielded the same momentum before the missing track projection was declared recovered. These procedures salvaged about 5% more events than would have been possible without them.

We now consider the problem of determining the real track when more than one track projection appears in the x-z and/or y-z views. In less than 1% of the events were there more than one track projection in both x-z and y-z views of an array, as anticipated when the experiment was designed. However, the circumstance that one view has more than one track projection while the other has only one occurred about 10 to 15% of the time in the range chambers. This most probably indicated the presence of an electron in the chambers, as an electron suffers significant multiple Coulomb scattering, so that its path is not very straight. Thus it was possible that such events had a reconstructible track projection in only one view.

The following procedure was used in all cases when there was a multiple track ambiguity in the front magnet or range chambers. Each track projection in each view was extrapolated into the $He^3$ target, and

those which missed the target by more than 1" were rejected. Then, for both arrays, a track in space was formed by combining one x-y view track projection with one from the y-z view. The 'coplanarity', or difference between the azimuthal angles - $180^{o}$, of the two tracks was calculated. This was done for all possible combinations of track projections from the x-z and y-z views, and the combination with the minimum coplanarity was chosen as the 'real' one. As noted above, in most instances when this procedure was necessary, there were only two combinations, resulting from five track projections in the four views in the front chamber arrays. Further, most often the ambiguity was in the range chambers, which would not affect the later calculation of the incident photon energy which is derived from quantities determined in the magnet array. Thus I feel that the practical effect of possible mischoices is below the 1% level - the fraction of events where the ambiguity was in the magnet array.

In case of an ambiguity in the rear magnet chambers, that track was chosen which when combined with the other tracks predicted the smallest deviation in a calculation of the properties of the particle in the range chambers. This choice was necessary less than 1% of the time.

The tracks in the magnet array were investigated as to whether the particle had scattered off of the magnet pole tips or other framework. This was done by extrapolating the front tracks to the rear of the magnet and comparing with the observed track. If the comparison

was not satisfactory, the event was rejected. Multiple Coulomb scattering rendered this comparison less decisive than is desirable. I feel it would have been wiser to have placed scintillation counters around the boundary of the magnet gap, so that any particle outside the desired region could have been vetoed on the basis of a signal in these counters.

Figures 3.1 and 3.2 illustrate the results of the track reconstruction. The coordinate frame had the z-axis along the photon beam which was horizontal in the lab; the x-axis was vertical and the y-axis was horizontal. Figure 3.1 shows the projection of the reconstructed event vertices onto the x-y plane. The beam spot was about 1.2 inches in radius. In general, the tracks in the front magnet and range chambers did not intersect but are skew, and a 'vertex' as plotted is the mid-point of the line joining the closest points on the two tracks. Figure 3.2 shows the distribution of the skew distances of closest approach of the two tracks. In Figure 6.6 of Appendix D, the radial distribution of event vertices is compared with a curve taken from densitometric analysis of a photographic plate exposed in the photon beam.

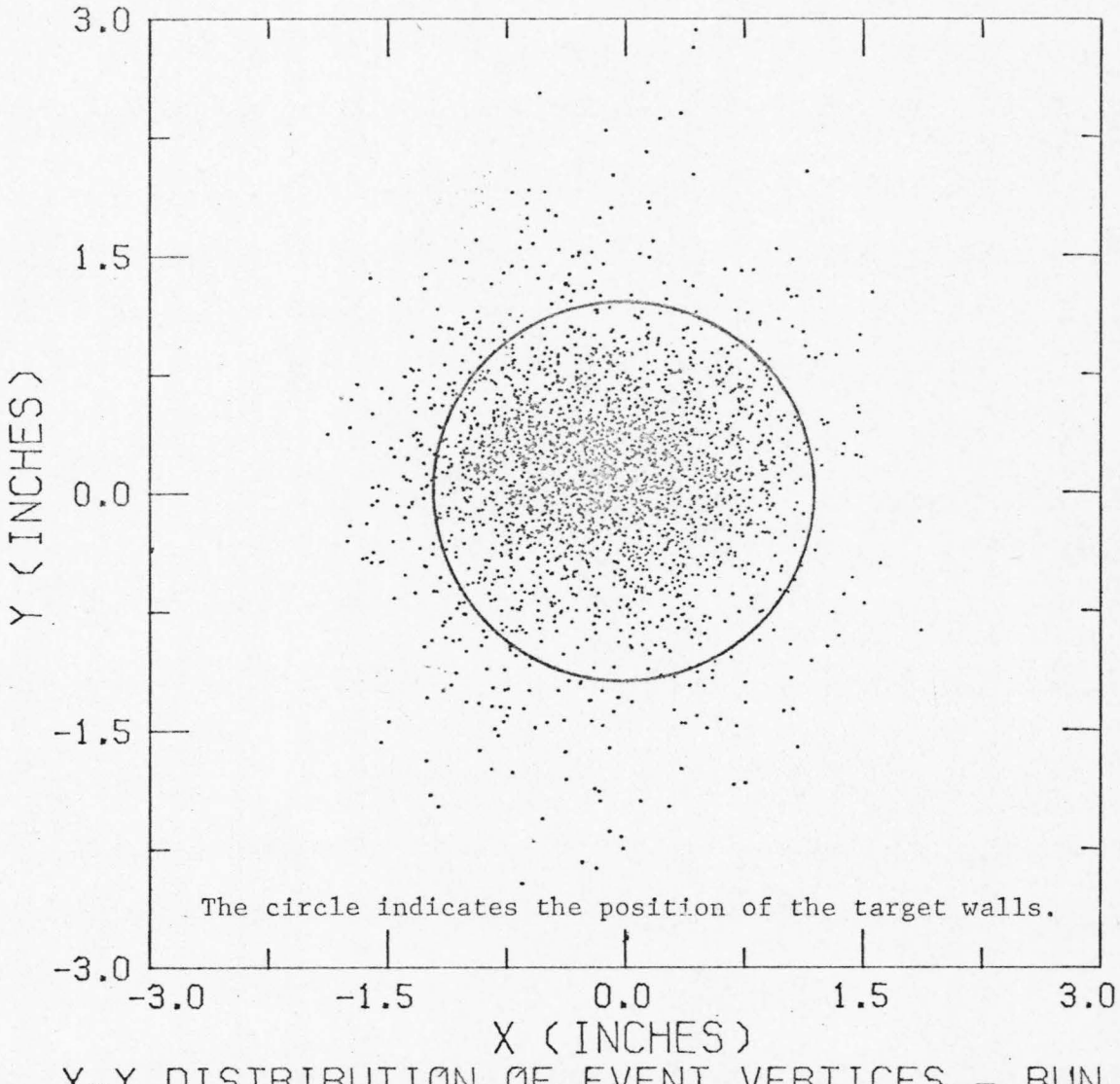
3.0
1.5
0.0
-1.5
-3.0
Y (INCHES)
-3.0
-1.5
0.0
1.5
3.0
X (INCHES)
The circle indicates the position of the target walls.
X-Y DISTRIBUTION OF EVENT VERTICES - RUN 68

Figure 3.1

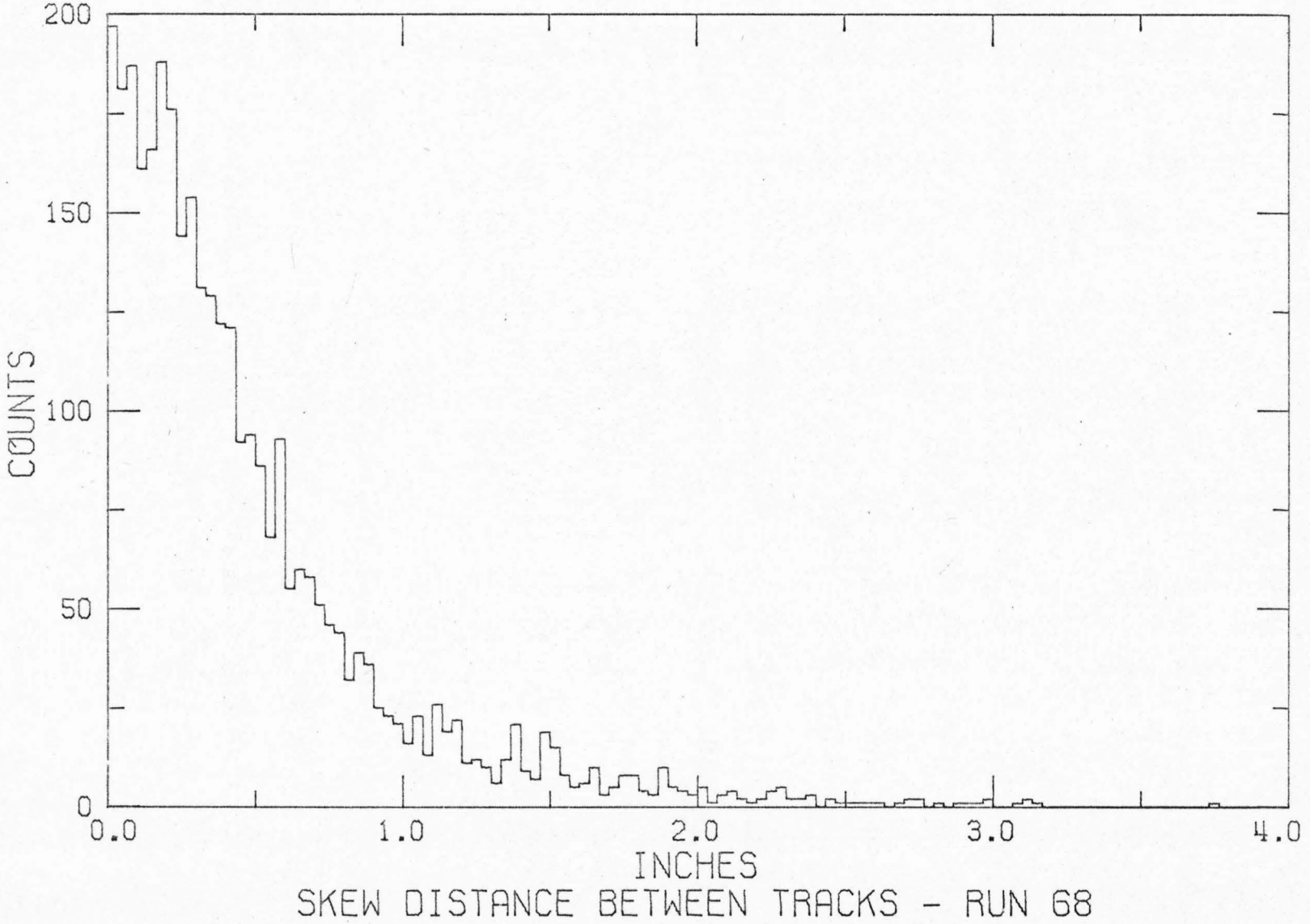
200
150
100
50
0
COUNTS
0.0
1.0
2.0
3.0
4.0
INCHES
SKEW DISTANCE BETWEEN TRACKS - RUN 68

Figure 3.2

B. Event Reconstruction

With a knowledge of the tracks, and the momentum of the particle in a magnet, futher parameters of an event can be calculated. Events for which this information is available are called 'reconstructible'.

The polar and azimuthal angle of each particle with respect to the photon beam are obtained at once. Call these $\theta_M$ and $\phi_M$ for the particle detected in the magnet array, and $\theta_R$ and $\phi_R$ for the particle in the range array. The coplanarity of the two particle is defined by

$$\phi_M - \phi_R - 180^o.$$

For a scattering with only two particles in the final state, the coplanarity should be zero. However, multiple scattering broadens the distribution even for real events. Figure 3.6 shows the coplanarity distribution for all reconstructible events in run 74. A peak of half width about $1^o$ containing the good events is seen to rise above a broader background.

If the identity (and hence the mass) of the particle in the magnet array is assumed, then the mass of the particle in the range array, the incident photon energy and the center of mass angle of the scattering can be calculated. Thus

$$M_R^2 = (P_M \cdot (\cos\theta_M + \cos\theta_R \cdot \sin\theta_M/\sin\theta_R) + M_H - E_M)^2 - (P_M \cdot \sin\theta_M/\sin\theta_R)^2$$

$$E = \frac{2M_H E_M - M_H^2 - M_M^2 + M_R^2}{2(M_H - E_M + P_M \cos\theta_M)}$$

$$\theta_{c.m.} = \tan^{-1}\left(\frac{P_M \cdot \sin\theta_M}{\gamma(P_M \cos\theta_M - \beta E)}\right)$$

$$\beta = E/(E + M_H) \qquad \gamma = \sqrt{1/(1-\beta^2)}$$

$$E_M^2 = M_M^2 + P_M^2$$

where $M_H$ = mass of $He^3$

$M_M$, $P_M$, $E_M$ = mass, momentum and energy of the particle in the magnet array.

$M_R$ = mass of particle in the range array.

$E$ = incident photon energy.

$\theta_{c.m.}$ = scattering angle of the proton in the $\gamma$ - $He^3$ center of mass frame.

In practice, E was calculated using the exact value of $M_R$ (assuming a correct particle identification) while the calculation of $M_R$ was used to separate good events from bad.

Figure 3.4 shows a distribution of the quantity $M_R$ (calculated) - $M_R$ (exact) for all reconstructible events in run 74. This is called the missing mass although it is more precisely a mass excess. The good events lie in a peak of width about 20 MeV/$c^2$ centered at zero while the background events center at 50 MeV/$c^2$ with a width of about 50, in this case.

Figure 3.5 shows the reconstruction of the incident photon energy spectrum for the same run. Events below 250 MeV will later prove to be entirely background. The number of events at a given incident photon energy is, of course, directly related to the cross-section. Thus the remaining effort in processing the events is to exclude bad events from this distribution. All other distributions are secondary in the sense that while they can aid in the elimination of bad events,

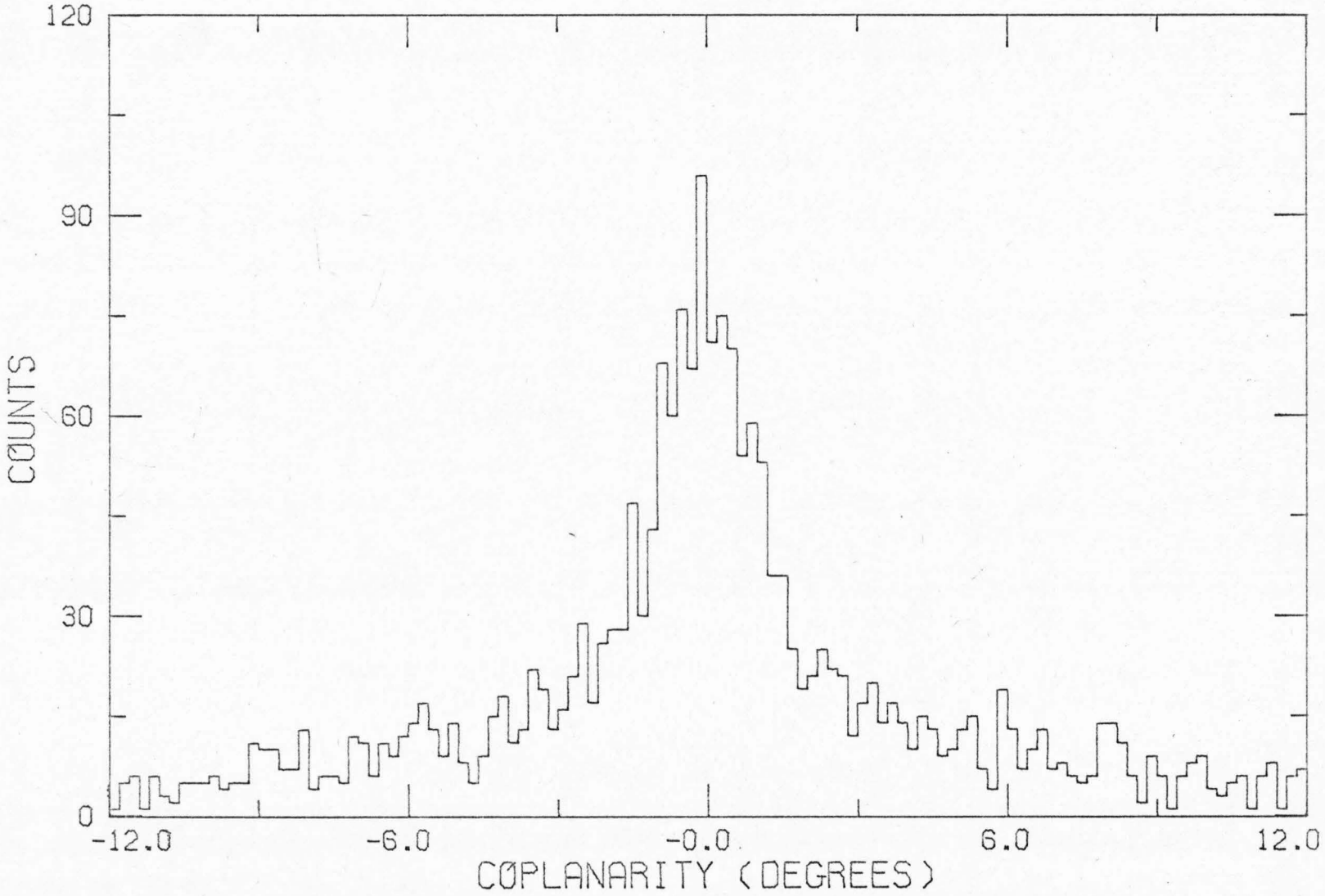


Figure 3.3 A Raw Coplanarity Distribution

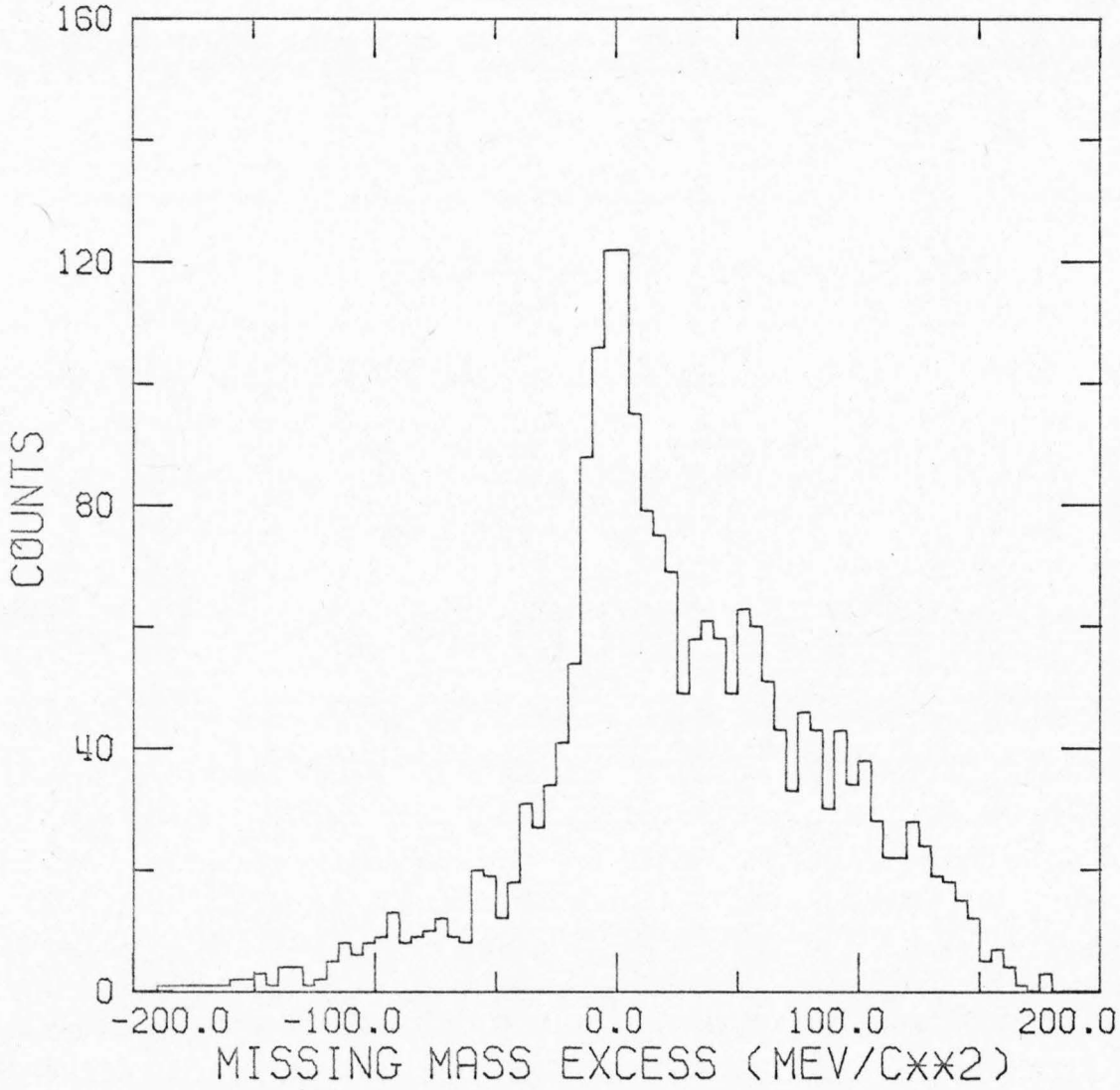


Figure 3.4 A Raw Missing Mass Distribution

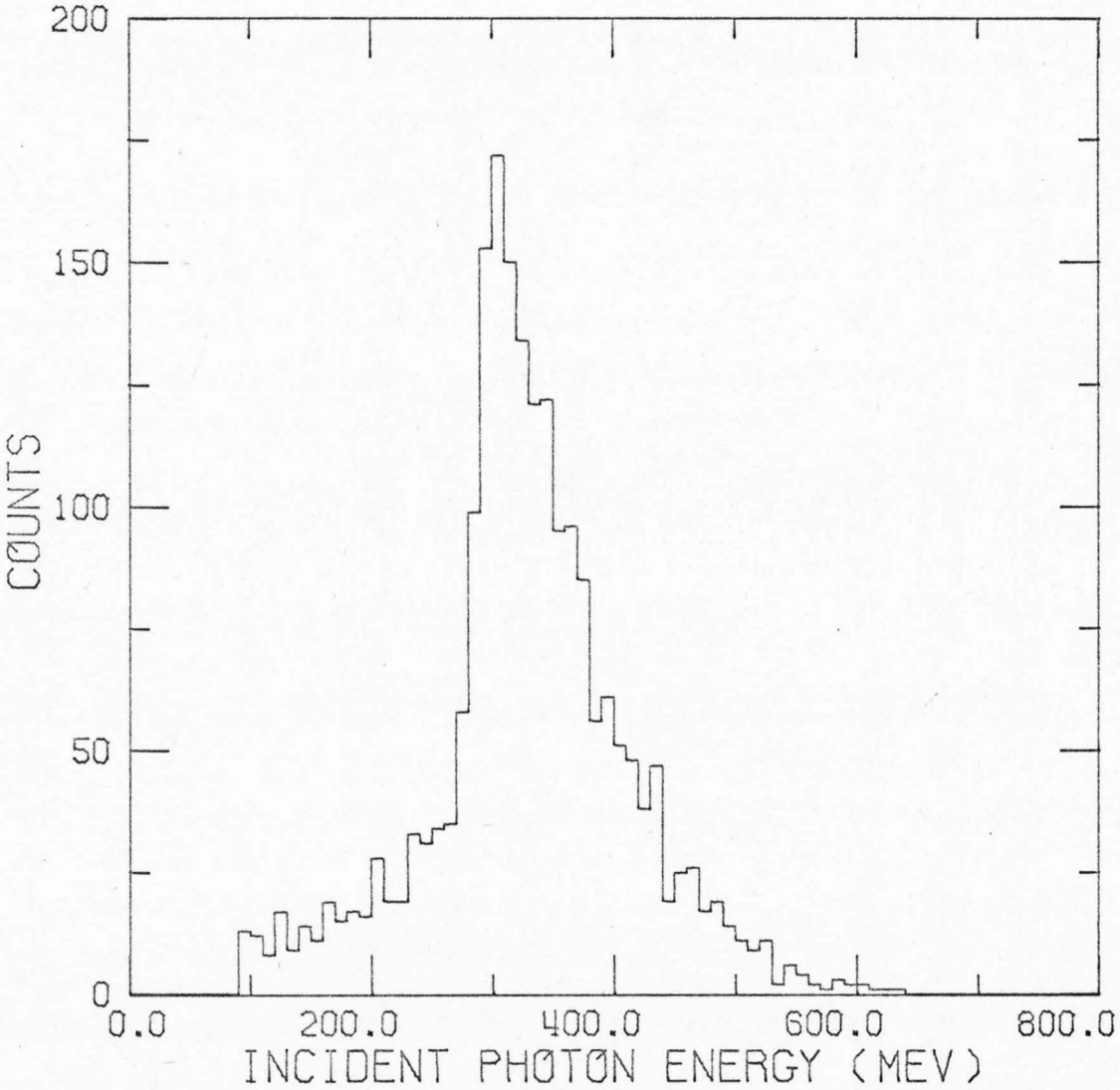


Figure 3.5 A Raw Incident Photon Energy Spectrum

they are not simply related to the value of the scattering cross-section.

We have so far assumed the identities of the particles detected in the magnet and range arrays. The various pulse heights and the time of flight measurement were useful to check this. First, the points of intersection of the tracks and the scintillation counter were calculated and a correction applied to the pulse heights for the variation of light output as a function of position.

Depending on whether a proton or a deuteron was expected in the magnet array, different pulse height distributions are most useful. If a proton was in the magnet array, the width of the gate in the time of flight circuitry discriminated against positrons and deuterons. Fast protons could conceivably be confused with slow pions in the time of flight spectrum. The pulse heights of the magnet scintillation counters for such protons and pions were in the same range. Thus the electronics of the magnet array provided a fairly pure sample of protons, which could not be further purified by looking at the details of the time of flight spectrum or the magnet scintillator pulse heights. A proton in the magnet array should correspond to a deuteron in the range array. The deuterons were slow moving compared to the speed of light and consequently had large pulse heights. Figure 3.6 shows the pulse height distribution of particles in counter RS1 of the range array, for a run with predominantly protons in the magnet array. Deuterons have pulse heights of roughly 400 or more (arbitrary units).

The separation of deuterons from (in all probability) protons with high pulse heights is not completely clean; individual events

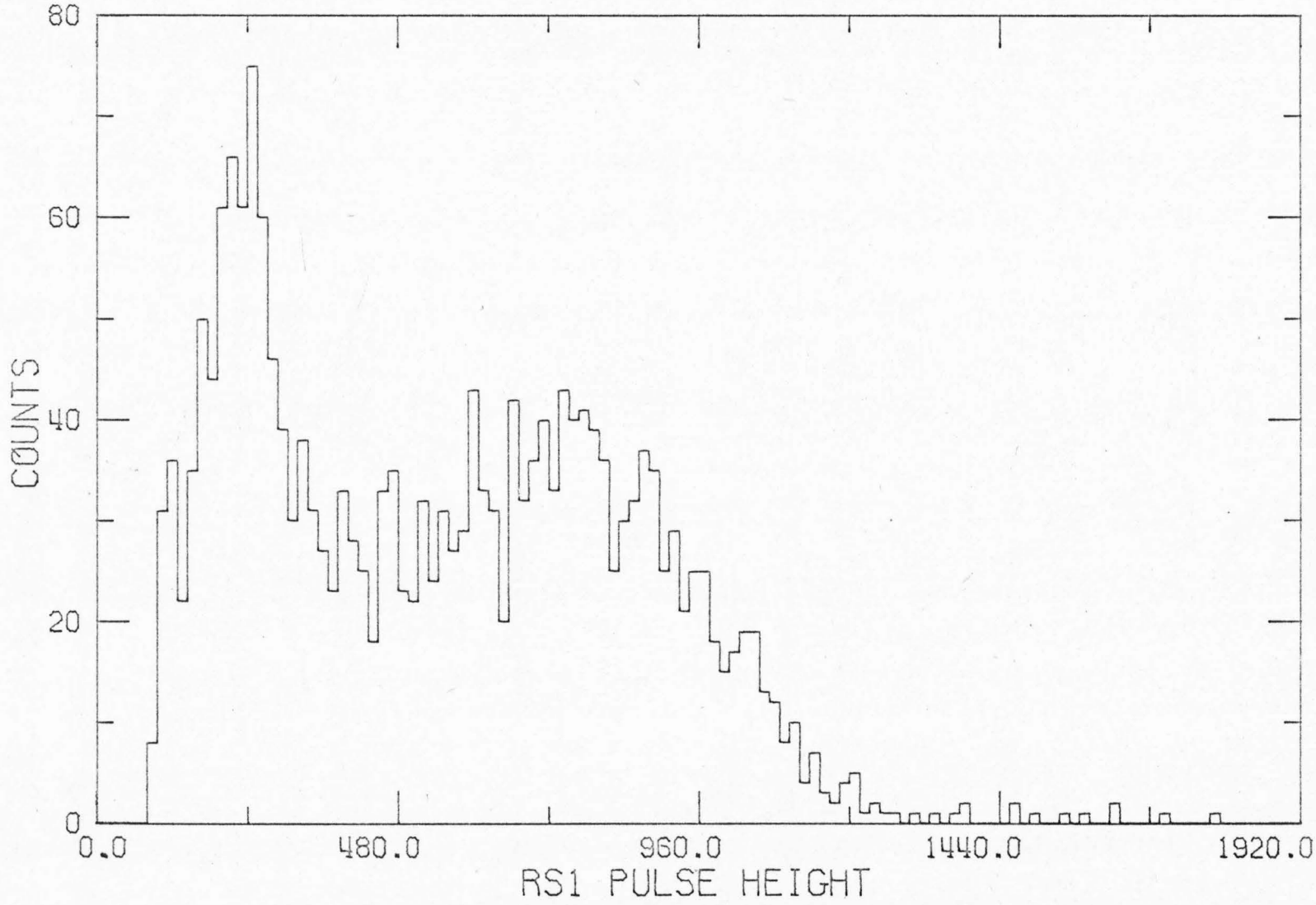


Figure 3.6 A Raw Pulse Height Spectrum in Counter RS1

cannot be positively identified as p-d final states. Hence a background subtraction is needed.

In the case that a deuteron is expected in the magnet, the situation is much simpler. The time of flight spectrum (see Figure 2.3) allows a clear identification of deuterons. The pulse height in counter MS3 was used to confirm this identification. Figure 3.7 shows a spectrum in counter MS3 with deuterons having pulse heights averaging eighty compared to twenty for protons. With deuterons in the magnet array, protons are expected in the range array. The other possibilities are electrons or pions. A background subtraction was made to correct for such spurious events.

In summary, a reconstructible event is parametrized by its

1. Incident photon energy;
2. Center of mass scattering angle;
3. Coplanarity;
4. Mass excess of particle in the range array;
5. RS1 pulse height if a proton was in the magnet array or time of flight and MS3 pulse height if a deuteron was in this array.

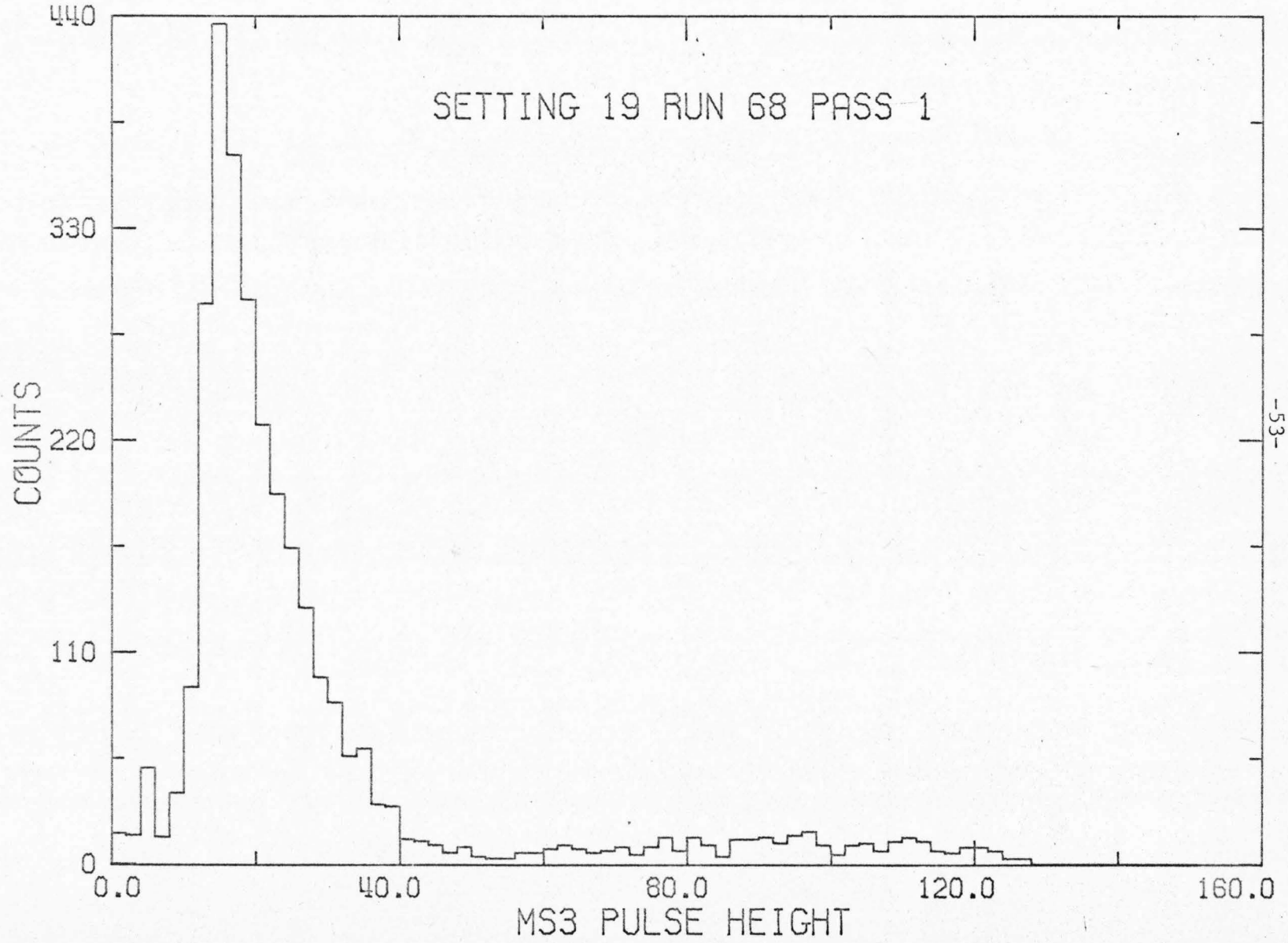


Figure 3.7 A Raw Pulse Height Spectrum in Counter MS3

C. Background Subtraction

Aside from accidental coincidences, the following $\gamma + He^3$ reactions might contribute to the background of $\gamma + He^3 \rightarrow p + d$ (only reactions with two charged particles in the final state are listed):

$$\gamma + He^3 \rightarrow T + \pi^+ \qquad (1)$$

$$\left.\begin{array}{l} d + p + \pi^o \\ d + n + \pi^+ \end{array}\right\} (2)$$

$$\left.\begin{array}{l} p + p + n \\ p + p + n + \pi^o \end{array}\right\} (3)$$

$$\text{etc.}$$

The meagre experimental data[26] on reaction (1) indicate that its cross-section might be five times that of $\gamma + He^3 \rightarrow p + d$. However, the laboratory kinetic energy of the tritium is so low as to make detection difficult, and essentially impossible with the apparatus of this experiment. A survey[27] of $\gamma + He^3$ reactions using a diffusion chamber detected only one-third as many $T\pi^+$ events as pd.

Reactions of type (2) would be the principal source of background in runs where deuterons were detected in the magnet array; about as many events of this type as of the pd final state were observed in the survey experiment. The $p\pi^o$ or $n\pi^+$ can come from a $\Delta^+(1236)$ without the isospin complications present with only a pd final state. Thus the cross-section for these reactions might well be much greater than for $\gamma + He^3 \rightarrow p + d$. A rather optimistic paper[28] has predicted an enhancement of about three orders of magnitude. Of course, three-particles in a final state will not be so strongly correlated as only two, and the

efficiency of the apparatus for detecting two out of three particles is much less than for two out of two.

Reactions of type (3) would be the principal background for runs with protons in the magnet array. There is experimental evidence[73] that the ppn state is about as likely as the pd state for incident photon energies below 50 MeV. However, by 150 MeV the ppn states occur about five times as often as the pd. The previous remark about the lower efficiency for detection of three particle states applies here also. For photon energies around 300 MeV, production of the pnn$\pi^+$ state will probably be of the same order of magnitude as of the ppn state.

Thus the background consists of several different reactions about which even less is known than the reaction being studied. Accordingly, no attempt was made to calculate the background. But instead, an empirical procedure was devised to estimate it.

The desired result of the background subtraction is the true number of events as a function of incident photon energy. However, as seen in the preceding section, the 'foreground', or good event sample, stands out from the background most clearly in the distributions of coplanarity, missing mass excess and the pulse heights. Data from all the photon energies accepted during a run are lumped together in such plots. If these distributions were calculated for only a small range of photon energies, there would be so few events that the statistical accuracy of any background subtraction would be poor.

To overcome this difficulty inherent to experiments with a bremsstrahlung photon beam, we used a procedure devised by Leon

Rochester[29]. To make an initial separation of the foreground from the background, consider the distribution of all events (from a single run) as a function of coplanarity and missing mass excess. This distribution can be divided into two regions: the foreground region at small values of coplanarity and mass excess, chosen to contain all foreground events, but having some background contamination; and the background region which consists of the remaining events and includes only background.

The problem is to use the events in the background region to estimate the number and the photon energy spectrum of the background events which lie in the foreground region. The procedure for this takes advantage of the observed fact that background events do not have strong correlations among the eight parameters which define an event:

- The (3) coordinates of the event origin in the target.

- The (4) coordinates of the intersections of the particle's tracks with counters MS2 and RS1.

- The momentum of the particle measured in the magnet.

A collection of 'fake' events can be constructed by choosing sets of eight parameters at random from those describing the background region. The eight parameters of a 'fake' event are, in general, drawn from eight separate background events by a random number generator. If N is the number of events in the background region, then $8^N$ independent 'fake' events can be generated. If the eight parameters are indeed uncorrelated, the 'fake' events should reproduce the structure of the

background region as a function of coplanarity, mass excess, or photon energy. However, these events are not restricted to the background region but populate the foreground region as well. The ratio of the number of background events in the foreground region to the number in the background region can be determined from the 'fake' event sample. Further, a photon energy spectrum for background events in the foreground region is generated, and can be properly normalized using the above ratio. This normalized spectrum is then subtracted from the spectrum for all events in the foreground region to yield the corrected number of $\gamma + He^3 \rightarrow p + d$ events as a function of photon energy.

The statistical accuracy of this procedure is easily demonstrated. Let $N_I$ be the (unknown) number of background events inside the foreground region, with photon energies in some given energy interval. The above procedure estimates

$$N_I = N_o \cdot M_I / M_o$$

where $N_o$ = number of events outside the foreground region.

$M_o$ = number of 'fake' events outside the foreground region.

$M_I$ = number of 'fake' events inside the foreground region lying in the desired energy interval.

$N_o$, $M_o$ and $M_I$ are subject to statistical uncertainties, leading to an uncertainty in $N_I$:

$$(\sigma_I / N_I)^2 = 1/N_o + 1/M_o + 1/M_I$$

As $M_o$ and $M_I$ can be made arbitrarily large (up to $8^{N_o}$), $N_o$ is the main source of uncertainty in $N_I$. In this procedure, $N_o$ is as large as

possible since it is the entire background region sample, not just those events lying in the energy interval of $N_I$, as would be the case for a more typical method. Hence our method attains the maximum statistical precision available.

Rochester has gone to considerable length in his thesis[29] to justify the procedure in general. We have verified that the eight parameters used to describe a background event are uncorrelated, and that the resulting 'fake' events reproduce the structure of the background (cf. Appendix H). We have checked that the results are not systematically dependent on the size of the background region, so long as true foreground events are not included in it. Also, the subtraction was only 10 to 15 percent, so that the procedure need not be precise in all details to yield good results.

In Appendix H, the subtraction process is presented in detail for a particular run. The resulting corrected photon energy spectrum is shown in Figure 3.8.

A background problem not yet considered is the possibility of events originating in the material of the target walls, rather than in the $He^3$. It is, however, unlikely that reactions in which photons hit protons, carbon or oxygen nuclei, etc., could imitate $\gamma + He^3 \rightarrow p + d$. To be safe, a short empty-target run was taken at each setting. The resulting event rates were not zero, but very few of them contained enough tracks to reconstruct the event. In these, there is no sign of a signal in the distributions of coplanarity or missing mass excess.

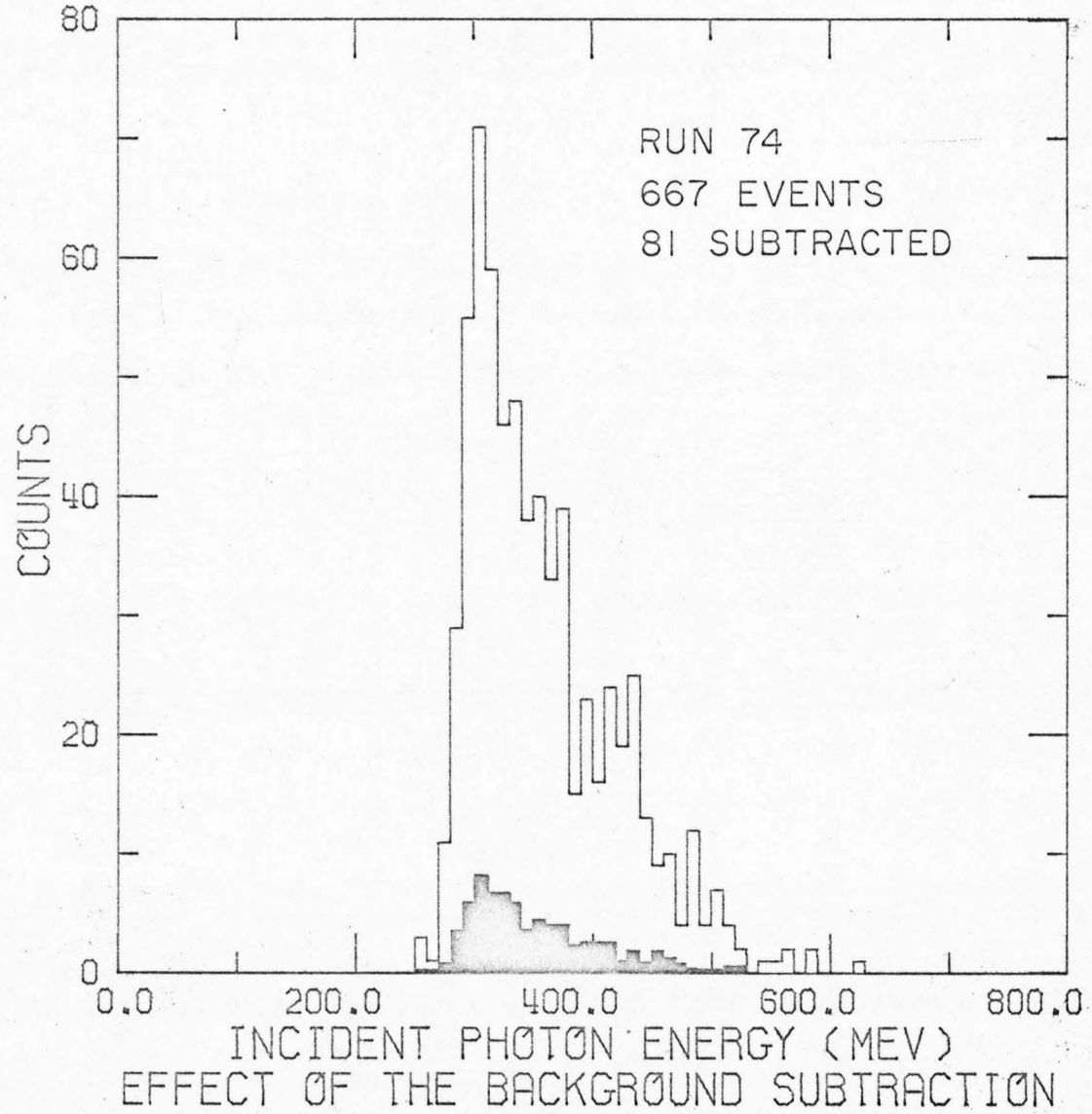
80
60
40
20
0
COUNTS
RUN 74
667 EVENTS
81 SUBTRACTED
0.0
200.0
400.0
600.0
800.0
INCIDENT PHOTON ENERGY (MEV)
EFFECT OF THE BACKGROUND SUBTRACTION

Figure 3.8

Therefore, we conclude that events originating in the target walls contribute only to the background as discussed earlier in this section. The background subtraction has already corrected for events of this type, so no additional empty-target subtraction was made.

D. Efficiency Calculations

In the previous sections of this chapter, the method of analysing the raw data has been explained. The numbers of events of the reaction $\gamma + He^3 \rightarrow p + d$ which result from this analysis cannot be immediately converted into cross-sections. We must know, among other things, with what probability the apparatus detected such events. Several factors influence this probability, or efficiency, as it is called.

1. The solid angle subtended by the apparatus.

2. The momentum acceptance of the magnet.

3. The effect of secondary nuclear interactions which might prevent the protons and deuterons from reaching the detectors.

4. The efficiency of the scintillation counters and associated electronics.

5. The efficiency of the wire spark chamber system.

We now discuss the calculation of each of these effects in turn. The first two are considered together.

1. Geometric Efficiency and Momentum Acceptance.

The geometric efficiency of the apparatus is the probability that the final state particles of a $\gamma + He^3 \rightarrow p + d$ event pass through all the scintillation counters required for the 'signature' of the event (see Chapter II, Section C). This probability depends on basic kinematic parameters of the event, the photon energy and the scattering angle, as well as the properties of the apparatus.

Several features complicate the efficiency calculation. The intersection of the photon beam with the $He^3$ target occupies a finite volume. Particles passing through the magnet have curved trajectories. Multiple Coulomb scattering causes small deflections in all trajectories and the energy loss in such collisions could prevent particles from reaching the detectors in certain cases. There is a corresponding effect due to nuclear scattering; however, it will be considered separately. Finally, as the experimental cross-sections are to be expressed in the $\gamma$ - $He^3$ center of mass frame, the efficiency calculation must be done in this frame also.

It is impossible to make an exact calculation which takes the above features into account. Therefore, a Monte Carlo computer program was used. The steps in the calculation of the efficiency averaged over a 10 MeV bin at one setting of the apparatus are:

1. Determine an upper limit on the solid angle subtended by counters MS2 and RS1 as viewed in the $\gamma$ - $He^3$ center of mass frame. It was convenient to take this limit as a region bounded by four surfaces,

two of constant $\phi$, and two of constant $\theta$, in a spherical coordinate system with origin at the center of the target and z axis along the photon beam. The surfaces were chosen so as to contain all possible straight lines passing through both the target and the counters.

2. Using a random number generator, events were generated by choosing

- a random photon energy within the 10 MeV bin;
- a random event origin within the target such that the radial (in cylindrical coordinates) distribution of events reproduces the shape given in Appendix D;
- a random $\phi$ within the limits defined in step 1;
- a random cos $\theta$ within the limits defined in step 1.

3. Each event was transformed to the laboratory frame where several tests were applied to determine whether it could be detected:

- Did the tracks pass through counters MS2 and RS1?
- Did the track in the magnet array pass through the pole tips and counter MS3? To answer this, the results of the magnet calibration discussed in Appendix G were used.
- Did the energy loss due to Coulomb interactions prevent the particles from passing through the entire apparatus? (For this, the range-energy relations for protons and deuterons were extracted from calculations by Janni[30].)

4. The fraction of successful events was multiplied by the solid angle within the $\theta$ and $\phi$ limits set in step 1. This number is the geometric detection efficiency. A typical value was 0.005 steradians.

In the calculation as outlined, no correction was made for the angular deflection of the tracks caused by multiple Coulomb scattering. A separate calculation including this effect showed that, to within 1%, as many particles would scatter into the apparatus as scatter out of it. As this calculation was about twice as expensive as the one outlined, it was not performed for all settings.

The statistical error of the calculation is given by

$$\text{relative error} = \frac{1}{\sqrt{\text{successes}}} \cdot \sqrt{\frac{\text{failures}}{\text{attempts} - 1}}$$

where 'attempts,' 'successes' and 'failures' refer to the numbers of such events generated in the Monte Carlo calculation. This is, of course, the error associated with the determination of a quantity obeying a binomial distribution. For the same number of attempts, the calculation is more accurate the higher the fraction of successes. By choosing the $\theta$ and $\phi$ limits (step 1) to be as small as possible, the greatest accuracy per dollar spent was obtained.

Figure 3.9 shows the calculated efficiency as a function of photon energy for setting 14, at which run 74 was made. The ordinate is not the effective solid angle of the apparatus, but this quantity divided by $4\pi$. For each bin in photon energy, 10,000 events were generated. This gives the calculation an accuracy of about 2.5% for the bins with large efficiency. When averages are taken over five adjacent bins, the accuracy will be roughly 1%.

There are several sources of systematic uncertainty in the efficiency calculation:

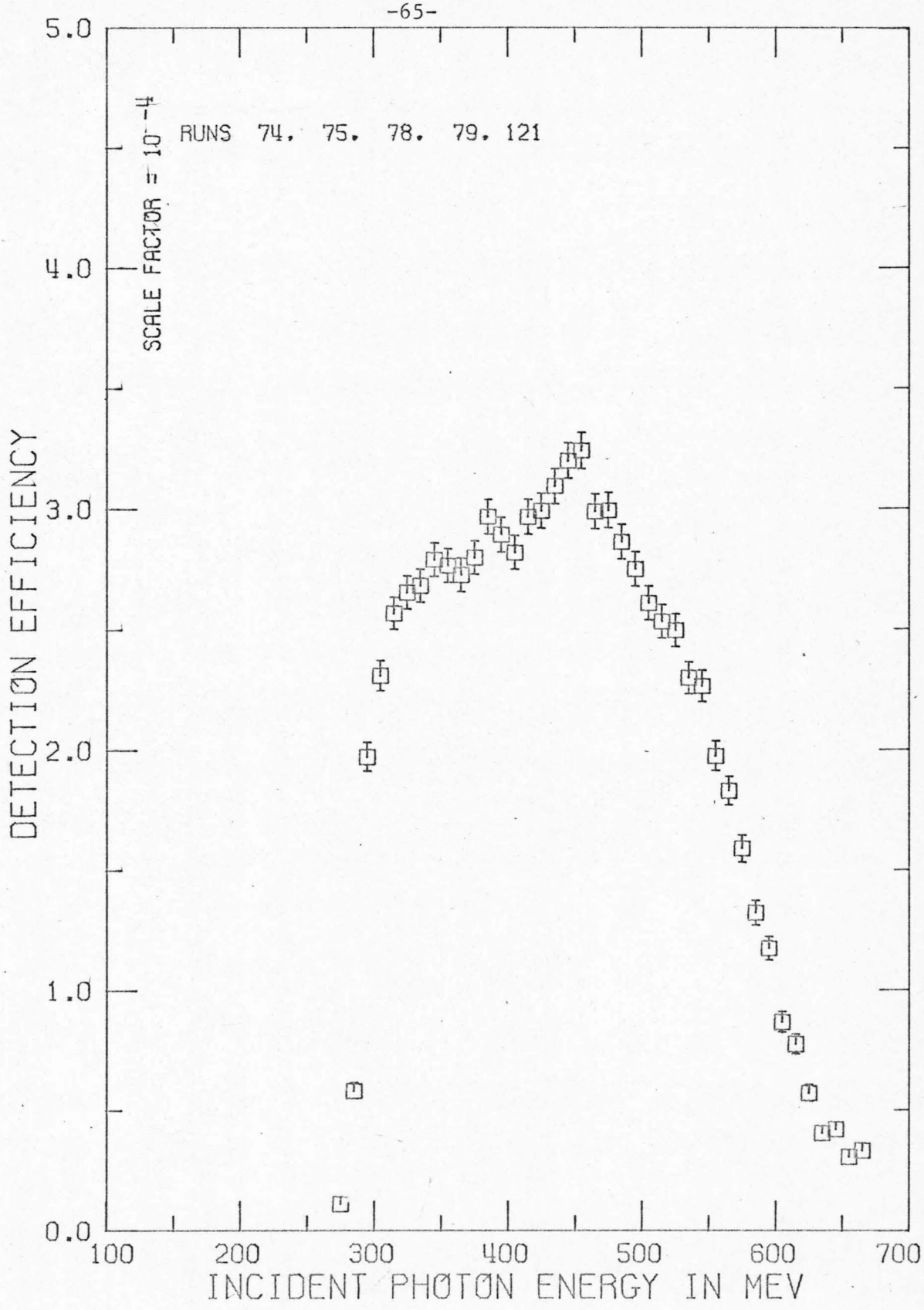


Figure 3.9 Example of the Monte Carlo Efficiency Calculation

1. 3% due to uncertainty in the defocusing effect of the magnet's fringe field (see Appendix G).
2. 2% due to uncertainty in the effective vertical aperture in the magnet field.
3. 1% due to uncertainty in the target position of 0.05 inches.
4. 0.5% due to possible error of 0.1 inches in size and position of counter MS2.
5. 0.5% due to same effect for counter MS3.

The maximum system uncertainty is estimated to be 7%.

2. Nuclear Scattering

A significant fraction of the protons and deuterons produced by the reaction $\gamma + He^3 \rightarrow p + d$ scattered off some atomic nucleus in the detection apparatus. If such a scattering caused a large change in the energy or angle of the particle, the $\gamma + He^3 \rightarrow p + d$ event would go undetected. A correction was made for this inefficiency, as described below.

There are four cases to consider: either protons or deuterons lost in either the magnet or range arrays. An extra complication in the case of deuterons is the 'stripping' process in which the deuteron breaks up into a proton and a neutron.

In the magnet array, a scatter of $3^o$ or more (on the average) occurring before the magnet causes the event to be lost as the solid angle of the apparatus is very small. For scatters less than $3^o$, a track can still be reconstructed no matter where it occurs. In these cases, the coplanarity, or momentum (and hence missing mass excess), or both, will be in error. However, the deviations are within the widths on the quantities used to define the foreground event sample. If a deuteron underwent stripping with the resulting proton at less than $3^o$ to the deuteron, the event is still lost, since the proton would have only roughly half the momentum of the deuteron. Scatters which occur after the magnet are not so detrimental. A scatter which occurred in counters MS3 or MS4 was harmless; the event would still be detected. There was very little matter between the magnet and counter MS3 to cause a scatter, so for ease of calculation, the $3^o$ criterion was applied to

this region also.

In the range array, only the deflection of a particle can cause the event to be lost. A stripped deuteron is still detected if the proton goes forward; the pulse heights in a scintillator are the same for a deuteron and for a proton of half the kinetic energy. A deflection of greater than $5^{o}$ was considered to eliminate the event, based on the width of the coplanarity used in defining the foreground event sample. Also, the scatter would have to occur before counter RS1 to have any effect.

To calculate the probability of a scatter, empirical fits to proton-nucleous and deuteron-nucleous cross-sections were made[31]:

$$(pA) = A^{-0.26}(A(pp) + (A-Z)(pn))$$

$$(nA) = 1.2A^{-0.17}(Z(np) + (A-Z)(pp))$$

$$(dA) = ((pA) + (nA)) \cdot \begin{cases} 0.83 & \text{- magnet array} \\ 0.56 & \text{- range array} \end{cases}$$

where A = atomic number of the nucleus,

Z = charge of the nucleus

and (pA) = proton-nucleus cross-section, etc.

Using these fits, the probability of nuclear scattering was calculated for each setting of the apparatus in steps of 10 MeV incident photon energy. Most of the scattering occurred in the magnet array, which contained more material. The average correction was about 15% although it reached 40% for a few bins at low energies and small angles. I estimate a 5% accuracy in the fits, so the resulting systematic error in the $\gamma + He^{3} \rightarrow p + d$ cross-sections is about 1%.

3. Electronic Inefficiencies

In this section, we consider the fraction of events which went unrecorded due to inefficiencies in the trigger electronics.

The scintillation counters were better than 99% efficient in the detection of charged particles, and no correction was made for any loss of events in the counters themselves. Likewise, the electronics were reliable in putting out a signal whenever an input was present, provided the input signal did not occur during the dead-time caused by a previous signal. The circuits whose dead-times determined the inefficiencies were the TVD-3B discriminators (see Chapter II, Section C). Their dead-time was twenty nanoseconds. Signals were accepted by the electronics only during the sixty millisecond intervals during which the photon beam was incident on the $He^3$ target. The number of beam pulses in each run and the total counts observed in the various scintillation counters are combined to predict the loss rate. Only counters MS1, RS1 and RS2 experienced high enough counting rates for the loss to be significant. The average electronic inefficiency for all three counters combined was about 1%, reaching 3% for runs with the apparatus at small angles to the photon beam.

4. Wire Spark Chamber Inefficiencies

The last type of inefficiency we consider is that of the wire spark chamber system. The sources of possible inefficiencies were background electrons in the chambers, bad chamber gas, bad magnetostrictive ribbons, maladjusted want amplifiers, etc. These effects were not calculated separately, but rather methods were devised that estimated the combined effect of all sources of inefficiency.

The measure of chamber efficiency is defined to be the fraction of foreground events detectable by the apparatus which also were reconstructed according to the procedures discussed in Sections A and B of this chapter. Since the true number of foreground events is not known, the efficiency must be estimated by assuming it equal to some measureable quantity.

The first method of estimation, and the one which was used in the calculation of the cross-section, is as follows. First, a sample with a high percentage of foreground events is chosen on the basis of a scintillator pulse heights and the time-of-flight measurement. Of these, a certain fraction are also 'reconstructible'. This fraction is the exact measure of the chamber efficiency for the sample as defined. We estimate that the efficiency for the entire foreground event sample has the same value.

It is quite possible that the chamber efficiency is different for background than for foreground events. The sensitivity of our estimate to this effect can be checked by varying the pulse height requirements of the test sample. The calculated efficiencies of various

samples with from ten to ninety percent foreground events vary by only two percent. That is, the chamber efficiency is the same for background and foreground events with similar pulse heights (ionization).

The above method is the simplest and most direct, since it bases the estimate on the exact, observed efficiency for a sample of events very similar to the desired sample. A further advantage of this method is that it includes the effect of any possible inefficiency in the track finding computer program. As a measure of the uncertainty of the estimate, a statistical error is assigned to the efficiency as if it were an observation of a binomially distributed process.

The efficiencies estimated by this method varied from 85% to 30%, depending on the run, and averaged about 65%. The statistical uncertainties ranged from about 1% to 10%, depending on the number of events in the particular run.

As a check on this method, a second one was devised. In it, the inefficiency of each wand was calculated and then the separate inefficiencies were combined into an overall efficiency. The wand inefficiency was calculated by observing the fraction of events for which no spark was found within 0.1" of a reconstructed track. An error was assigned to the determination, assuming the process to obey a binomial distribution. To estimate the overall inefficiency, at least three sparks were required to define a track. For example, the individual wand inefficiencies were used to calculate the probability that in five chambers the first three had sparks but the last two did not,

and so on for all possible combinations. The overall inefficiency is the sum of these probabilities. An error for this overall inefficiency was calculated by combining in the proper fashion the errors assigned to the wand inefficiencies.

The results of the second method agreed with those of the first to within the assigned errors. The errors were greater for the second method due to the large number of combinations which contribute to the result. Further, the second method was found to be quite sensitive to the choice of 0.1" as the allowed discrepancy between a 'good' spark and a track. This is somewhat surprising as the spread of sparks from the corresponding tracks in a chamber that was working well was about 0.02". I believe the trouble was due to intermittent signals prior to the first fiducial signals on certain wands. In any case, it was felt that the first method was more reliable than the second, and the former was used exclusively for the results presented.

E. Cross-Sections and Statistical Errors

In this section, the expressions for calculating the differential cross-sections and associated statistical errors are summarized.

The data collected in this experiment have been grouped into bins 10 MeV width in incident photon energy, and as wide in angle as the acceptance of the magnet array - about $4^{\circ}$. The number of events in such a bin is related to the differential cross section by

$$N(K,\theta) = \frac{d\sigma}{d\Omega}(K,\theta)\cdot N_{He^3}\cdot N_{\gamma}(K)\ \Delta K\cdot 4\pi\eta(K,\theta),$$

where $K$ = central photon energy of the bin;

$\Delta K$ = 10 MeV;

$\theta$ = central proton angle of the bin (c.m. frame);

$\frac{d\sigma}{d\Omega}$ = differential cross-section in $cm^2$;

$N_{He^3}$ = number of $He^3$ nuclei/$cm^2$,

= $6.024 \times 10^{23}$ · length of target/molar volume of $He^3$; also included are the (small) effects due to $He^4$ in the $He^3$ sample - see Appendix F;

$N_{\gamma}(K)$ = number of incident photons per unit energy interval,

$$= \frac{\text{total energy of beam}}{K_{max}} \qquad \frac{\text{bremsstrahlung spectrum function}}{K}$$

See Appendices D and E for details;

$\eta(K,\theta)$ = efficiency for detecting an event. $0 \leq \eta \leq 1$

= geometric efficiency x probability of no nuclear scattering x electronic efficiency x spark chamber efficiency.

The factor $4\pi$ converts the efficiency $\eta$, into an effective solid angle.

Analysis of the experimental data does not directly yield the number of events, N, because of background processes. As discussed in Section C above,

$$N = N_I - N_o \cdot M_I/M_o$$

where $N_I$ = number of events inside the foreground region,

$N_o$ = number of events outside the foreground region,

$M_I/M_o$ = ratio of number of background events inside the foreground region to the number outside; determined by a Monte Carlo calculation.

The cross-section for a single bin in K and $\theta$ would then be

$$\frac{d\sigma}{d\Omega} = N/N_{He^3} \cdot N_\gamma \, \Delta K \cdot 4\pi\eta \ .$$

In the experiment, data for a single bin were taken during several runs, which in general had different values for all of the parameters in the above expression. The proper way to combine the data from the several runs is indicated by an application of the maximum likelihood method. The expected number of events to be observed in run i is governed by a Poisson distribution:

$$P(N_i) = \frac{(\sigma\eta_i)^{N_i} e^{-\sigma N_i}}{(N_i)!} \ ,$$

where $\sigma$ abbreviates $d\sigma/d\Omega$,

and $\eta_i$ abbreviates all of the remaining factors relating $N_i$ and $\sigma$ for run i.

The probability of observing the set of values $\{N_i\}$ is the likelihood function

$$L(\sigma) = \prod_i \frac{(\sigma\eta_i)^{N_i} e^{-\sigma\eta_i}}{(N_i)!} \ .$$

The maximum likelihood method consists of taking as the best estimate of $\sigma$ that value which maximizes $L(\sigma)$. Thus,

$$\sigma = \sum_i N_i / \sum \eta_i .$$

This is just the simple result that the cross-section is given by the average number of events per run divided by the average efficiency.

The statistical error in the determination of the cross-section may now be calculated. If the only source of error was that of the statistics of the Poisson distribution, the maximum likelihood method would imply

$$\text{error} = \sqrt{\sum N_i / \sum \eta_i} \ .$$

The other sources of error were:

1. The background subtraction - Section C.
2. The geometric efficiency calculation - Section D.1.
3. The spark chamber efficiency calculation - Section D.4.
4. Beam monitoring - Appendix E.
5. Target density fluctuations - Appendix F.

The complete expression for the relative statistical error is

$$(\text{relative error})^2 = \frac{\sum_i \eta_i^2 (E_{G,i}^2 + E_{C,i}^2 + E_{B,i}^2 + E_{T,i}^2)}{(\sum \eta_i)^2} + \frac{\sum_i (N_{I,i} + (N_{o,i} M_{I,i} / M_{o,i})^2 (1/N_{o,i} + 1/M_{o,i} + 1/M_{I,i}))}{(\sum_i N_i)^2} ,$$

where i labels the run,

and $E_G$ = relative error in the geometric efficiency,

$E_C$ = relative error in the chamber efficiency,

$E_B$ = relative error in the beam monitoring,

$E_T$ = relative error in the target density.

F. Systematic Errors and Resolution

There are three sources of possible systematic error greater than 1%.

1. 7% in the geometric efficiency calculation (Section D).
2. 5% in the absolute calibration of the beam monitors (Appendix D).
3. 1% in the nuclear scattering correction, from a 5% error in a 15% correction (Section D.4).

Thus the absolute cross-sections might be in error up to 13%, assuming all the effects had the same sign. If the uncertainties are combined in quadrature, the result is 6%. This uncertainty does not affect the shape of the differential cross-sections.

As the differential cross-section is a relatively steep function of energy and angle, poor resolution of these quantities could cause a systematic error. The question of angular resolution is the simpler. All events accepted in one setting of the apparatus are lumped together into one bin. Including the effect of multiple Coulomb scattering, the resulting bin is at most $5^{o}$ wide, and the event population is essentially symmetrical about the center of the bin. Hence it is a good approximation to average the cross-section over the entire bin and report the result as that at the central angle.

As discussed in Section B above, the incident photon energy is reconstructed from the lab angle and momentum of the particle detected in the magnet array. The dependence on the lab angle is small; an

error of $0.5^{o}$ due to multiple Coulomb scattering causes only about a 0.1% shift in the calculated photon energy. However, a 1% error in the momentum causes nearly 2% error in the photon energy. There are three possible causes of error in the determination of the momentum; uncertainty in the magnetic field strength, the error of the momentum fit, and the multiple scattering a particle suffers between the front and rear magnet spark chamber arrays. The magnetic field strength was held constant to within 0.1% during each run by current regulated power supplies. The current in the magnet was monitored, rather than the magnetic field itself. The hysteresis of the magnet could cause up to 1% error in the calculation of the magnetic field strength. This would appear as a 2% systematic error in the photon energy for all runs at a given setting taken between adjustment of the magnet current. As the cross-section varies rapidly with energy, this has the effect of causing a slight normalization error between different runs at the same setting. The data from three runs (out of about 100) were discarded due to anomalous normalizations compared to other runs at the same settings. If an overall 1% error remains in the magnetic field strength averaged over the various runs, this would cause a 3% systematic error in the cross-sections, using the observed energy dependence of roughly EXP (-0.01* $E\gamma$). This effect would most likely affect the shape of the angular distributions, as it is different at different settings.

The accuracy of the momentum fit is 0.2% (r.m.s.) as discussed in Appendix G. Multiple Coulomb scattering causes an error in the momentum of 0.5% to 1.5% depending on the setting. These errors are

random and produce only a slight systematic effect. However, as a 1.5% shift in momentum caused a 10 MeV shift in the photon energy at 300 MeV, the data were binned into 10 MeV bins, this size being commensurate with the resolution in photon energy.

Another aspect of the experimental resolution is the observed spread in the coplanarity and missing mass excess (Section C). This is well accounted for by the effect of multiple Coulomb scattering. Typical values of r.m.s. Coulomb scattering are $0.5^{o}$ for protons and $1.0^{o}$ for deuterons, yielding a r.m.s. width of $1.2^{o}$ for the coplanarity and about 20 MeV for the mass excess, using the expression given in Section C for the latter. The effect on the mass excess of uncertainty in the momentum of the particle in the magnet is slight.

# IV. RESULTS

The differential cross-sections for the reaction $\gamma + He^3 \rightarrow p + d$ have been extracted from the data according to the method given in Section E of Chapter III. The systematic uncertainty of the results is about 10%, as discussed in Section F of Chapter III.

Figure 4.1 shows the differential cross-section as a function of photon energy at the various center of mass frame angles of the proton which were observed. Each point is the average over a 10 MeV spread in energy and $4^o$ in angle, centered at the values as plotted. The vertical error bars are the statistical uncertainties assigned to each cross-section. The cross-sections for each angle have their own log scale on the left, each scale reaching a maximum of one microbarn per steradian. The data plotted with a circular symbol are from runs in which a proton was detected in the magnet array; the square symbols represent data with a deuteron detected in this array. Data for both cases were collected at $90^o$; the cross-sections are seen to agree well with one another there.

The statistical accuracy of the cross-sections as binned in 10 MeV steps is not high. To suppress the effect of fluctuations, all further consideration of the data will be for bins of 50 MeV in photon energy. Figure 4.2 shows the differential cross-sections plotted in this way. Otherwise, the plot is the same as Figure 4.1. The logarthmic scale obscures the true size of the error bars.

Table 4.1 lists the cross-sections and statistical errors as a

function of angle and photon energy. These are the main results of the experiment.

Figures 4.3 through 4.9 show the differential cross-sections as a function of proton center of mass angle for photon energies from 250 to 550 MeV. Again, the results at a given photon energy are the averages over the data from ± 25 MeV about the central value. The units of the ordinate are arbitrary; the purpose of the figures is to display the shapes of the various angular distributions.

The smooth curves shown in these figures are fits of the form

$$A + B\cos\theta + \sin^2\theta(C + D\cos\theta + E\cos^2\theta).$$

The relative values of the five parameters A,...E are listed in Table 4.2. The fits at 250 and 300 MeV went negative at the extreme angles if left unconstrained. They have been required to remain non-negative, with the result that the fits go to zero at large and small angles, as shown in Figures 4.3 and 4.4. These constrained fits are not very good in the $\chi^2$ sense.

All of the cross-sections and the fits are shown on a single semilog graph, Figure 4.10, except for the data at 550 MeV.

The fits may be integrated to yield total cross-sections, which are shown in Figure 4.11. The values and statistical errors of the total cross-sections are also listed in Table 4.2. Due to the pathologies of the fits at 250 and 300 MeV, the estimated total cross-sections at these energies are very probably too small.

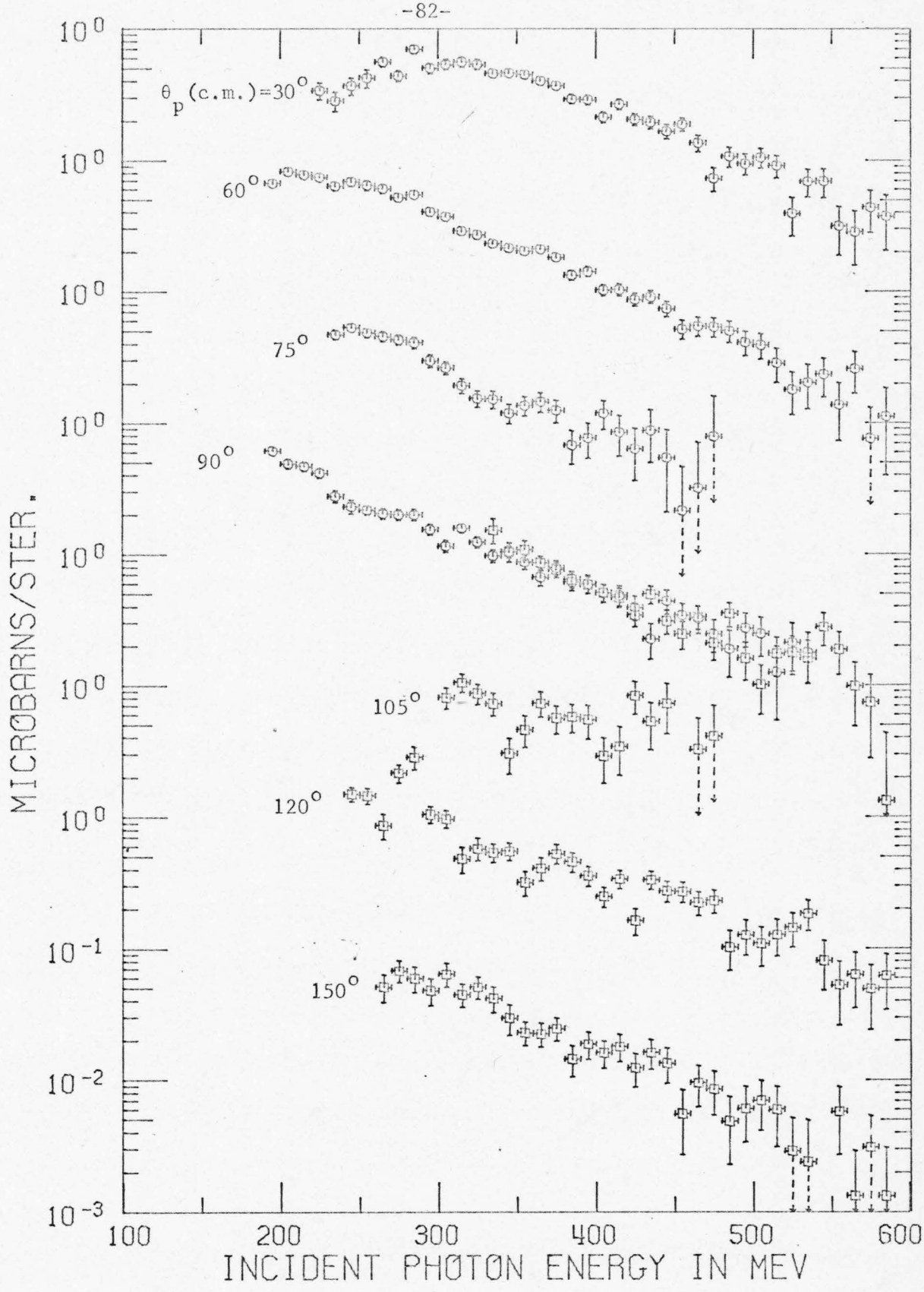


Figure 4.1 $He^3$ Photodisintegration Differential Cross-Sections in 10 MeV Bins

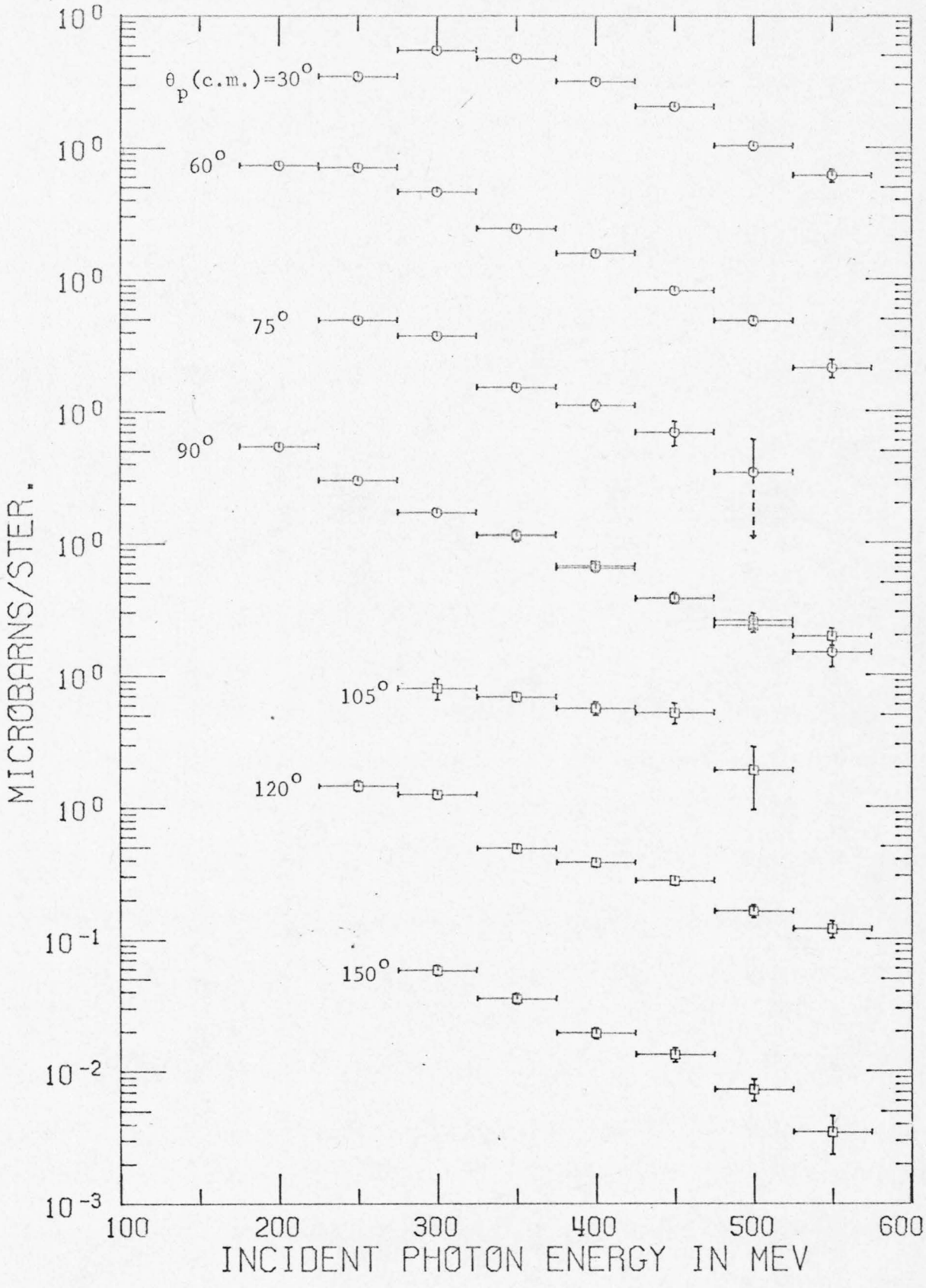


Figure 4.2 $He^3$ Photodisintegration Differential Cross-Sections in 50 MeV Bins

Table 4.1

Differential Cross-Sections for $\gamma + He^3 \rightarrow p + d$
in Microbands/Steradian

| $E_\gamma$ (MeV) | 30° | 60° | 75° | 90° proton in magnet | 90° deuteron in magnet | 105° | 120° | 150° |
|---|---|---|---|---|---|---|---|---|
| 200 | | 0.730± 0.035 | | 0.540± 0.029 | | | | |
| 250 | 0.348± 0.027 | 0.701± 0.023 | 0.490± 0.022 | 0.297± 0.012 | | | 0.145± 0.013 | |
| 300 | 0.546± 0.021 | 0.460± 0.012 | 0.372± 0.016 | 0.169± 0.007 | | 0.079± 0.014 | 0.127± 0.010 | 0.058± 0.006 |
| 350 | 0.483± 0.016 | 0.244± 0.007 | 0.153± 0.010 | 0.117± 0.005 | 0.115± 0.012 | 0.069± 0.006 | 0.055± 0.005 | 0.037± 0.004 |
| 400 | 0.327± 0.012 | 0.158± 0.005 | 0.110± 0.011 | 0.067± 0.004 | 0.067± 0.004 | 0.063± 0.007 | 0.042± 0.003 | 0.021± 0.002 |
| 450 | 0.215± 0.010 | 0.084± 0.005 | 0.085± 0.017 | 0.042± 0.004 | 0.039± 0.003 | 0.068± 0.012 | 0.032± 0.003 | 0.016± 0.002 |
| 500 | 0.119± 0.009 | 0.055± 0.005 | | 0.032± 0.004 | 0.027± 0.003 | | 0.020± 0.002 | 0.010± 0.002 |
| 550 | 0.090± 0.010 | 0.029± 0.004 | | 0.019± 0.004 | 0.022± 0.003 | | 0.014± 0.002 | 0.007± 0.002 |

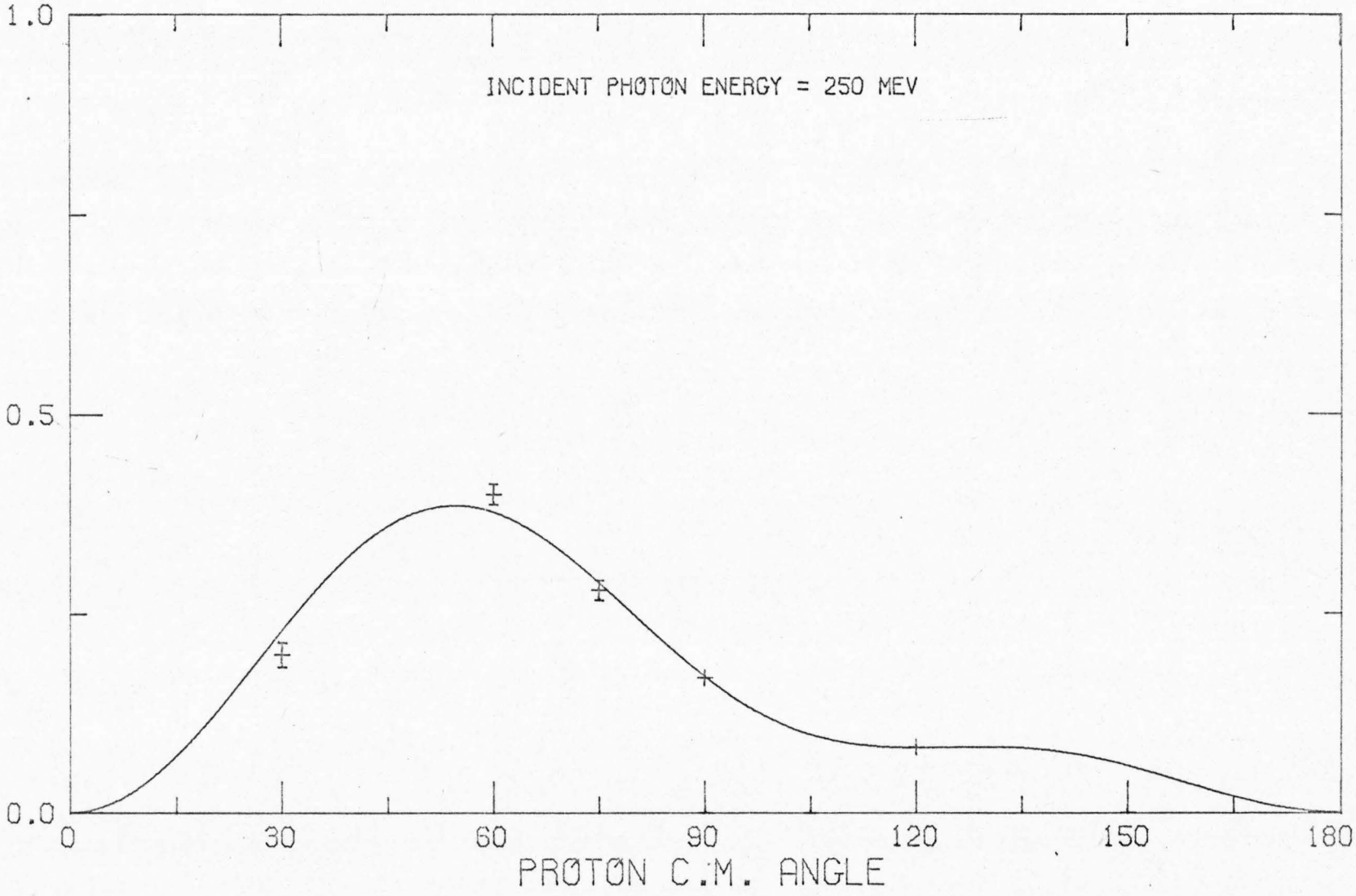


Figure 4.3 $He^3$ Photodisintegration Angular Distribution at 250 MeV

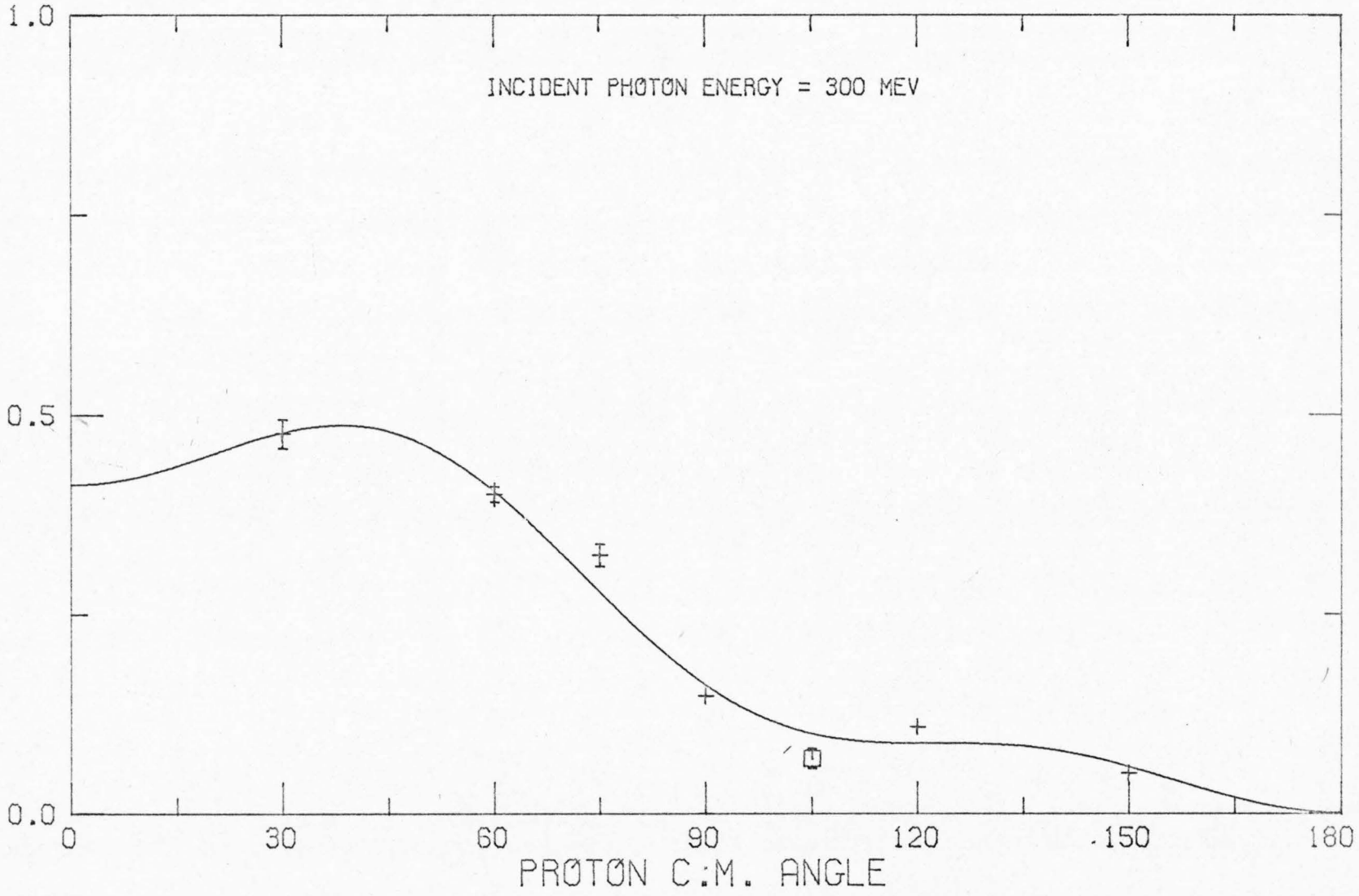


Figure 4.4 $He^3$ Photodisintegration Angular Distribution at 300 MeV

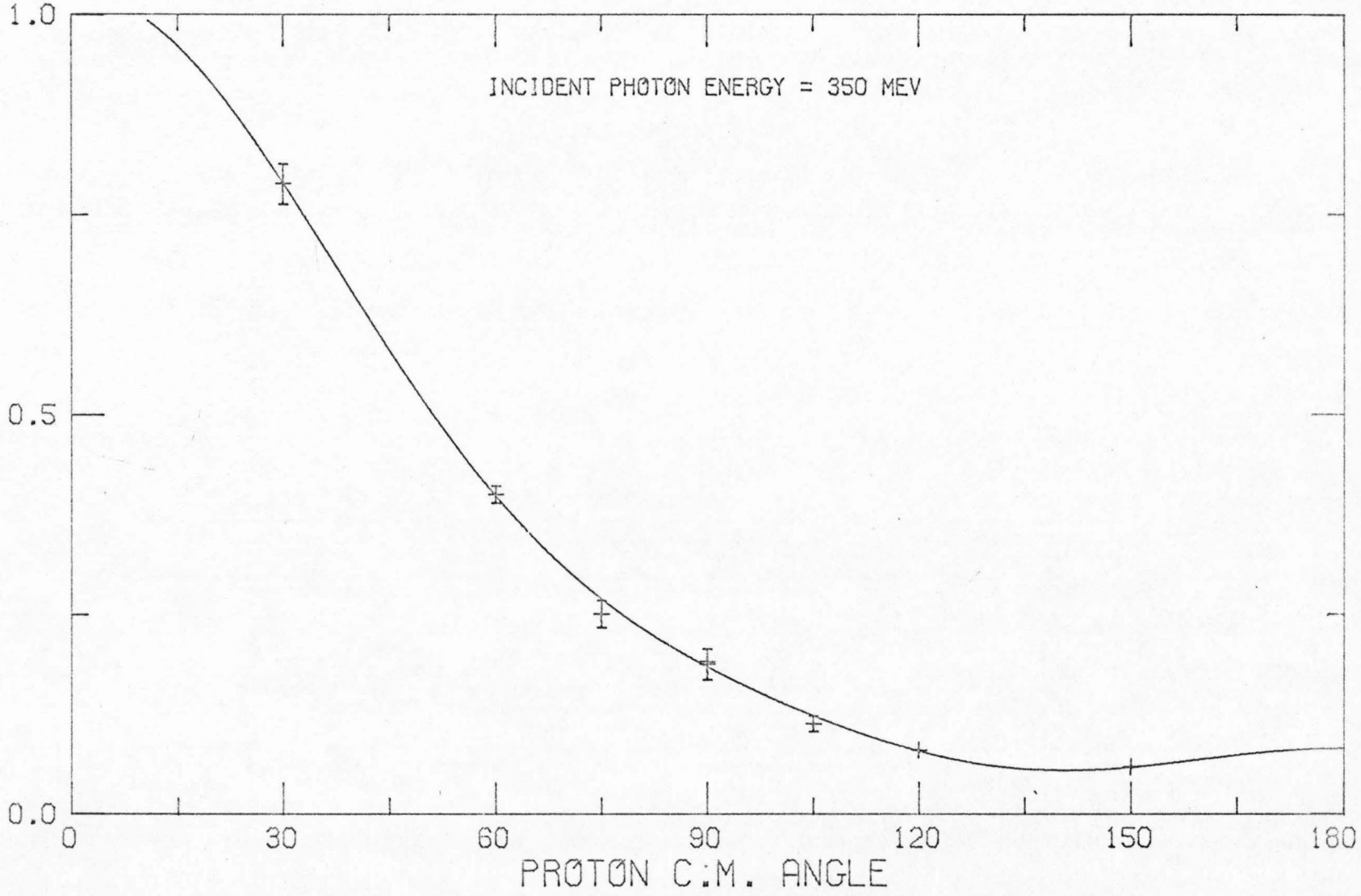


Figure 4.5 $He^3$ Photodisintegration Angular Distribution at 350 MeV

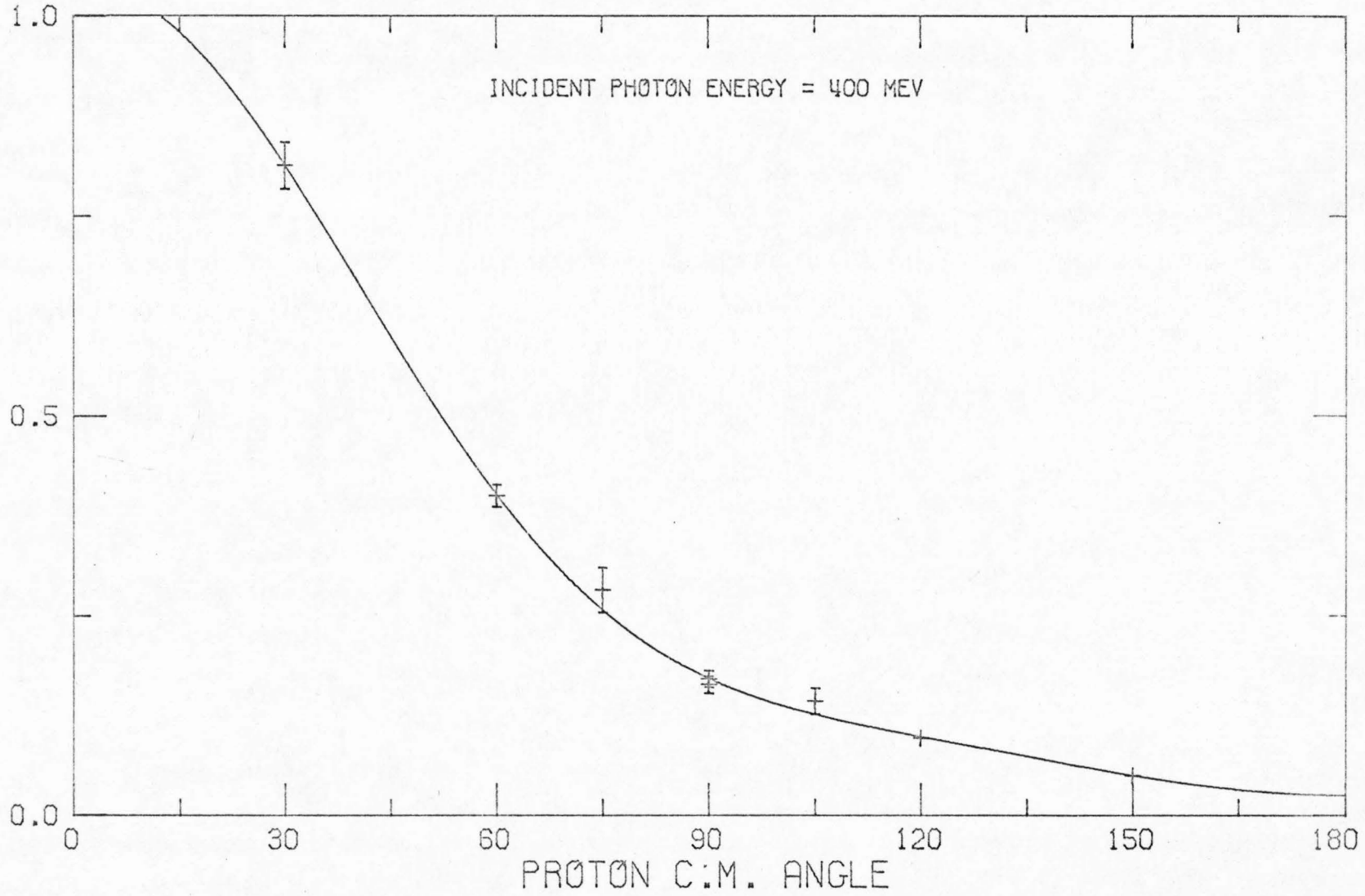


Figure 4.6 $He^3$ Photodisintegration Angular Distribution at 400 MeV

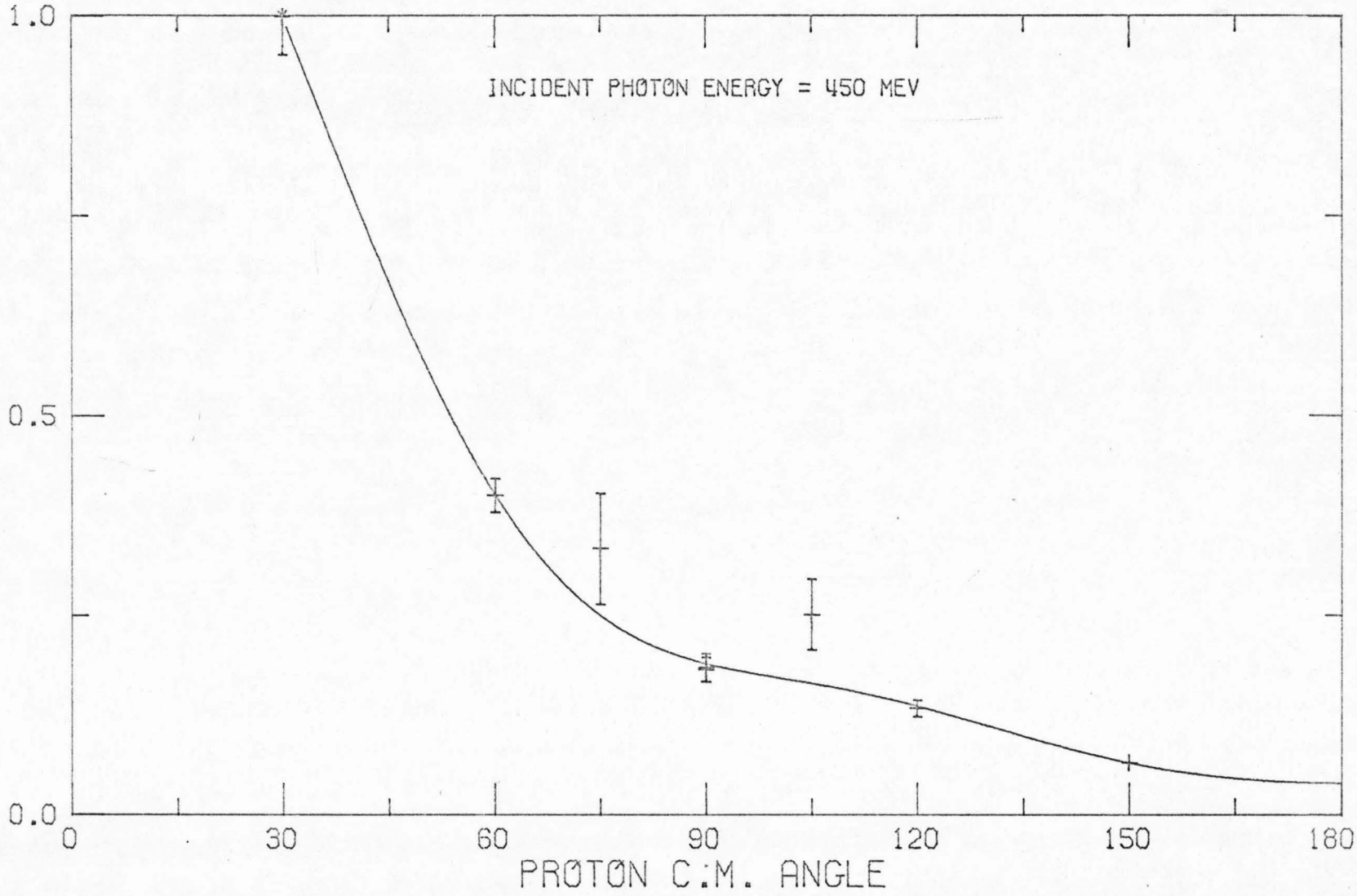


Figure 4.7 $He^3$ Photodisintegration Angular Distribution at 450 MeV

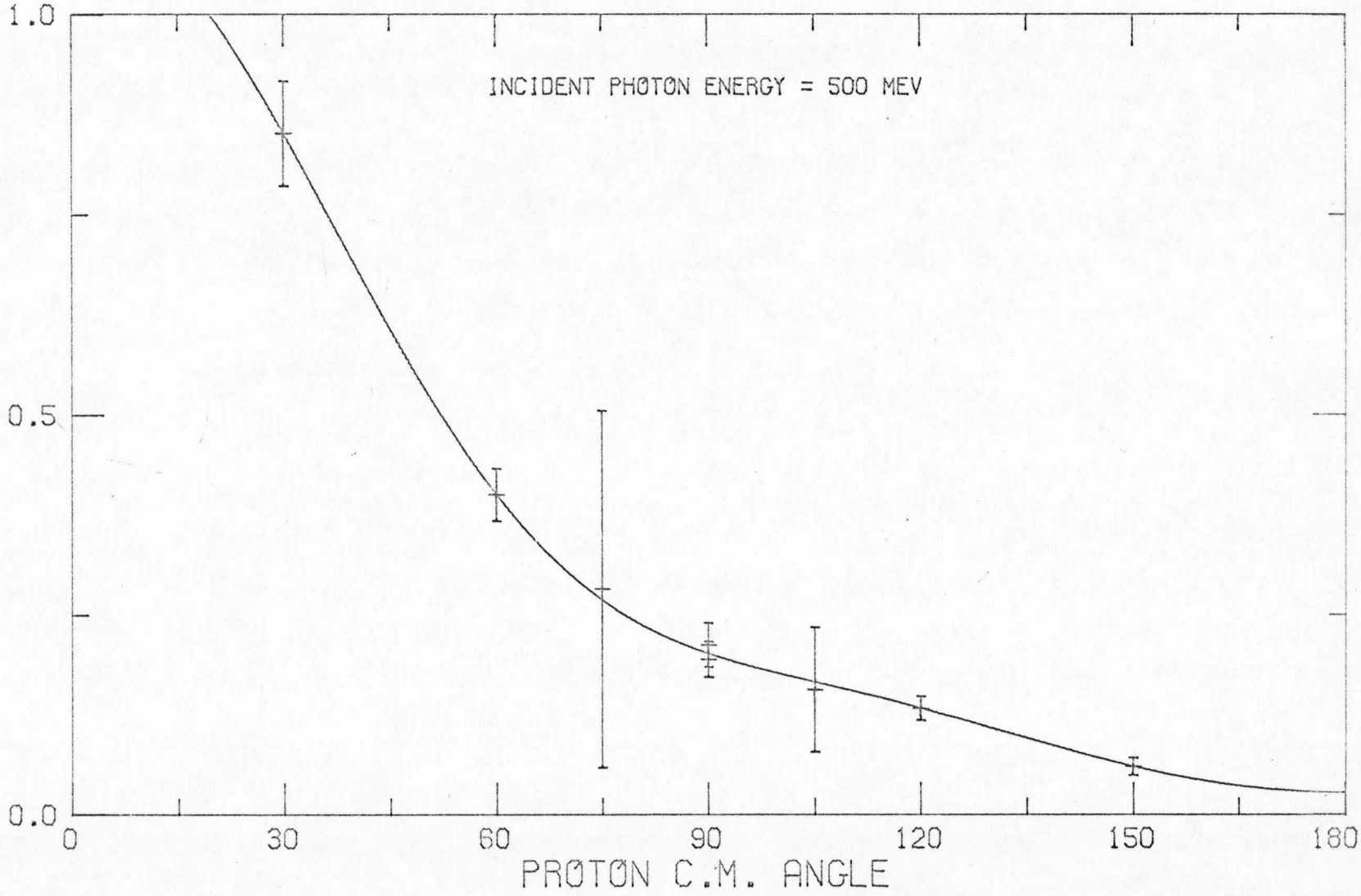


Figure 4.8 $He^3$ Photodisintegration Angular Distribution at 500 MeV

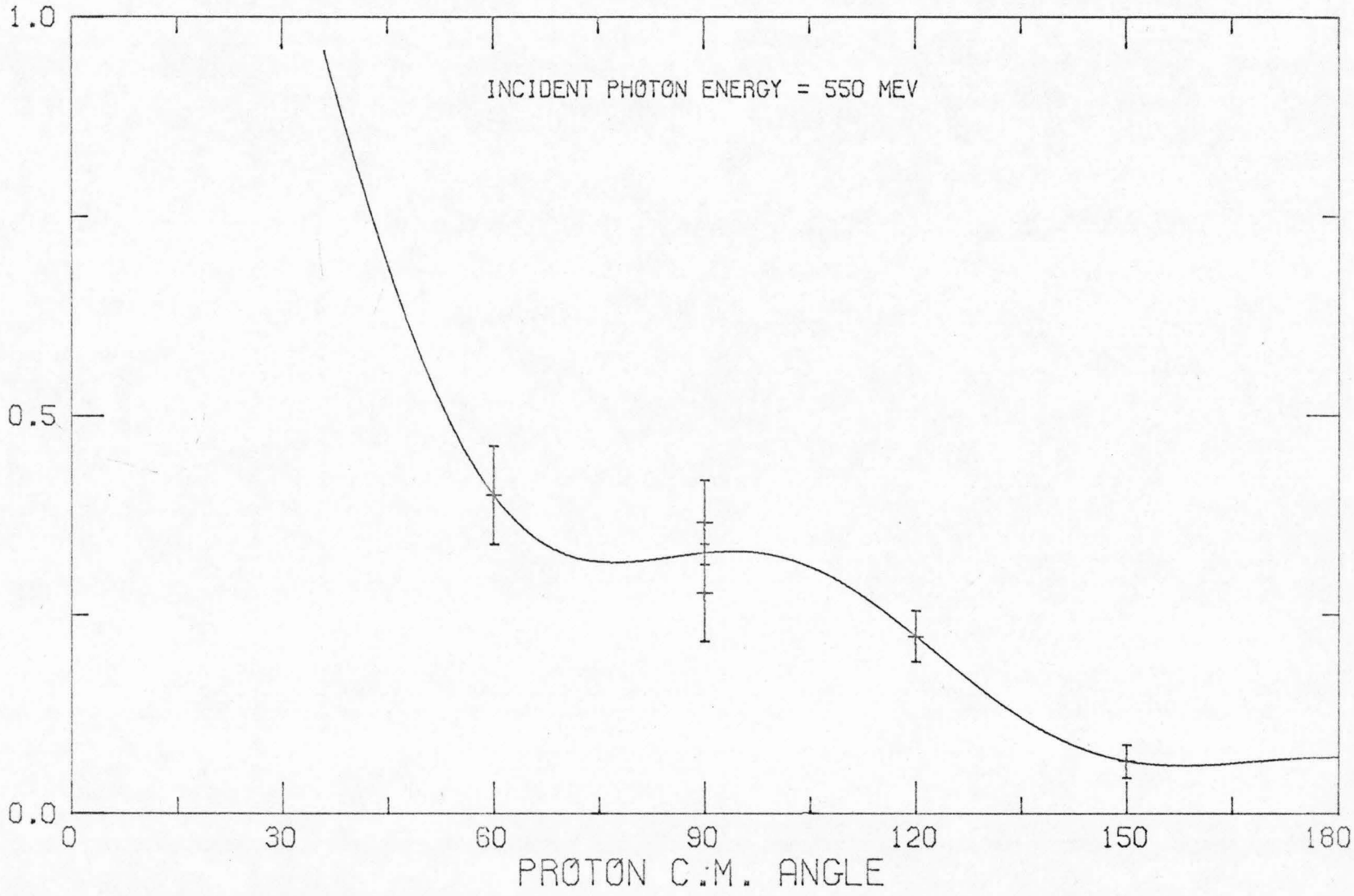


Figure 4.9 $He^3$ Photodisintegration Angular Distribution at 550 MeV

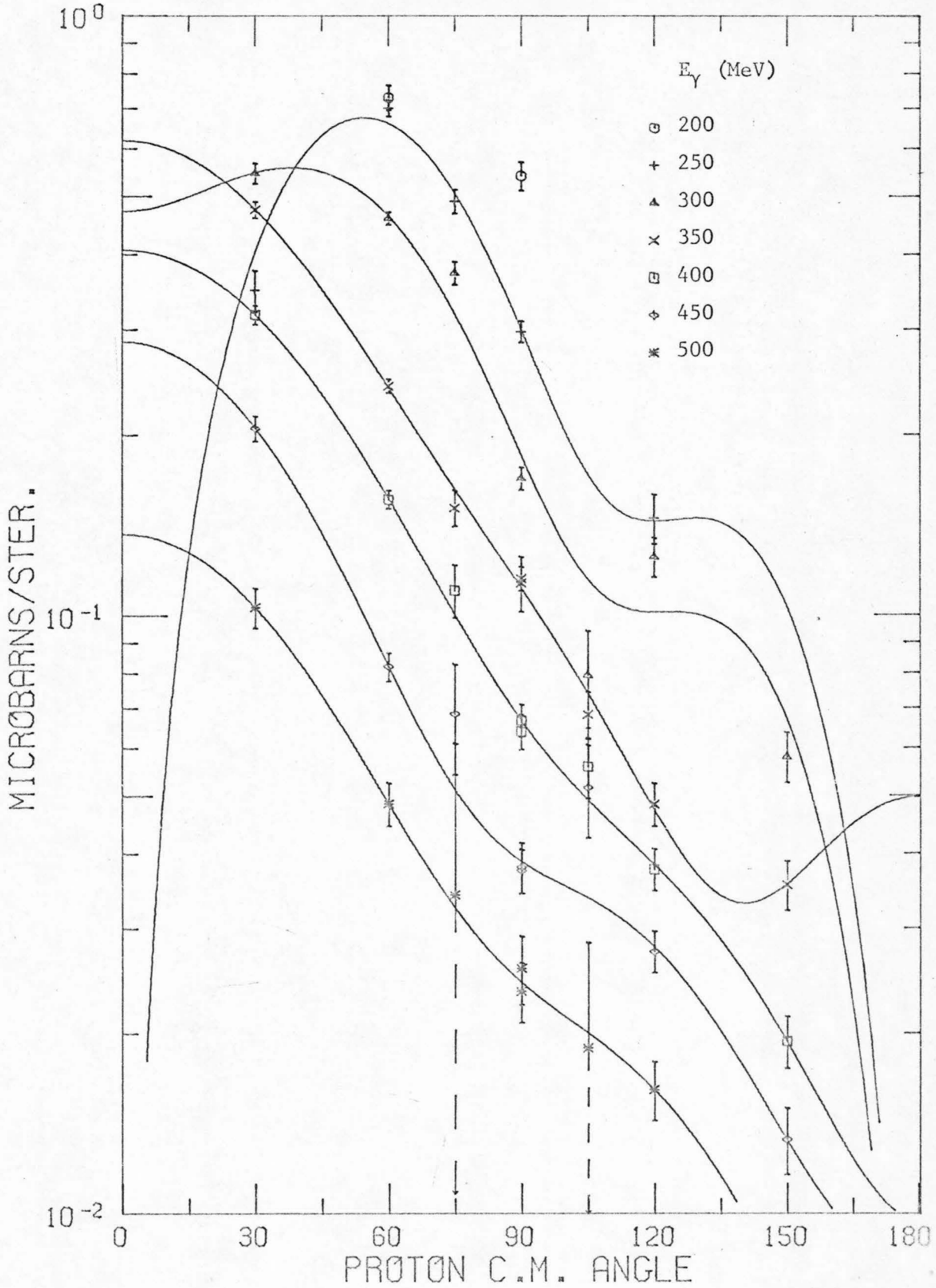


Figure 4.10 Summary of $He^3$ Photodisintegration Angular Distributions and Fits

Table 4.2

Parametrization of the Cross-Sections of $\gamma + He^3 \rightarrow p + d$

| $E_\gamma$ | A | B | C | D | E | $\chi^2$ | Deg of Freedom | $\sigma_T(\mu b)$ |
|---|---|---|---|---|---|---|---|---|
| 250 | .003 | 0.0 | 1. | 2.32 | 3.17 | 7.5 | 2 | $4.09 \pm 0.1$ |
| 300 | 1. | 1.0 | -.21 | .71 | 1.9 | 27. | 2 | $3.29 \pm 0.2$ |
| 350 | 1. | .85 | -.67 | -.37 | -.37 | 2.8 | 3 | $2.12 \pm 0.04$ |
| 400 | 1. | .95 | -.68 | -.52 | -.12 | 2.4 | 3 | $1.39 \pm 0.03$ |
| 450 | 1. | .97 | -.74 | -.76 | -.39 | 5.6 | 3 | $0.84 \pm 0.02$ |
| 500 | 1. | .95 | -.65 | -.65 | -.26 | 0.3 | 3 | $0.47 \pm 0.02$ |
| 550 | 1. | .92 | -.65 | -.97 | -.95 | 0.1 | 1 | $0.27 \pm 0.02$ |

Note that the coefficients A - E have been normalized to A = 1 (except $E_\gamma$ = 250 for which C = 1).

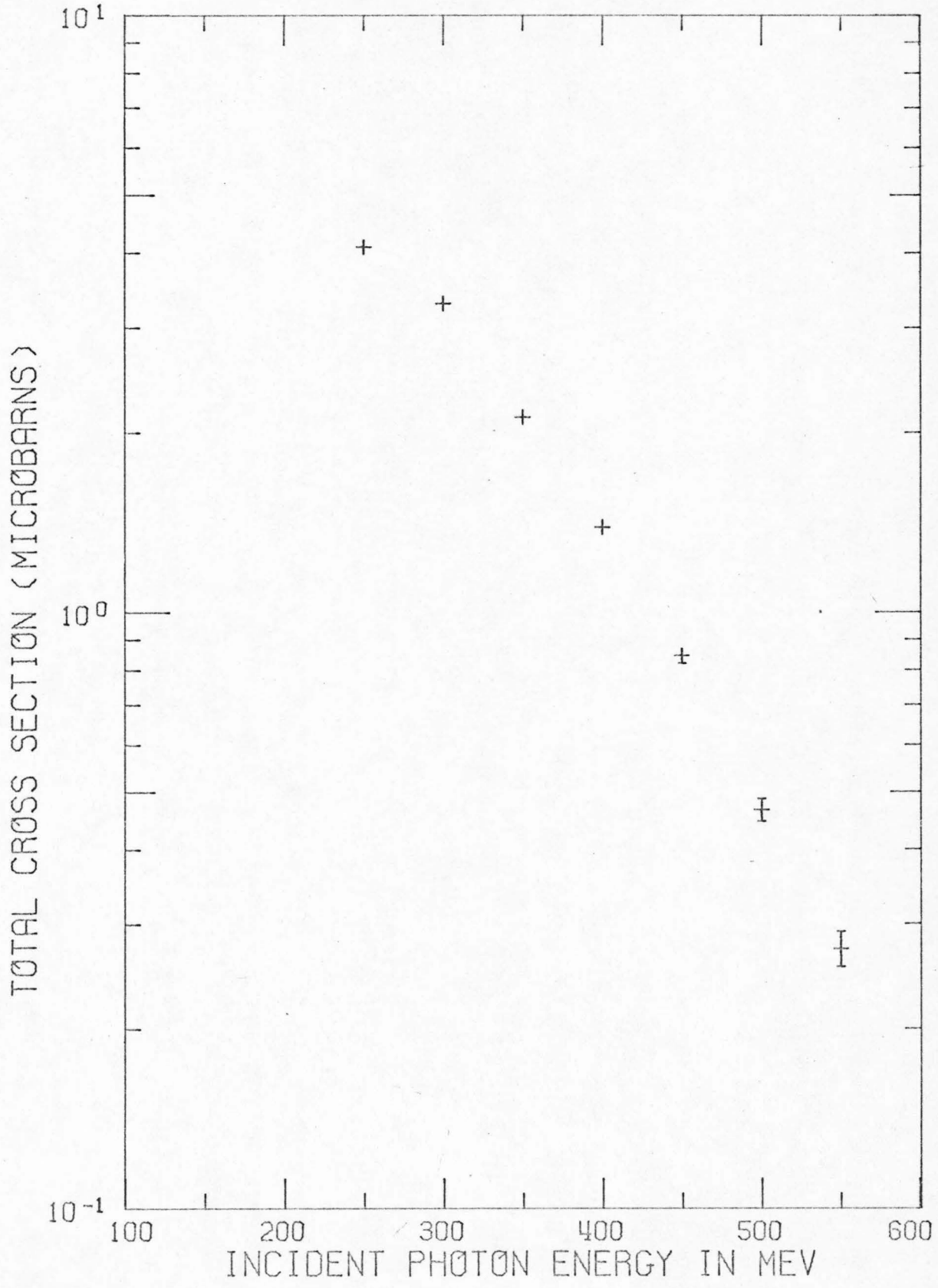


Figure 4.11 $He^3$ Photodisintegration Total Cross-Sections

# V. DISCUSSION

The prominent features of our data on the reaction $\gamma + He^3 \rightarrow p + d$ are:

1. The total cross-section falls with increasing photon energy roughly as $\exp(-E\gamma/100\ MeV)$ above 300 MeV, with an indication of a shoulder near 300 MeV.

2. This energy dependence holds also for the differential cross-sections at angles greater than $60^o$ (c.m. frame).

3. The data at $30^o$ show a rise from 250 to 300 MeV, after which they also fall with energy.

4. The angular distributions show a slight forward dip at 250 MeV which changes to a forward peak at 350 MeV and above.

We first consider the consistency of these trends with other data on the same reaction. Figure 5.1 summarizes the existing total cross-sections for $\gamma + He^3 \rightarrow p + d$, including the present work. Our data have somewhat higher values than might be extrapolated from lower energies. We shall consider the possibility that this is due to $\Delta$ production near photon energies of 300 MeV. Caution is necessary, however, because the total cross-sections are calculated from differential cross-sections observed only at angles between $30^o$ and $150^o$.

The data at $30^o$ offer the best evidence of $\Delta$ production to the extent that they can be regarded with confidence. The $30^o$ data were among the hardest to analyze due to the greater backgrounds and lower chamber efficiencies encountered at smaller angles to the beam. However,

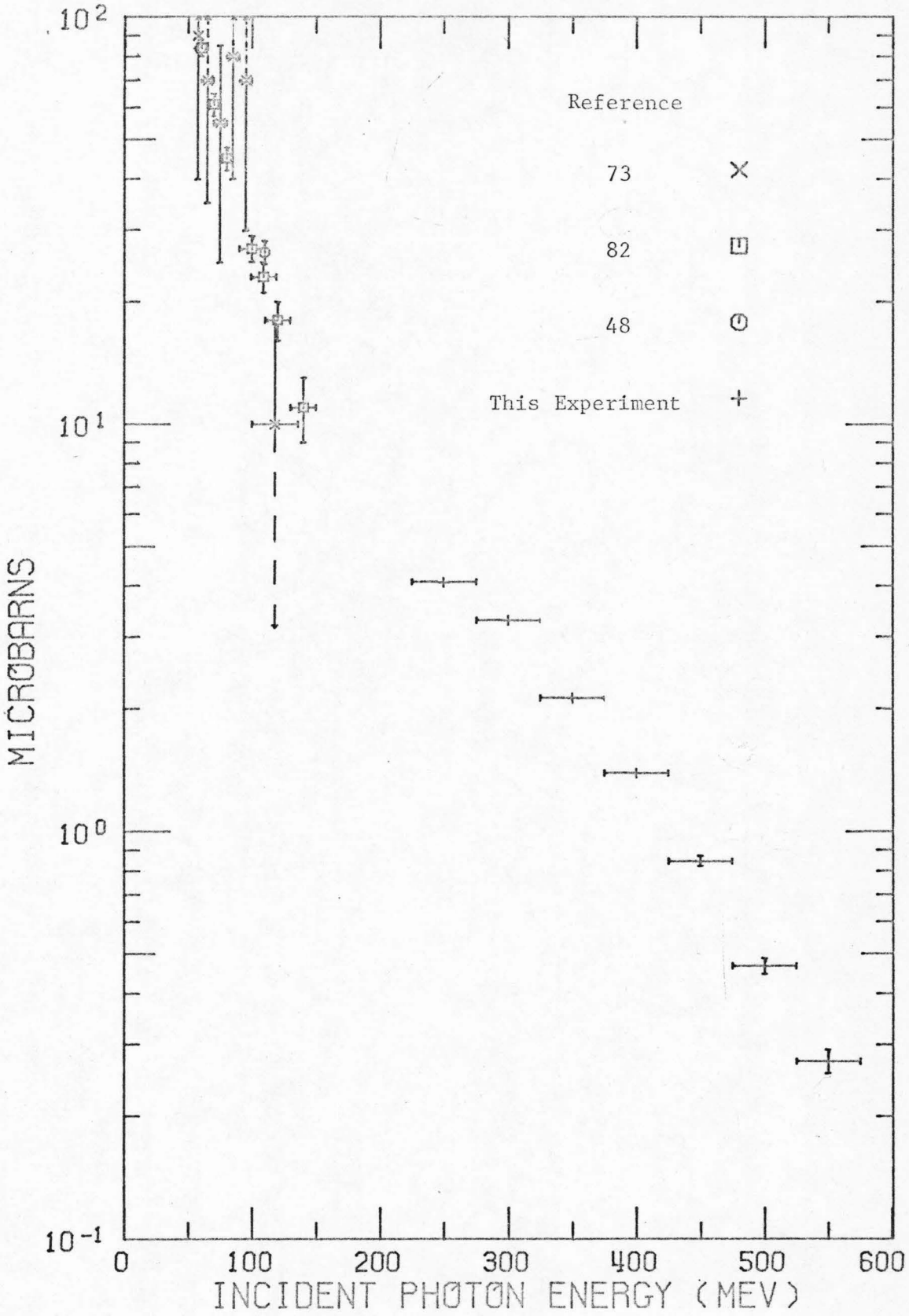


Figure 5.1 Comparison of $He^3$ Photodisintegration Total Cross-Section Data

as seen in Figure 5.2, the data point at 250 MeV is in good agreement with the trend of the data at lower energies. The data at 300 MeV and above indicate the presence of some new mechanism causing higher cross-sections at this angle.

Figures 5.3 through 5.6 give comparisons of data at $60^{\circ}$, $90^{\circ}$, $120^{\circ}$ and $150^{\circ}$, respectively. At $60^{\circ}$ there appears to be a shoulder between 200 and 250 MeV. While this feature may be spurious, the trend of the data above 250 MeV is consistently above an extrapolation from low energies. The data at $90^{\circ}$ and $120^{\circ}$ are in reasonable agreement above and below 250 MeV, and give no particular indication of resonance production. At $150^{\circ}$ the data above 300 MeV are substantially higher than expected from the low energy trend. Unfortunately, the $150^{\circ}$ data from this experiment near 250 MeV are not reliable enough to be reported. There is crude evidence of a large dip near 250 MeV, but we shall not rely on this in further discussion.

In Figure 5.4, it may be noted that our $90^{\circ}$ data are one third lower than those of a Frascati thick plate spark chamber experiment[78] in the same energy range. Both sets of data may be smoothly extrapolated into the cross-sections below 150 MeV. We have searched extensively for possible errors in relative normalization; however, the source of the discrepancy remains an open question.

We may also compare the shapes of our angular distributions with those at lower energies. The forward dip, and peak near $60^{\circ}$ seen in our 250 MeV data (Figure 4.3), are also present at 109 and 140 MeV (Figure 6.3). The change in shape of the angular distributions near

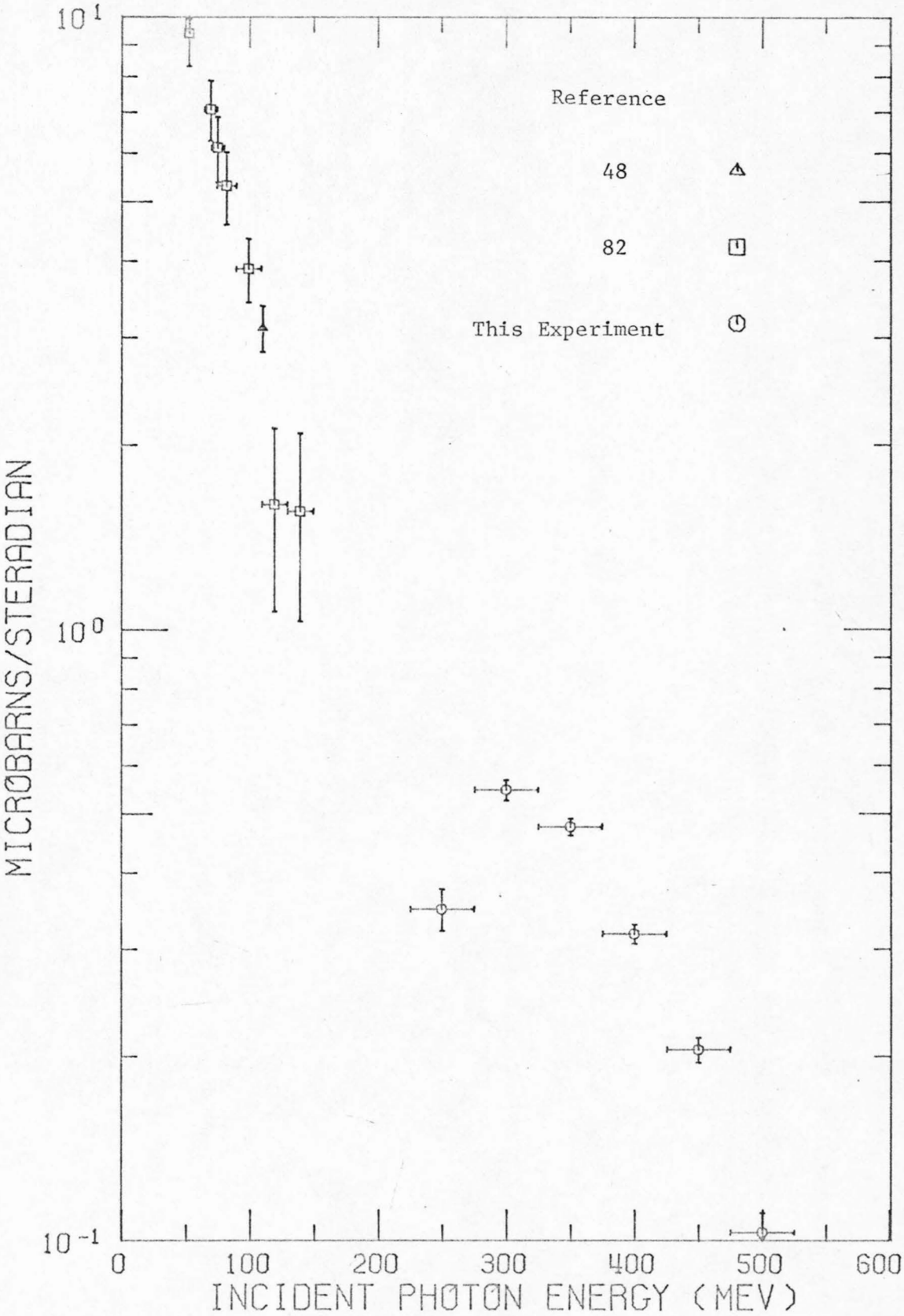


Figure 5.2 Comparison of $He^3$ Photodisintegration Differential Cross-Section Data at $30^{\circ}$(c.m.)

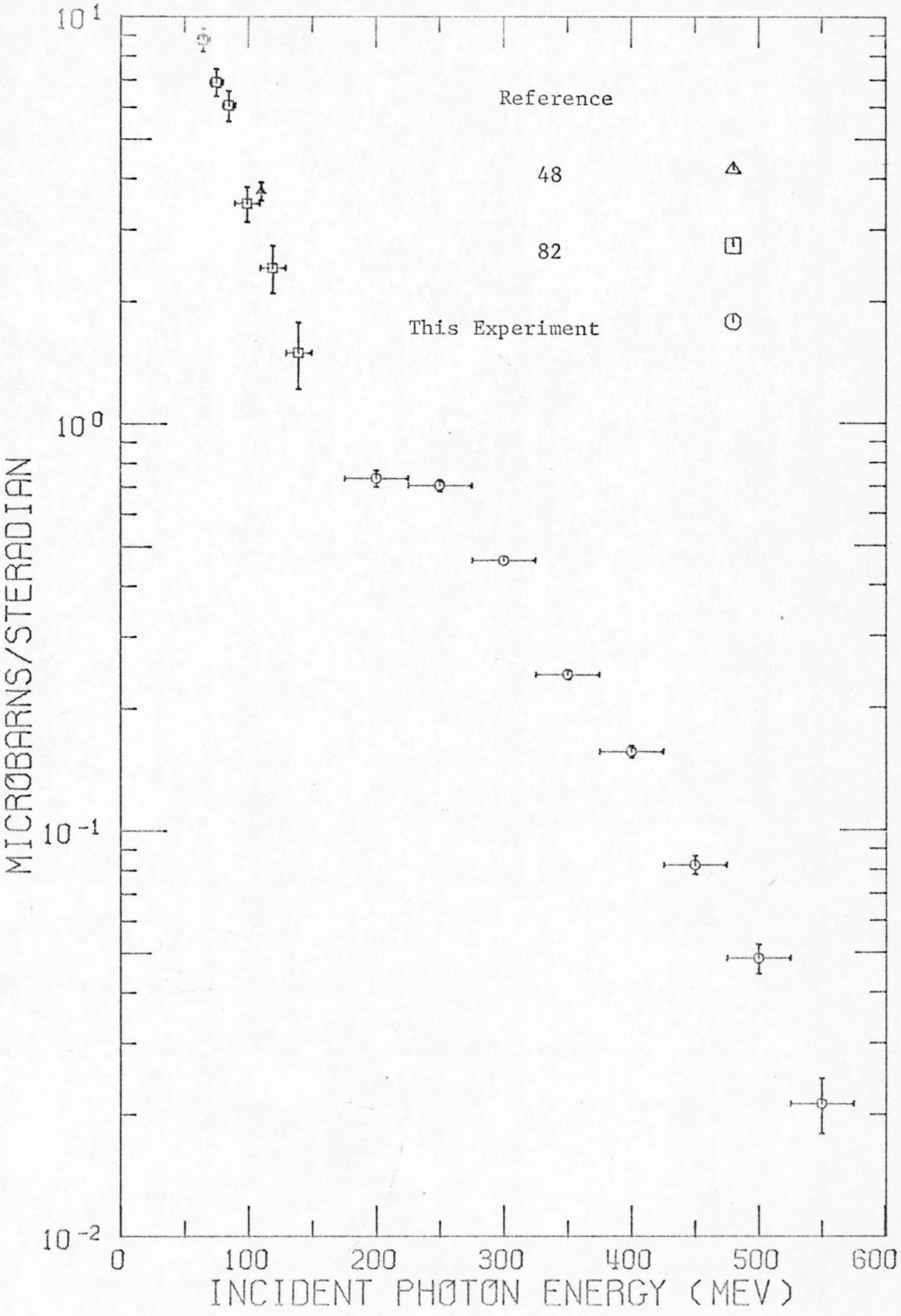


Figure 5.3 Comparison of $He^3$ Photodisintegration Differential Cross-Section Data at $60^o$(c.m.)

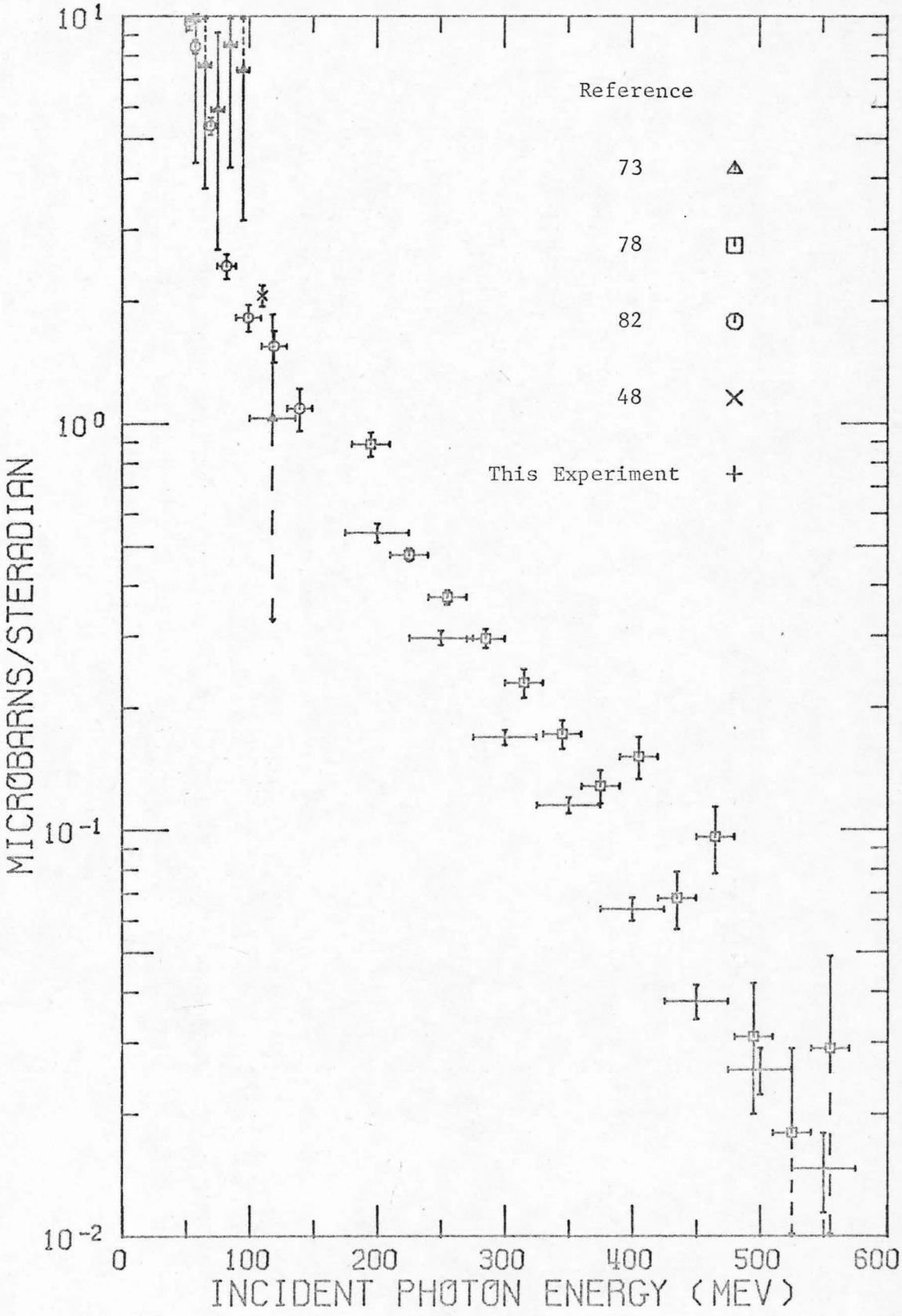


Figure 5.4 Comparison of $He^3$ Photodisintegration Differential Cross-Section Data at $90^{\circ}$(c.m.)

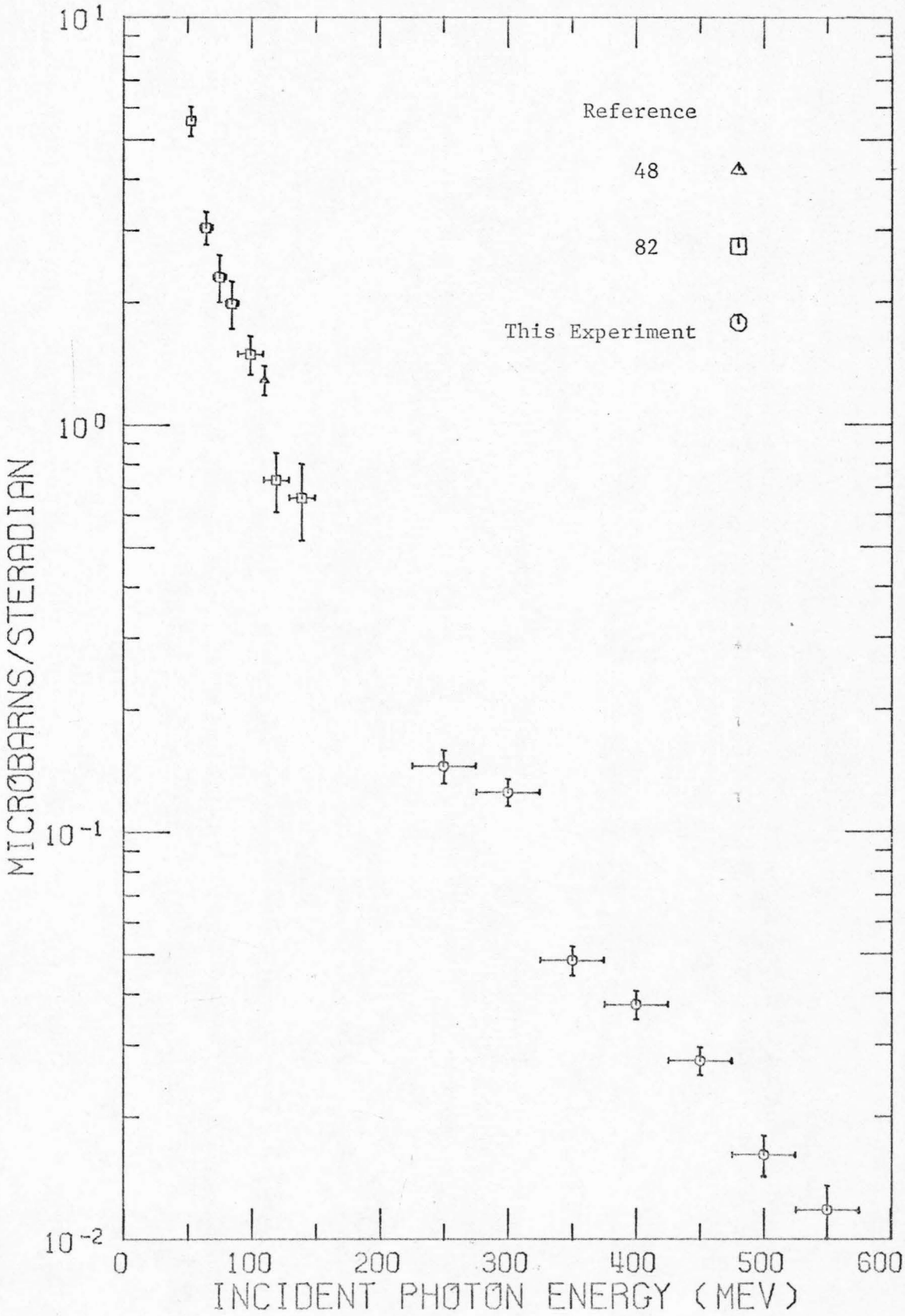


Figure 5.5 Comparison of $He^3$ Photodisintegration Differential Cross-Section Data at $120^{\circ}$ (c.m.)

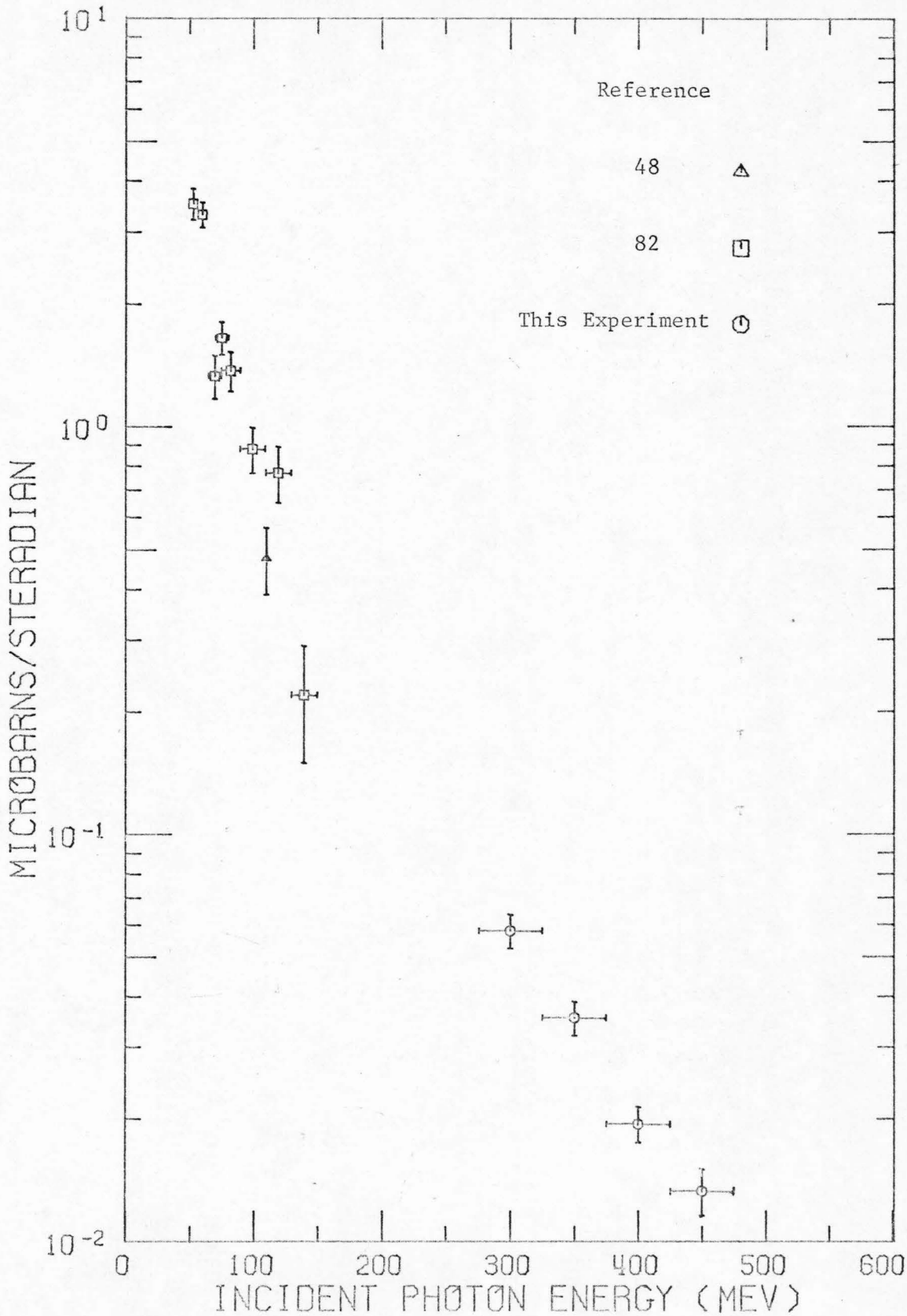


Figure 5.6 Comparison of $He^3$ Photodisintegration Differential Cross-Section Data at $150^{o}$(c.m.)

300 MeV suggests the onset of Δ production. While isospin complications might broaden the region of Δ production (cf. Appendix C), it is unlikely to extend above 400 MeV. There is, however, little change in the angular distribution above 350 MeV. This indicates that the non-resonant part of the cross-section may have altered considerably in the energy region of Δ production. A similar feature is observed in the reaction $\gamma + d \rightarrow n + p$[11].

We now examine the data in more detail for evidence of Δ production, using the models outlined in Appendix C. A sizeable contribution from this process is needed if the test of T-invariance in the reactions $\gamma + He^3 \leftrightarrow p + d$ is to have significance at our energies. Recall, however, that the reciprocity test provides a direct check of T-invariance independent of any particular model; models merely provide us with the size of expected effects.

From the discussion in Appendix C, Δ production might be expected in either of the multipole transitions $M1 \rightarrow {}^4S_{3/2}$ or $M1 \rightarrow {}^2D_{3/2}$, abbreviated $S_3$ and $D_3'$ respectively. S and D label the relative angular momentum of the final state proton and deuteron. The non-resonant background might occur in five amplitudes: $M1 \rightarrow {}^4S_{3/2}$, $E1 \rightarrow {}^2P_{1/2}$ or ${}^2P_{3/2}$, and $E2 \rightarrow {}^2D_{3/2}$ or ${}^2D_{5/2}$, which are abbreviated $S_3$, $P_1$, $P_3$, $D_3$ and $D_5$, respectively. The differential cross-section and polarized photon cross-section asymmetry resulting from these transitions are given in expressions (C.1) and (C.2) of Appendix C. Recall that the differential cross-section is expected to have the form

$$A + B\cos\theta + \sin^2\theta(C + D\cos\theta + E\cos^2\theta).$$

We first briefly discuss the behavior of the non-resonant background, which should be the dominant feature outside the region from 250 to 350 MeV. The pertinent differential cross-section data are summarized in Tables 4.2 and 6.1, while data on the cross-section asymmetry from photodisintegration by polarized photons are discussed in Appendix C. The key features are

1. Coefficients A and B are large above 100 MeV;

2. The cross-section asymmetry is positive but small from 180 to 280 MeV;

3. Coefficients C and E change signs between 250 and 350 MeV.

(1) implies the combinations $P_3$-$P_1$ and $D_5$-$D_3$ are both non-zero. From (2) we conclude $P_3$-$P_1$ is large below 280 MeV. The trend of the asymmetry (2) argues that the sign changes (3) are not due to P-wave effects. Instead, above 350 MeV, $D_5$-$D_3$ is probably dominant, and the negative coefficient E indicates that $D_3$ is the largest amplitude. A significant contribution from the $S_3$ amplitude is not ruled out, but cannot be dominant. Beyond these qualitative features, the large number of possible amplitudes in conjunction with the limited set of data make the assignment of precise numerical values for the amplitudes unadvisable.

Consider now the region between 250 and 350 MeV, where $\Delta$ production may be significant. The transitions $S_3$ and $D_3'$, considered in Appendix C as candidates for $\Delta$ production, lead to isotropic and $2 + 3 \sin^2\theta$ angular distributions, respectively. Neither of these is clearly indicated by the data. The isotropic term is rising from 250 to

350 MeV, but can be attributed to the rise of the $D_3$ transition. The $\sin^2\theta$ term is definitely decreasing, which argues against the importance of the $D_3'$ transition.

However, the observed rise in the $30^o$ cross-sections from 250 to 300 MeV suggests the search for $\Delta$ production should be continued. The $D_3$ transition leads to a $1 + \cos^2\theta$ distribution, if dominant, and interference with $P_3$-$P_1$ will add a $\cos\theta$ term, so that its effect is greatest at small angles. The change in sign of the $\sin^2\theta\cos^2\theta$ term between 300 and 350 MeV (Table 4.2) indicates a large phase change of $D_3$ relative to $D_5$. Thus we conclude that the $D_3$ transition is the most likely candidate for a resonant amplitude.

Recall that $D_3$ abbreviates the transition $E2 \rightarrow {}^2D_{3/2}$. As discussed in Appendix C, the ${}^2D_{3/2}$ final state is possible, and perhaps favored,from intermediate $\Delta$ production. An electric quadrupole photon can initiate the excitation $N \rightarrow \Delta$, but this is much more likely to occur via magnetic dipole radiation[93]. In the photodisintegration of $He^3$, it may be that $\Delta$ production by M1 photons is suppressed, although the mechanism is unclear. Since $\Delta$ production via E2 photons is a small effect[93], this would explain the lack of any prominent resonant behavior in $\gamma + He^3 \rightarrow p + d$ compared to, say, the process $\gamma + d \rightarrow n + p$.

In summary, the data indicate that $\Delta$ production via magnetic dipole photons is unimportant in the photodisintegration of $He^3$. The interesting possibility remains that electric quadrupole photons do initiate $\Delta$ production in an observable amount. The completion of the inverse experiment, $p + d \rightarrow He^3 + \gamma$, will provide a firmer experimental

base for these conclusions. Independent of the details of the amplitudes, the two experiments will provide a test of time reversal invariance in the electromagnetic interaction.

# VI. APPENDICES

## A. Historical Survey of the Reactions $\gamma + He^3 \leftrightarrow p + d$

Helium-3, the nucleus consisting of two protons and a neutron, was first observed in 1934 by the Rutherford group[36]. It was produced by the reaction

$$p + Li^6 \rightarrow He^3 + He^4,$$

and also by

$$d + d \rightarrow He^3 + n.$$

The earliest interest in the photo-disintegration of $He^3$,

$$\gamma + He^3 \rightarrow p + d,$$

centered on the inverse reaction,

$$p + d \rightarrow He^3 + \gamma,$$

which is exothermic by 5.49 MeV. Thus it is a possible step in the transmutation of elements in stars. Indeed, it is the second reaction in the chain which converts hydrogen into helium-4;

1. $p + p \rightarrow d + e^+ + \nu$
2. $p + d \rightarrow He^3 + \gamma$
3. $He^3 + He^3 \rightarrow He^4 + p + p$

"Men have worshipped things more foolish than reactions 1, 2 and 3." - Fred Hoyle[37].

The original work concerning these reactions was theoretical

rather than experimental; Bethe's calculation[38] of the p + d reaction rate is correct to within a factor of 2, in the region of astrophysical interest.

The p + d reaction was first detected in 1939[39]. More recent investigations are reported in references 40 through 49. These experiments show the photons to be emitted predominantly as electric dipole radiation for incident proton energies in the range 1 - 50 MeV.

The p + d experiments inspired various theoretical calculations,[50-64] usually in terms of the photodisintegration of $He^3$ into a proton and deuteron. The calculations are generally restricted to the electric dipole part of the cross-section and to incident photon energies below 40 MeV, corresponding to incident proton energies below 60 MeV in $p + d \rightarrow He^3 + \gamma$. Only Carron[64] considers photon energies above 100 MeV. Various forms are assumed for the $He^3$ wave function and the data are used to determine which is most realistic. The various theories enjoy some success in fitting the energy dependence, but are poor at predicting the shape of the angular distribution, beyond the $\sin^2\theta$ contribution from electric dipole transitions.

A further stimulus to experimental study of $\gamma + He^3 \rightarrow p + d$ as opposed to the inverse reaction was the derivation of certain sum rules for electric dipole radiation by Levinger and Bethe[65,66]. In particular, the bremsstrahlung weighted cross-section should not be sensitive to the details of the nuclear forces:

$$\int \sigma(E) \frac{dE}{E} = \frac{4\pi^2}{3} \alpha \frac{NZ}{A-1} R^2$$

where E = photon energy;

$\sigma$ = total cross-section due to electric dipole radiation;

$\alpha$ = fine structure constant;

A = atomic number; Z = charge; N = A-Z

R = r.m.s. radius of the charge distribution in the nucleus.

If the photons are produced by bremsstrahlung, their spectrum is proportional to 1/E, so that the total scattered particle yield from a bremsstrahlung beam incident on a target is the integral given above. However, both the two-body ($\gamma + He^3 \rightarrow p + d$) and the three-body ($\gamma + He^3 \rightarrow p + p + n$) photodisintegration of $He^3$ must be measured to evaluate the integral.

The first observation of the reaction $\gamma + He^3 \rightarrow p + d$ was in 1958[67], followed by several subsequent experiments[68-82], including observations of the three-body breakup reaction $\gamma + He^3 \rightarrow p + p + n$. Figure 6.1 shows the experimental data for the differential cross-section of $\gamma + He^3 \rightarrow p + d$ at $90^o$ in the center of mass frame as a function of incident photon energy. Figure 6.2 shows the sparser data on the total cross-section. Data from $p + d \rightarrow He^3 + \gamma$ have been converted[83] to that for $\gamma + He^3 \rightarrow p + d$ by the detailed balance relation:

$$\sigma(\gamma + He^3 \rightarrow p + d) = \frac{3}{2} \frac{P_p^2}{P_\gamma^2} \sigma(p + d \rightarrow He^3 + \gamma)$$

evaluated in the center of mass frame. This relation presumes the reactions are invariant under time-reversal.

The angular distributions can be well-fitted at all energies by:

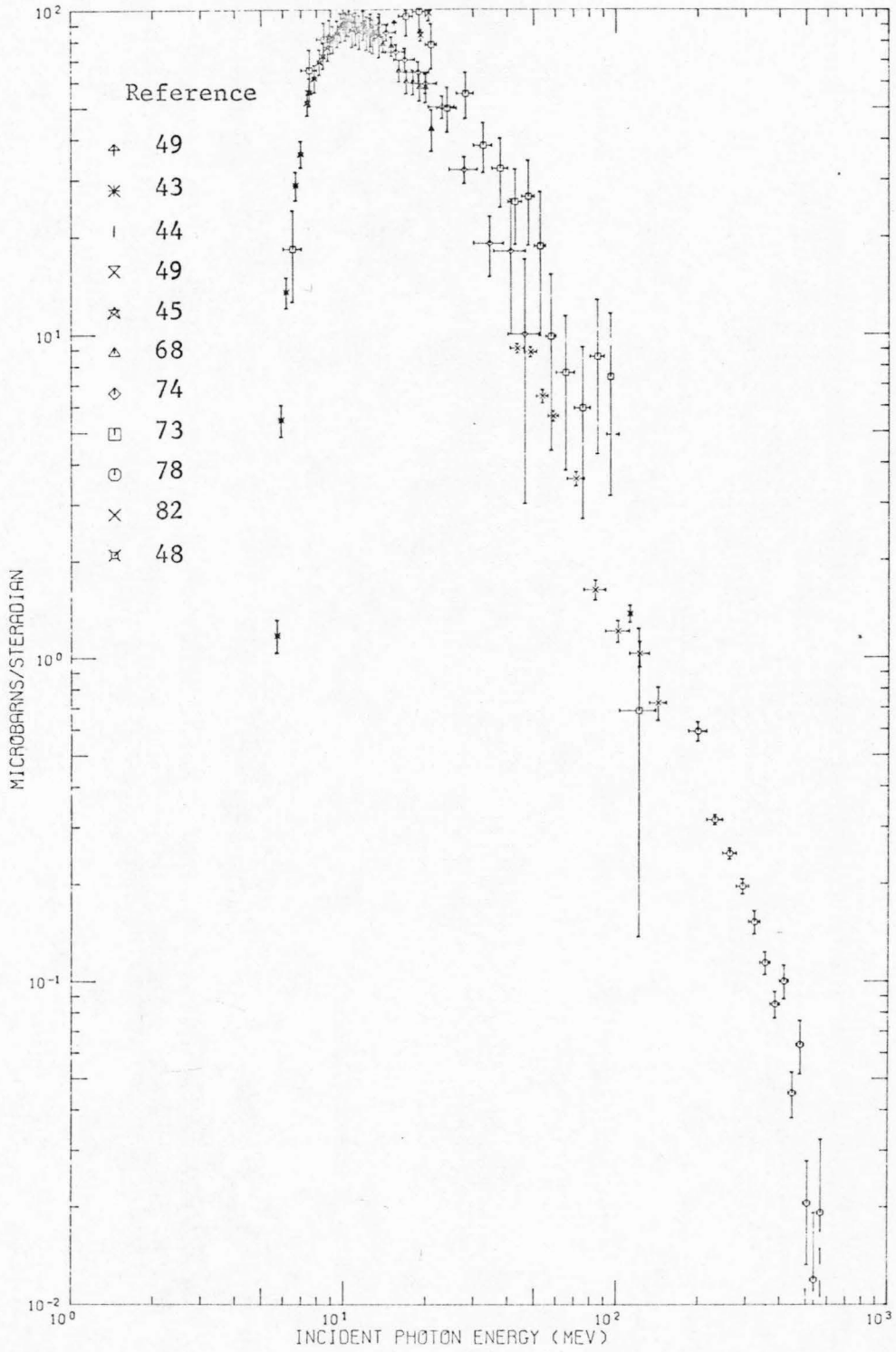


Figure 6.1 Existing Data on $He^3$ Photodisintegration Differential Cross-Sections at $90^o$ (c.m.)

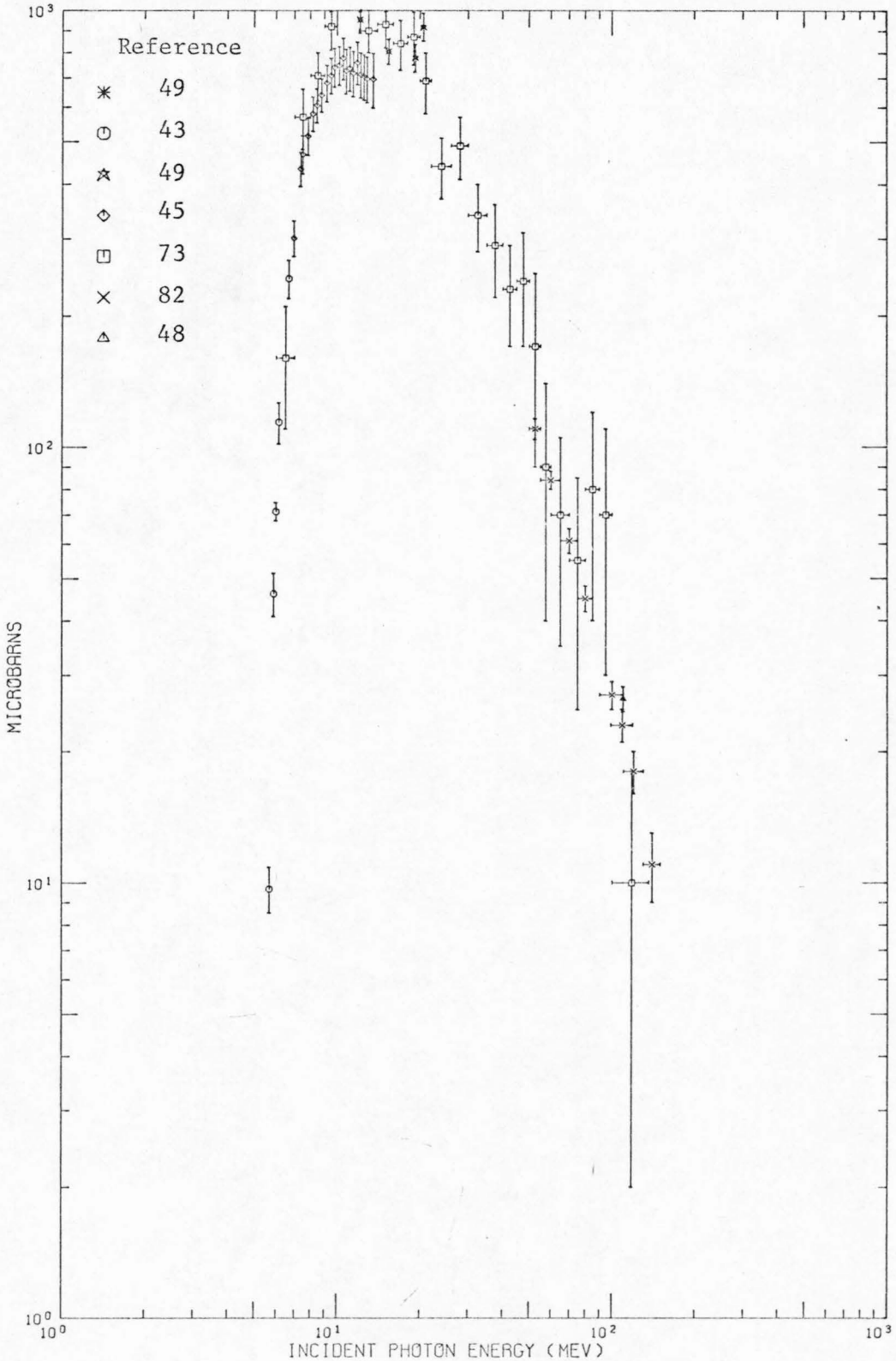


Figure 6.2 Existing Data on $He^3$ Photodisintegration Total Cross-Sections

$$A + B\cos\theta + C\sin^2\theta + E\sin^2\theta\cos\theta + D\sin^2\theta\cos^2\theta.$$

Table 6.1 lists values of the coefficients at representative energies normalized such that C=1. A detailed discussion of possible electromagnetic multipole transitions leading to this angular distribution is given in Appendix C. At low energies, three transitions dominate:

1. Magnetic dipole leading to an S-wave p + d final state. Label this S.
2. Electric dipole leading to a P-wave, labelled P.
3. Electric quadrupole leading to a D-wave, labelled D.

The corresponding angular distribution is

$$S^2 + \sin^2\theta\ (P^2 + \sqrt{2}\ \mathrm{Re}\ P^*D\cos\theta + D\cos^2\theta).$$

The data in Table 6.1 show the dominance of the electric dipole transition for photon energies below 50 MeV. Very near threshold, the magnetic dipole transition has significant relative size, primarily because the electric dipole transition is suppressed by the angular momentum 'barrier'. At photon energies above 50 MeV the electric quadrupole transition is increasingly important, and has the effect of shifting the peak in the differential cross-section away from $90^\circ$ towards smaller angles.

The highest energy at which an angular distribution has been measured is 140 MeV. These data are shown in Figure 6.3, along with a more complete distribution at 109 MeV. The solid curves are fits based on the coefficients in Table 6.1.

The experimental data may also be used to evaluate the Levinger-Bethe sum rule. This rests principally on the work of Fetisov, Grobunov

TABLE 6.1

Angular Distribution Coefficients
for the Reaction $\gamma + He^3 \rightarrow p + d$

The coefficients are normalized such that C=1.

| $E_\gamma$(MeV) | A | B | D | E | Reference |
|---|---|---|---|---|---|
| 5.52 | 0.3 | | | | 44 |
| 5.68 | 0.08 | | | | 43 |
| 6.0 | 0.024 | | | | 43 |
| 6.97 | 0.02 | | 0.13 | | 45 |
| 9.17 | 0.015 | | 0.25 | | 45 |
| 12.11 | 0.013 | | -0.49 | 0.16 | 49 |
| 15.39 | 0.008 | | -0.59 | 0.25 | 49 |
| 19.23 | 0.08 | | -0.27 | 0.39 | 49 |
| 20.60 | 0.11 | | -0.3 | 0.44 | 49 |
| 42.00 | -.01 | | 1.2 | 1.32 | 82 |
| 52.00 | -0.11 | | 1.03 | 1.46 | 82 |
| 75.00 | 0.01 | | 1.94 | 2.62 | 82 |
| 99.00 | -0.08 | | 1.85 | 3.06 | 82 |
| 109.70 | 0.715 | 0.643 | 1.79 | 2.51 | 48 |
| 119.00 | 1.07 | -0.31 | 3.42 | 1.76 | 82 |
| 139.00 | 0.05 | 1.26 | -.58 | 1.88 | 82 |

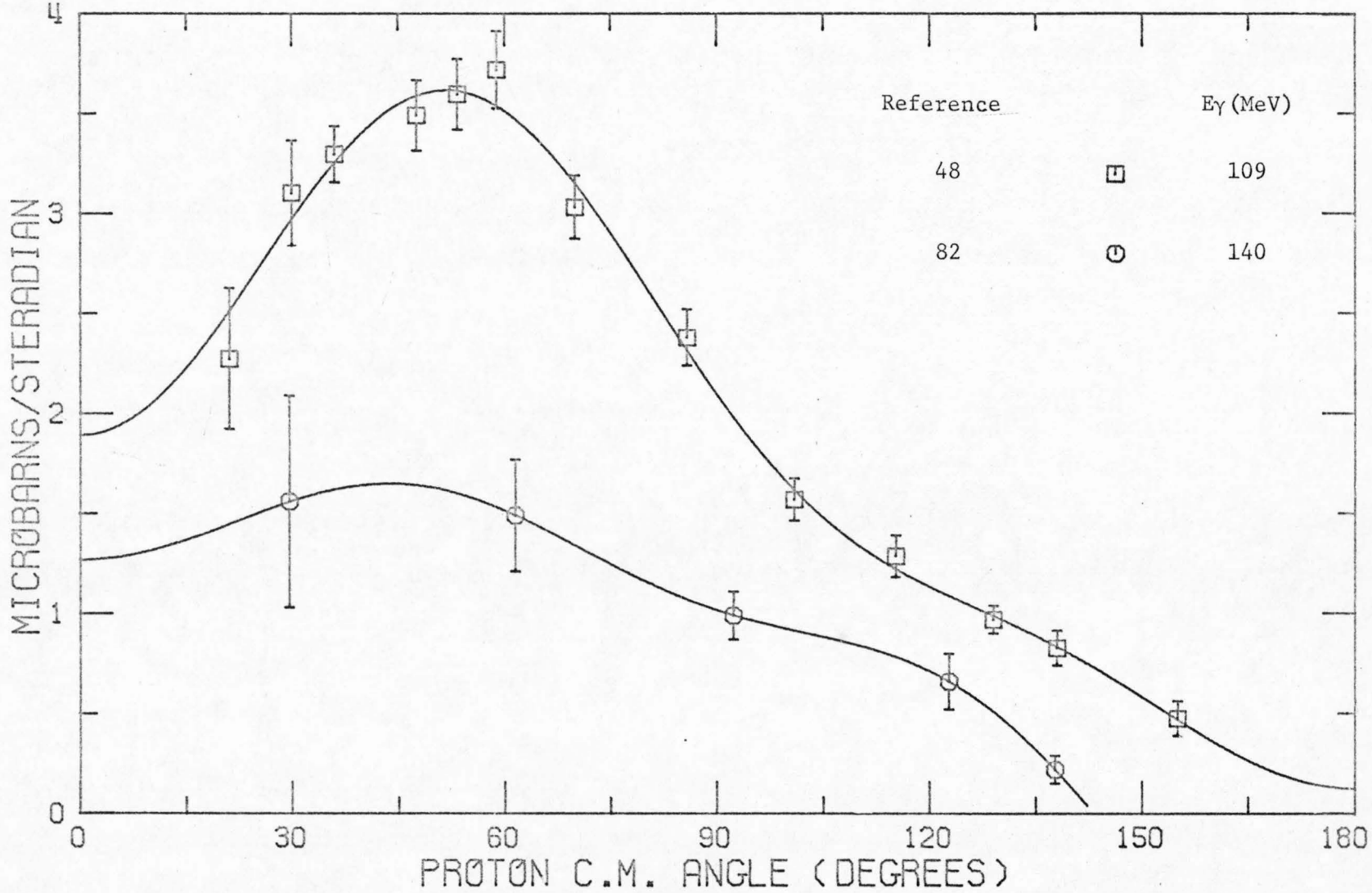


Figure 6.3 $He^3$ Photodisintegration Angular Distributions at 109 and 140 MeV

and Varfolomeev[73]. They found

$$R_{r.m.s.} = 1.81 \pm 0.06 \text{ fermis.}$$

This compares well with the result[84,85]

$$R_{r.m.s.} = 1.88 \pm 0.05 \text{ fermis}$$

obtained from analysis of elastic scattering of electrons with $He^3$.

For more details and for additional information on the three-nucleon problem at low energies, the reader is referred to reviews by Delves and Phillips[86], and by Amado[87].

B. Electrodisintegration of $He^3$

In this Appendix we investigate the possibility of extracting information about photodisintegration of Helium-3, $\gamma + He^3 \to p + d$, from the reaction $e + He^3 \to e' + p + d$. If the latter reaction involves the exchange of a single photon, we may consider the reaction to take place in two steps: $e \to e' + \gamma$ followed by $\gamma + He^3 \to p + d$. The second step is called virtual photodisintegration since the photon is off the mass-shell. Hence an extrapolation to real photodisintegration is necessary.

If the final state electron and proton are detected in the reaction $e + He^3 \to e' + p + d$, we may write[88] (in the one-photon approximation):

$$\frac{d^3\sigma}{dE_{e'}\, d\Omega_{e'}\, d\Omega_p} = \Gamma \frac{d\sigma}{d\Omega_p} ,$$

$\Gamma$ is the virtual photon spectrum factor given by

$$\Gamma = \frac{\alpha}{2\pi^2} \frac{E_{e'}}{E_e} \frac{K}{q^2} \frac{1}{1-\varepsilon} ,$$

where

$$q^2 = 4E_e E_{e'} \sin^2 \frac{\theta_{e'}}{2} = - (\text{4-momentum transfer})^2 ,$$

$$K = \frac{W^2 - M^2_{He^3}}{2M_{He^3}} = \text{real photon energy needed to produce the p + d final state,}$$

$$W = (M^2_{He^3} + 2\nu\, M_{He^3} - q^2)^{\frac{1}{2}} = \text{mass of p + d system,}$$

$$\nu = E_e - E_{e'}$$

$$\varepsilon = 1/(1 + 2(1 + \nu^2/q^2) \tan^2 \frac{\theta_{e'}}{2} = \text{polarization parameter.}$$

The virtual photodisintegration cross-section can be further expressed

$$\frac{d\sigma}{d\Omega_p} = A + \varepsilon B \sin^2\theta_p \cos 2\phi + \varepsilon C + \sqrt{\varepsilon(1+\varepsilon)}\, D \sin\theta_p \cos\phi,$$

where

$\theta_p$ = proton angle in the $\gamma$-$He^3$ c.m. frame.

$\phi$ = angle between the plane $e \to e' + \gamma$ and the plane $\gamma + He^3 \to p + d$.

A, B, C, and D are functions of $q^2$, W and $\theta_p$. The only data for $e + He^3 \to e' + p + d$ are those of Johansson[89], at

$$E_e = 550 \text{ MeV}, \quad E_e' = 443 \text{ MeV}, \quad \text{and} \quad \theta_{e'} = 51.7^\circ.$$

The proton laboratory angles varied from $44^\circ$ to $62^\circ$. The values of the various quantities contributing to the flux factor are:

$\nu = 107$ MeV $\qquad q^2 = 1.85 \times 10$ MeV$^5$

$K = 74$ MeV $\qquad \varepsilon = .667$

$\Gamma = 3.57 \times 10^{-7}$ MeV$^{-1}$

Note that the data were taken at only a single $q^2$, making any extrapolation to $q^2 = 0$ rather uncertain. The effective real photon energy, 74 MeV, is well below the region of $\Delta$ production in $\gamma + He^3 \to p + d$.

To compare these data to those for $\gamma + He^3 \to p + d$ we need to cast the $p + d$ system into the $\gamma - He^3$ c.m. frame. First, note that the lab angle of the photon is

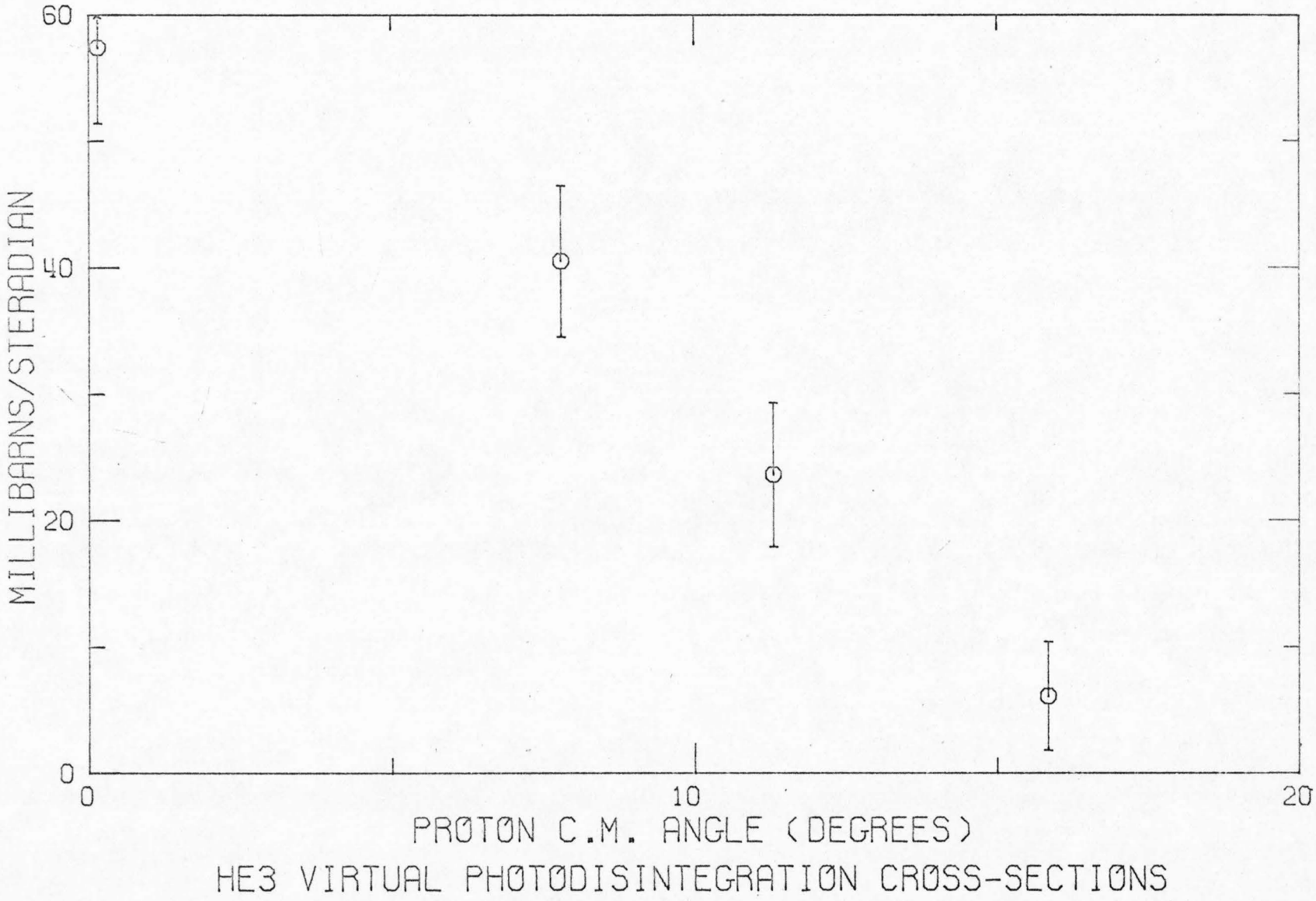
60
40
20
0
MILLIBARNS/STERADIAN
0
10
20
PROTON C.M. ANGLE (DEGREES)
HE3 VIRTUAL PHOTODISINTEGRATION CROSS-SECTIONS

Figure 6.4

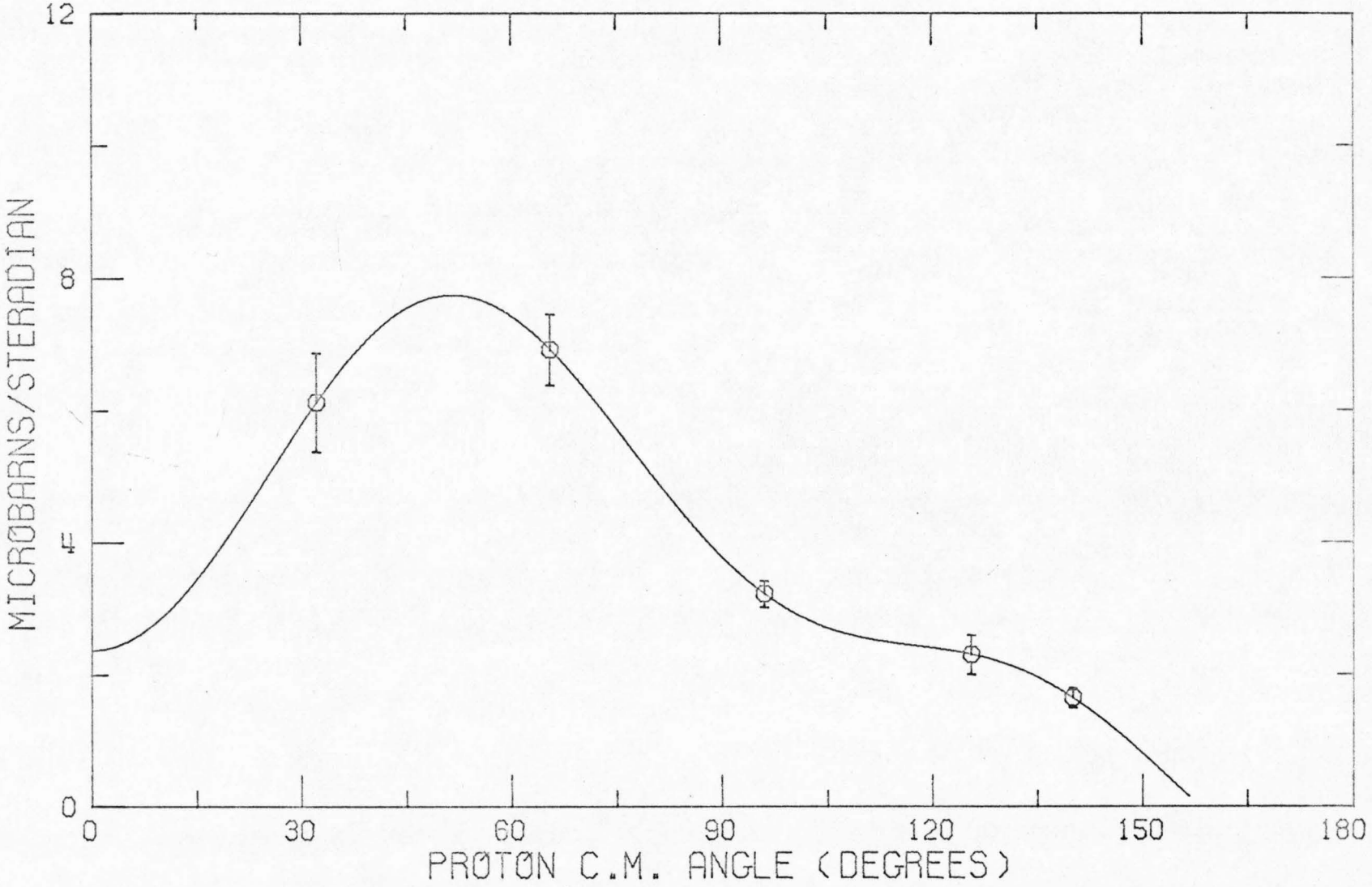


Figure 6.5 $He^3$ Photodisintegration Angular Distribution at 75 MeV

$$\theta_\gamma = \tan^{-1} \frac{E_{e'} \sin\theta_{e'}}{E_e - E_{e'} \cos\theta_{e'}} = 51.6^o.$$

Thus the data for the virtual process $\gamma + He^3 \rightarrow p + d$ all have small angles between the proton and the virtual photon. The solid angle transformation from the laboratory to the center of mass frame can now be calculated. With this, and the factor $\Gamma$ given above, Johansson's data can be expressed as virtual photodisintegration cross-sections. The results are shown in Figure 6.4.

They can be compared with the real photodisintegration data at 75 MeV photon energy of O'Fallon et al[82]. We consider this energy because the p + d final state produced by $\gamma + He^3 \rightarrow p + d$ has the same invariant mass as that of the p + d state in $e + He^3 \rightarrow e' + p + d$. The data are shown in Figure 6.5, with a fit based on the parametrization given in Appendix A. It is very striking that the real photodisintegration cross-sections are about four orders of magnitude smaller than those due to virtual photodisintegration, and that the former has a forward dip while the latter is strongly peaked at small angles.

The problem now is to explain the large experimental difference between the two conceptually similar photodisintegration reactions. The following argument is due to R. P. Feynman (private communication). The forward peak in the virtual photodisintegration cross-section suggests that the dominant mechanism is that a proton inside the $He^3$ absorbs the virtual photon and recoils along the direction of the photon. If energy and momentum are conserved, there need not be any final state interaction. The cross-section for the electrodisintegration of $He^3$

will then be very near twice that of the elastic scattering of electrons on protons. Since it is not possible for a proton to absorb a real photon and conserve energy and momentum, this process will not contribute to the disintegration of $He^3$ by real photons, and the cross-section will be much lower.

A refinement of the argument recognizes that the proton inside the $He^3$ need not be on the mass shell, but may have fermi momentum p. The distribution of possible fermi momenta is centered at 0 and has a width of about 100 MeV/C. Then if the photon has energy $\nu$ and momentum Q, conservation of energy and momentum requires

$$2m\nu - q^2 = p(p + 2\,Q).$$

For Johansson's experiment, this implies protons with 20 MeV/c fermi momentum parallel to the photon's direction can absorb the photon. However, for real photons of 74 MeV, the necessary momentum for the proton is 300 MeV/C. It is very unlikely that a proton in $He^3$ has this high a fermi momentum in the direction of the photon. Hence the conclusion is the same as before.

As the electrodisintegration process can be well approximated by the elastic scattering of a single proton, this can be used to calculate the cross-section. See, for example, Gibson and West[90], who obtain a good fit. Conversely, we see that it will be difficult to calculate cross-sections for the photodisintegration of $He^3$ at energies well above threshold.

C. Electromagnetic Multipole Structure of $\gamma + He^3 \rightarrow p + d$

In this Appendix, the angular distribution for the reaction $\gamma + He^3 \rightarrow p + d$ is parametrized according to various electromagnetic multipoles [91]. For this purpose, we suppose that the wave function of $He^3$ is a $^2S_{1/2}$ state. The effect of the roughly five per cent admixture of a $^4D_{1/2}$ state has been considered by Bailey et al[58] and by Bock [80]. The effect is small and does not introduce any new angular functions; we therefore neglect it.

A list of all possible electric dipole, E1, magnetic dipole, M1, and electric quadrupole, E2, transitions is given below. The p + d final states are labelled by total angular momentum, total spin, and relative orbital angular momentum.

| E1 $\rightarrow$ | M $\rightarrow$ | E2 $\rightarrow$ |
|---|---|---|
| $^2P_{1/2} = P_1$ | $^2S_{1/2}$ | $^4S_{3/2}$ |
| $^2P_{3/2} = P_3$ | $^4S_{3/2} = S_3$ | $^2D_{3/2} = D_3$ |
| $^4P_{1/2}$ | $^2D_{3/2} = D_3'$ | $^2D_{5/2} = D_5$ |
| $^4P_{3/2}$ | $^4D_{1/2}$ | $^4D_{3/2}$ |
| | $^4D_{3/2}$ | $^4D_{5/2}$ |

To determine which transitions are likely to be most important, we first consider scattering near threshold. The $\sin^2\theta$ behavior observed there indicates the dominance of E1 transitions. At low energies, E1 transitions affect the orbital angular momentum but not the spin. The important E1 transitions therefore lead to either the $^2P_{1/2}$ or the $^2P_{3/2}$

final state, abbreviated $P_1$ and $P_3$ respectively. Indeed, we expect $P_1 = P_3$ near threshold.

The presence of a small isotropic component at low energies is very likely due to the magnetic dipole transition to the $^4S_{3/2}$ final state, abbreviated $S_3$. Other magnetic transitions are suppressed by the angular momentum barrier, or the requirement that M1 transitions couple primarily to spin.

At energies above about 25 MeV, the angular distribution shows peaking at angles rather less than $90^o$. This can be accounted for by the E2 transitions leading to $^2D_{3/2}$ and $^2D_{5/2}$ final states, abbreviated $D_3$ and $D_5$ respectively. These two are favored over the other possibilities as the spin wave function is unaltered by these transitions. At low energies, we expect $D_3 = D_5$, again because electric radiation couples only to orbital angular momentum in this limit.

We consider the five independent transitions $P_1$, $P_3$, $S_3$, $D_3$ and $D_5$ sufficient to parametrize the non-resonant part of $\gamma + He^3 \rightarrow p + d$ even up to energies of 500 MeV. An evaluation of the angular distribution corresponding to these transitions leads to the form

$$A + B\cos\theta + \sin^2\theta\ (C + D\cos\theta + E\cos^2\theta),$$

where

$$A = S_3^2 + (P_3 - P_1)^2 + 2(D_5 - D_3)^2$$

$$B + 2\sqrt{2}\ \mathrm{Re}(P_3 - P_1)^*(D_5 - D_3)$$

$$C = 3/2\ P_3^2 + 3\mathrm{Re}\ P_3^* P_1 - (D_5 - D_3)^2$$

$$D = 5\sqrt{2}\ \mathrm{Re}\ P_1^* D_5 + 2\sqrt{2}\ \mathrm{Re} P_3^*(2D_5 + 3D_2)$$

$$E = 5(D_5 + 2D_3)^2 - 20D_3^2.$$

All squared quantities are to be taken as absolute squares. In the low energy limit, we may take

$$P_1 = P_3 = \sqrt{2}/3P;\ D_3 = D_5 = D/5 \text{ and } S_3 = S,$$

then $A = S^2$

$B = 0$

$C = P^2$

$D = \sqrt{2}\ P^*D$

$E = D^2$

We now consider which multipole amplitudes might contain a $\Delta(1236)$ in an intermediate state. We suppose that one of the nucleons in $He^3$ is excited into a $\Delta$ by the absorption of a photon. The $\Delta$ coexists for a short time with the other two nucleons before it decays by the emission of a pion, which must be absorbed by one of the non-resonant nucleons as part of the final-state interaction yielding a proton and a deuteron.

Isospin conservation in the final state interaction forbids the two non-resonant nucleons from being a deuteron in the intermediate state. A diagram for this process is

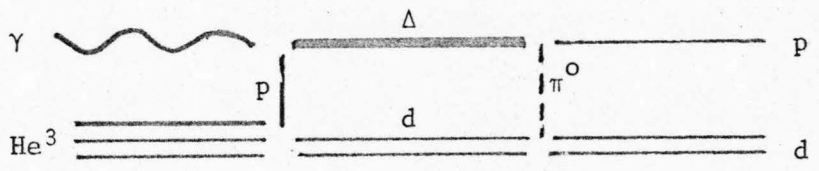


The p + d final state has isospin 1/2, while the $\Delta$ + d state has isospin 3/2. To conserve isospin, the two non-resonant nucleons must be in an isospin 1 combination. There is no such state which is bound. Phase

shift analyses[92] show the $^1S_0$ to be the strongest unbound state in nucleon-nucleon scattering between threshold and 150 MeV. A possible diagram for photodisintegration of $He^3$ including a $^1S_0$ is

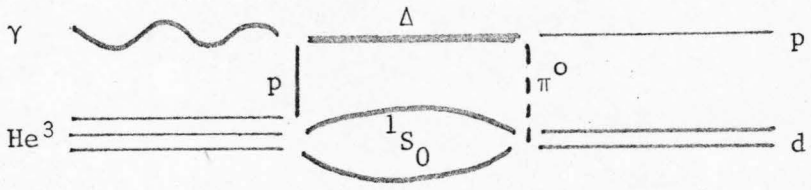


If all three baryons were at rest in the intermediate state, the effect of the Δ would be centered at incident photon energies about 320 MeV. Since all three particles must have positive kinetic energies relative to one another, any 'peak' in the cross-section due to a Δ will be smeared towards higher energies. Based on the $^1S_0$ phase shifts,[92] the smearing might well be on the order of 100 MeV. The effect of the Δ in $\gamma + He^3 \rightarrow p + d$ will not be nearly as dramatic as in $\gamma + d \rightarrow p + n$.

In order to assign specific multipole transitions to the above diagram, further assumptions must be made. First, suppose the Δ has zero orbital angular momentum relative to the $^1S_0$. Then the p + d final state must have total angular momentum 3/2 and positive parity. There are three such states: $^4S_{3/2}$, $^2D_{3/2}$, and $^4D_{3/2}$. Referring to the list of transitions earlier in this Appendix, all three final states can be reached by either a magnetic dipole or an electric quadrupole transition. From data on pion photoproduction, it is known[93] that magnetic dipole radiation dominates the photonuclear production of a Δ. In the present case, the multipolarity of the radiation is with respect to the entire $He^3$ nucleus and not its constituent nucleons. We shall assume that the

magnetic dipole radiation relative to the nucleon which is excited into a $\Delta$ is also magnetic dipole radiation relative to $He^3$. Qualitatively, this can be justified by the model that the $He^3$ consists of two spectator nucleons in a $^1S_0$ state which has zero relative orbital angular momentum with respect to the third nucleon. This nucleon absorbs a magnetic dipole photon and becomes a $\Delta$, which will also have zero orbital angular momentum relative to the $^1S_0$ spectator.

In summary, a model based on one excited nucleon and a $^1S_0$ spectator two nucleon system permits $\Delta$ production in three amplitudes: $M1 \rightarrow {}^4S_{3/2}$, $^2D_{3/2}$, $^4D_{3/2}$. Near threshold, the $^4S_{3/2}$ final state, previously abbreviated $S_3$, is favored by its low angular momentum, but this need not be so for photon energies of 300 MeV.

By considering two-nucleon correlations inside the $He^3$, we obtain an indication that the $M1 \rightarrow {}^2D_{3/2}$ transition, abbreviated $D_3'$, should dominate $\Delta$ production. The strongest two-nucleon interaction is in a $^3S_1$ state[92], having roughly twice the probability of a $^1S_0$ interaction at low energies. It is therefore reasonable to assume that the nucleon which absorbs the photon is in a $^3S_1$ relative to one of the other nucleons inside the $He^3$. We suppose this correlation lasts as long as the photodisintegration process, and can thereby affect the angular distribution of the final state particles. In particular, if the photon excites the nucleon into a $\Delta$, which then decays via pion emission, the pion is more likely to be absorbed by the partner nucleon of the $^3S_1$ state than by the third nucleon. $\Delta$ production by magnetic dipole photons can only result in a $^1D_2$ state of the two-nucleons after the pion has

been absorbed. To obtain a proton and a deuteron in the final state, the third nucleon must combine with a member of the $^1D_2$ to form a deuteron. A possible diagram for this is

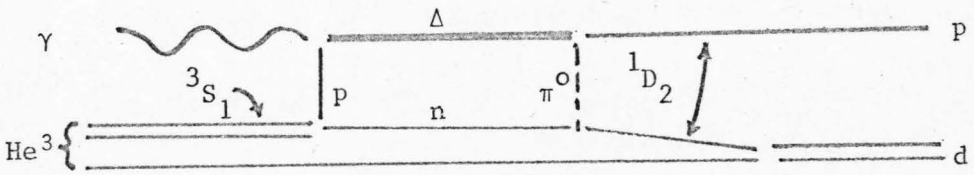


The third nucleon must have been in an S-wave relative to the other two, assuming the $He^3$ wave function to be $^2S_{1/2}$. Thus the final p + d states which can be reached are the $^2D_{3/2}$ and the $^2D_{5/2}$. Only the $^2D_{3/2}$ can be obtained from a magnetic dipole transition of the $He^3$.

A similar argument shows that Δ production is not possibe by a photon hitting one of two nucleons with a $^1S_0$ correlation. The consideration of two-nucleon correlations in the photodisintegration of heavy nuclei has been called the 'quasi-deuteron' model.[66,94] Experimentally observed[73] angular correlations between final state protons and neutrons in the reaction $\gamma + He^3 \rightarrow p + p + n$ are evidence of two-nucleon correlations inside the $He^3$. This model could also be applied to the discussion of non-resonant amplitudes given in the first part of this Appendix. However, it places no further restrictions on the possible amplitudes already given.

We may now give a form for the angular distribution of $\gamma + He^3 \rightarrow p + d$ including the amplitude $D_3'$ for Δ production. Recall that the amplitude $S_3$ is also a candidate for Δ production. Again the angular distribution has the form

$$A + B\cos\theta + \sin^2\theta\,(C + D\cos\theta + E\cos^2\theta),$$

where now

$$A = S_3^2 + (P_3 - P_1)^2 + 2(D_5 - D_3 - D_3')^2$$

$$B = 2\sqrt{2}\ \mathrm{Re}\ (P_3 - P_1)^*(D_5 - D_3 - D_3')$$

$$C = 3/2\ P_3^2 + 3\mathrm{Re}P_3^*P_1 - 4(D_5 - D_3)^2 + 3(D_5 - D_3 + D_3')^2 \qquad (C.1)$$

$$D = 5\sqrt{2}\ \mathrm{Re}\ P_1^*D_5 + 2\sqrt{2}\ \mathrm{Re}\ P_3^*(2D_5 + 3D_3)$$

$$E = 5(D_5 + 2D_3)^2 - 20D_3^2$$

Note that the amplitude $D_3'$ interferes with the amplitudes $P_1$, $P_3$, $D_3$ and $D_5$, which are observed to be large at low energies. If $D_3'$ contains a T-violating phase, it could cause a large difference between the angular shapes of the cross-sections of the reaction $\gamma + He^3 \leftrightarrow p + d$.

In the remainder of this Appendix, we give expressions for the angular distributions due to photodisintegration of $He^3$ by polarized photons. We consider photons polarized transversely parallel and perpendicular to the scattering plane leading to cross-sections abbreviated $\sigma_{\parallel}$ and $\sigma_{\perp}$ respectively. The cross-section due to unpolarized photons, given earlier in this Appendix, is abbreviated $\sigma_T$. Let $A_T$, $B_T$, etc., label the coefficients of the angular functions given previously. Then $\sigma_{\perp}$ and $\sigma_{\parallel}$ have the same functional form as $\sigma_T$ with coefficients

| | $\sigma_{\perp}$ | $\sigma_{\parallel}$ |
|---|---|---|
| A | $A_T$ | $A_T$ |
| B | $B_T$ | $B_T$ |
| C | $-2(D_5 - D_3 - D_3')^2 + 8D_3'^2$ | $3P_3^2 + 6\mathrm{Re}P_3^*P_1 + 8\mathrm{Re}D_3'(D_5-D_3)^*$ |
| D | 0 | $2D_T$ |
| E | 0 | $2E_T$ |

Note that $\sigma_{\perp} + \sigma_{\parallel} = 2\ \sigma_T$.

The asymmetry in the scatter of polarized photons is defined as $(\sigma_{\parallel} - \sigma_{\perp})/(\sigma_{\parallel} + \sigma_{\perp})$. At $90^{\circ}$, this is

$$\frac{3P_3^2 + 6\mathrm{Re}P_3^*P_1 + 2(D_5 - D_3 + D_3')^2 - 8D_3'^2}{2S_3^2 + 3P_3^2 + 6\mathrm{Re}P_3^*P_1 + 2(P_3 - P_1)^2 + 2(D_5 - D_3 + D_3')^2 + 8D_3'^2} \qquad (C.2)$$

In the limit of low energies as described earlier, this becomes

$$\frac{P^2}{S^2 + P^2}\ .$$

The asymmetry at $90^{\circ}$ (c.m.) has been measured[95] for photon energies between 180 and 280 MeV. The values decrease linearly from 0.4 at 180 MeV to 0.3 at 280 MeV.

If the low energy approximation holds at these energies, the $S^2$ term must be twice the $P^2$, which is not in agreement with the cross-section data presented in this thesis.

The more detailed expression for the asymmetry shows that the size of

$$S_3^2 + (P_3 - P_1)^2 + 4D_3'^2$$

must be roughly twice that of

$$3P_3^2 + 6\mathrm{Re}P_3^*P_1 + 2(D_5 - D_3 + D_3')^2$$

Further, $D_3'$ must be small since the asymmetry is positive. These conclusions hold at 180 MeV, well below $\Delta$ production energies, as well as at 280 MeV, where this process might contribute substantially.

D. The Photon Beam Spectrum

The energy of the circulated electrons was held at a nominal value of 700 MeV for the entire experiment. The fluctuations about this value were short-lived compared to an average run, and of order of 0.5%. They have been ignored. The standard calibration of the beam energy by Thiessen[96] gives the true energy as 1.021 $\pm$ .003 of the nominal value, or 714 MeV for the present case. Recent work of McNeely and Yellin[97] confirms Thiessen's calibration.

The differential energy spectrum of photons in the beam is given by

$$n(K)dK = \frac{W}{E_o} \frac{B(K,E_o)}{K} dK$$

where $K$ = photon energy,

$E_o$ = energy of the circulating electron beam (714 MeV for this experiment),

and $W$ = total energy in the beam.

The function $B(K,E_o)$ was calculated using a computer program written by Wolverton[98]. It is approximately equal to unity for K less than $E_o$, and is normalized such that

$$\int_o^{E_o} B(K, E_o)\, dK = E_o$$

Wolverton estimates a systematic uncertainty of 2%. W is measured by the beam monitors as discussed in Appendix E. The possible systematic error in W is 3%, while its statistical uncertainty is 1%. Thus the beam spectrum is known to a statistical accuracy of 1% with a maximum

systematic error of about 5%. This systematic error would influence the normalization but not the shape of the differential cross-sections measured in this experiment.

Because the beam diameter is large at the target, the intensity variation across the beam should be taken into account in the Monte Carlo detection efficiency calculation. The beam profile has been measured by Groom[99] by observing the grain density in photographic plates exposed in the beam. (A thin copper sheet was used to convert the high energy photons into ones of wave lengths, more suitable for photography.) Following Groom, I set the intensity to

$$I(r) \sim \cos^2\left(\frac{r}{3}\right) \qquad 0 \leq r < 1.5$$

where r - distance from the beam axis in inches.

(Note that the number of photons at a radius r is given by $n(r)\,dr \sim r\,I(r)\,dr$.) This intensity function can also be measured using the observed distribution of event vertices in this experiment. Figure 6.6 shows the result of a typical run to be in reasonable agreement with the above fit.

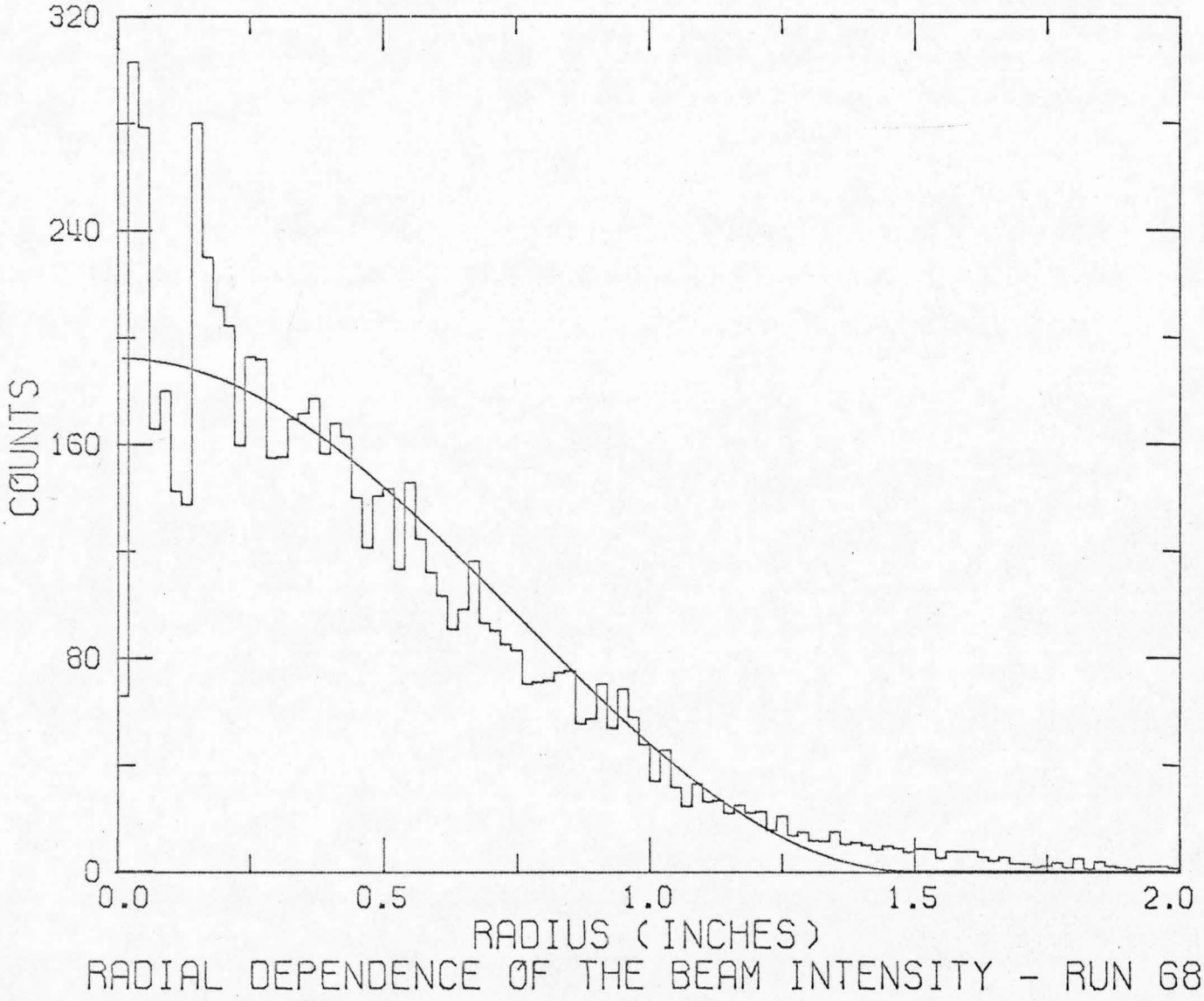
320
240
160
80
0
COUNTS
0.0
0.5
1.0
1.5
2.0
RADIUS (INCHES)
RADIAL DEPENDENCE OF THE BEAM INTENSITY - RUN 68

Figure 6.6

E. Beam Monitoring

The primary beam monitor was a thick plate ion chamber located about thirty feet downstream of the $He^3$ target as shown in Figure 2.1. As secondary monitors, there were two thin plate ion chambers upstream of the sweep magnet. In addition, the circulating electron beam of the synchrotron was monitored with a probe tuned to forty megahertz (the frequency of the R.F. accelerating field).

The charge collected by the ion chambers was measured with Littauer-type[100] current integrators. The integrators were calibrated daily against a precision current source, accurate to 0.25%. The results of the integrator calibration varied linearly with time. When the variation reached about 0.5%, the integrators were readjusted.

Two sources of error rendered the integrators less reliable during the first half of the experiment. A leakage current from a faulty ion chamber high voltage power supply caused the integrators to read too little by an unknown amount of the order of 1%. The second error was caused by the relays which turned the integrators off during the dead-time of the experiment associated with firing the spark chambers. This did not affect the thick ion chamber appreciably but did make the thin ion chambers unreliable. However, the thin chambers were used mainly during the calibration of the thick ion chamber as described below. During this calibration, the relays were disconnected as the spark chambers were not fired then. The result of the ion chamber calibration from the second half of the experiment was used for the whole experiment.

The measurement of the charge collected by the ion chambers must now be related to the energy of the beam. For this, the output of the thick ion chamber was compared daily with that of two Wilson-type[101] quantameters. The quantameter constant is calculated[102] to be

$$13.1\ (\pm 3\%) \times 10^{18}\ T/P\ \text{MeV/coulomb}$$

where T = temperature in $^{o}K$

and P - pressure in mmHg

for a gas mixture of 95% argon and 5% $CO_2$. The 3% uncertainty constitutes the systematic error of the quantameter calibration. This result was confirmed by a calibration of one of the quantameters against a Faraday cup at the Stanford Mark II linear accelerator[102]. Measurements taken during the experiment showed that all three of the ion chamber and quantameters were leaking slowly. The ion chamber was the worst at 1% per month.

The quantameters were mounted on rolling platforms on the lead wall just upstream of the $He^3$ target (Figure 2.1). When one was in the beam, the thick ion chamber was the shadow. Hence the calibration was done using the 40 mc probe and the two thin ion chambers as intermediate standards. This resulted in six ways of calibrating the thick ion chamber against the two quantameters. The average of these six methods was used. The variance of the six calibrations about the average was roughly 1% which I take as the statistical error of the final calibration. The systematic error, as noted above, is about 3%.

As a sidelight, we can compare the two quantameters, the so-called 'south' and 'west' quantameters. The ratio of the south quanta-

meter output to that of the west quantameter was

$$0.867 \pm .01$$

while the ratio of their gas densities was

$$0.884 \pm .004.$$

Thus the south quantameter constant was about 1.5% less than that of the west quantameter. I feel that the west quantameter is nearer the truth as its gas was above atmospheric pressure while the south quantameter gas was below (although both were apparently leaking!).

We now consider the question of the relation between the beam at the $He^3$ target and the beam at the thick ion chamber. The beam was always well centered on the $He^3$ target, as discussed in Appendix F. The ion chamber was centered on the beam at the beginning of the experiment. If the beam wandered beyond the limits of the ion chamber, this would show up as a variation in the cross-calibration of the ion chamber against the quantameters, whose position in the beam was checked at each calibration. As no such effect was observed, we conclude the ion chamber consistently monitored the whole beam.

A further question is to what extent the composition of the photon beam is altered by pair production. There are two effects:

1. The beam at the $He^3$ target contains electrons and positrons as well as photons;

2. Some of the beam energy is scattered out of the beam and not measured by the ion chamber.

There were about 0.05 radiation lengths of matter between the sweep magnet and the ion chamber distributed as follows:

| | |
|---|---|
| Air and $He^4$ bag upstream of target | .002 radiation lengths |
| target walls | .003 |
| $He^3$ in target | .016 |
| Air downstream of target | .025 |
| | .046 |

There were 0.01 radiation lengths of matter before the center of the target. Thus 99% of the total beam energy at the target was in the form of photons.

We now consider the second effect. The angle of a pair produced electron or positron with respect to the incident photon is roughly $M_e/E$. From the $He^3$ target the ion chamber had an angular radius of about 0.01 radians. Thus all electrons and positrons with energies greater than 50 MeV were collected by the ion chamber. Using the facts that the total pair production cross-section is very nearly constant for photon energies above 10 MeV and that the energy spectrum of the produced leptons is flat, we estimate that only 10% of the energy converted into pairs is not collected by the ion chamber. The 0.05 radiation lengths of matter convert 5% of the photon energy into pairs, so only 0.5% of the total beam energy was unmeasured.

The two effects of pair production have opposite signs. Thus the total energy in the form of photons at the target is 99.5% of the total energy collected in the ion chamber. This small syntematic effect has been included in the results of this experiment.

F. The $He^3$ Target

The helium-3 used as a target in this experiment was man-made. It came from the beta decay of tritium produced by neutron bombardment of lithium at the Lawrence Radiation Laboratory at Livermore. Our sample contained about 15 moles of $He^3$ , roughly one pint when liquid.

We first consider the composition of the 'helium-3'. As tritium has a half life of twelve years, there might well be a sizeable fraction of tritium remaining. As well as causing a background in the experiment, tritium would be a radiation safety hazard. However, as the boiling point of tritium is $20^oK$ while that of $He^3$ is $3.19^oK$, the tritium can be condensed out of a $He^3$-tritium gas mixture. The tritium content of our sample was below one part in $10^7$ [103].

The only significant admixture to the helium-3 was helium-4. A mass-spectrographic analysis[104] of our 'helium-3' established it to be 98.65% $He^3$ and 1.35% $He^4$. This admixture must be taken in account as $He^3$ and $He^4$ can remain in solution even at $0^oK$. Figure 6.7 shows the liquid phase diagram for $He^3$-$He^4$ mixtures under saturation vapor pressure[105,106]. As discussed below, the temperature of the liquid in the target was around $1.5^oK$. At this temperature, we see that the $He^3$ and $He^4$ are still in solution. Further, the mixture is not a superfluid although the temperature is below the $\lambda$ point for pure $He^4$.

The correction for the presence of $He^4$ appears in two ways. First, the density of the $He^3$-$He^4$ solution is about 0.5% greater than for pure $He^3$. From Table A7 of reference 105, I estimate that around $1.5^oK$, a 98.65% solution has a molar volume 0.17 c.c. less than pure

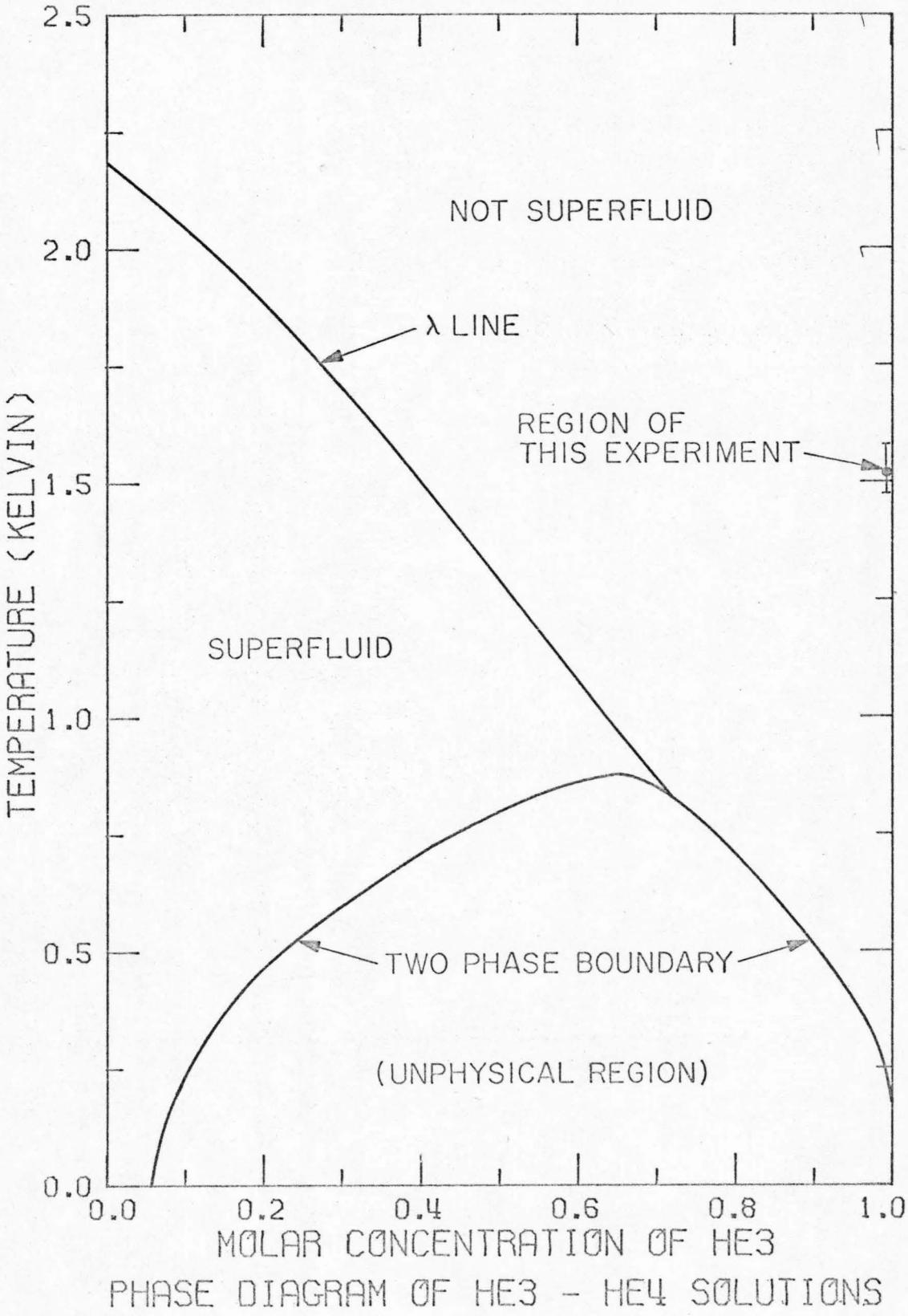
2.5
2.0
1.5
1.0
0.5
0.0
TEMPERATURE (KELVIN)
NOT SUPERFLUID
λ LINE
REGION OF
THIS EXPERIMENT
SUPERFLUID
TWO PHASE BOUNDARY
(UNPHYSICAL REGION)
0.0
0.2
0.4
0.6
0.8
1.0
MOLAR CONCENTRATION OF HE3
PHASE DIAGRAM OF HE3 - HE4 SOLUTIONS

Figure 6.7

$He^3$. Second, the solution is only 98.65% $He^3$, so a molar volume contains only 98.65% of a mole of $He^3$.

We now consider the target itself, shown schematically in Figure 6.8. The $He^3$ gas is kept in a closed system consisting of the storage tank (not shown), the condensor, and the target cup. The condensor is in good thermal contact with the reservoir of liquid $He^4$. The $He^3$ is condensed and cooled by the evaporation of $He^4$ from the reservoir. The $He^4$ lost by evaporation is replaced by liquid $He^4$ from a dewar. To reduce the evaporation, a liquid nitrogen jacket surrounded the $He^4$ reservoir. Further, a vacuum was maintained in the regions between the outer wall and the nitrogen jacket, and between the nitrogen jacket and the $He^4$ reservoir.

The target cup was suspended from the $He^3$ condensor by two pipes which also served to circulate the liquid $He^3$. The cup was surrounded by a chamber of $He^4$ gas in equilibrium with the liquid $He^3$ in the reservoir, in order to minimize the chance of a rupture of the cup. This chamber was surrounded by two concentric vacuum jackets, whose walls are shown in Figure 6.8 as heat shields. The metal shell of the target was replaced by a mylar window in the region of the target cup to reduce the multiple scattering of emerging particles. A particle had to traverse twenty-three mils of mylar and four mils of aluminum to escape.

The target consumed about thirty liters, or 1000 moles, of $He^4$ a day. The latent heat of vaporization of $He^4$ is about twenty calories per mole, so 20,000 calories a day were liberated. Assuming a running

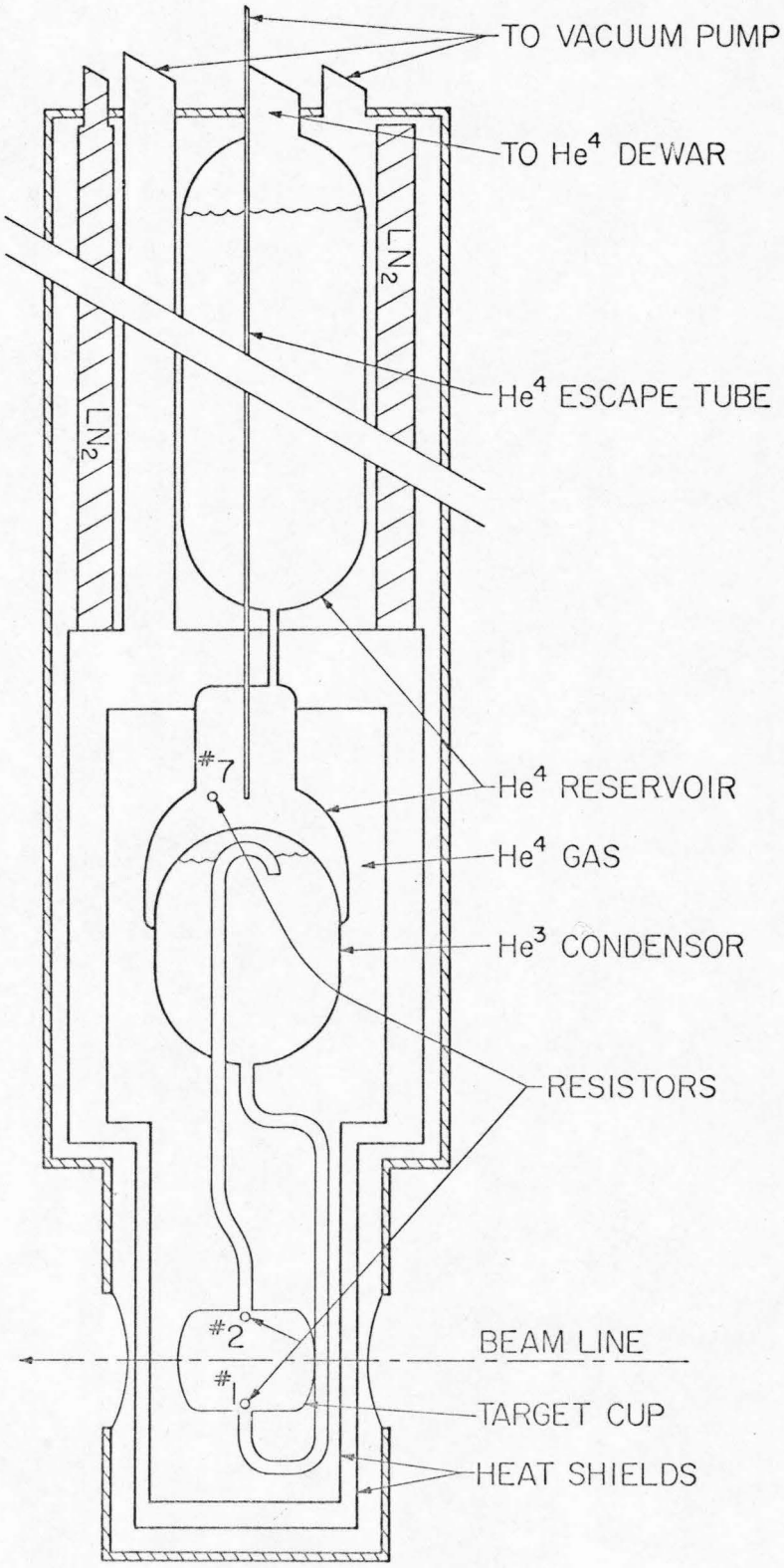


Figure 6.8 The $He^3$ Target

temperature of 1.5°K, 2000 calories were used in cooling the $He^4$ from its boiling point of 4.21°K. The latent heat of vaporization of $He^3$ at 1.5°K is about ten calories per mole so condensing and cooling the fifteen or so moles of $He^3$ took 150 calories. These calories were not needed every day, but only after the $He^3$ was entirely boiled. Thus about 90% of the cooling went into various heat losses through the walls of the target. Most of the loss occurred in the transfer pipe from the liquid $He^4$ dewar to the reservoir. If the $He^4$ supply were turned off, it would take at least twelve hours for the $He^3$ to boil completely. Hence the heat loss out of the $He^3$ system was only about ten calories per hour.

The temperature of the $He^3$ was monitored by measuring the resistance of one of eight carbon resistors mounted at various places within the target (see Figure 6.8). The resistors had a nominal value of 300 ohms at room temperature, but at 1.5°K the resistance would be about 200,000 ohms. The temperature versus resistance calibration of the resistors was performed according to the method of Reference 107.

The process of monitoring a resistor caused a heat source inside the target due to joule heating. Therefore, we observed resistor seven, which is in the condensor, rather than resistor two in the cup. The observations could then be made continuously and they were recorded at several times each run. A calibration of resistor two against resistor seven showed the cup to be cooler than the condenser by about 0.05%.

Figure 6.9 shows the density of liquid $He^3$ at saturation vapor pressure as a function of temperature, taken from table A10 of

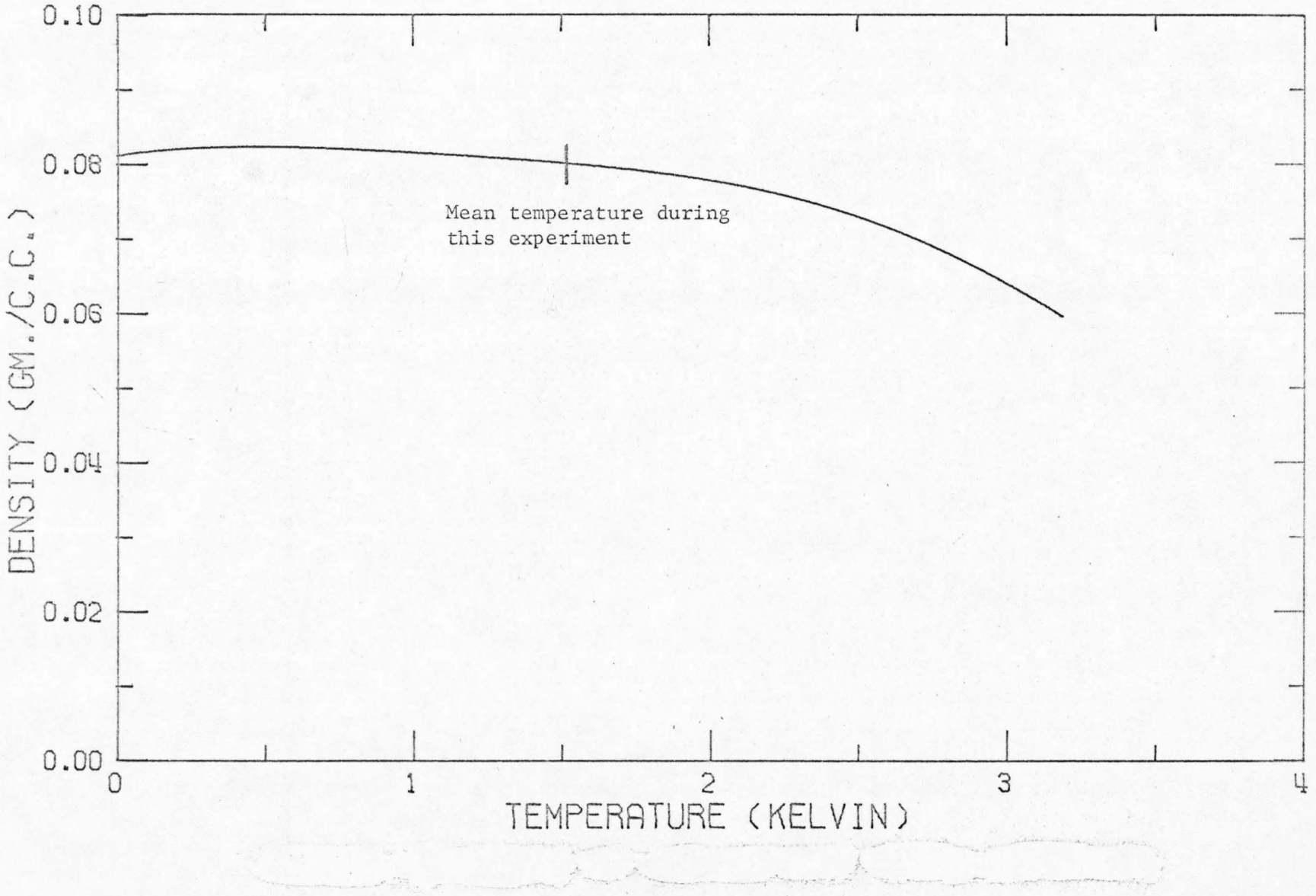


Figure 6.9 Density vs. Temperature of Liquid $He^3$ at Saturation Vapor Pressure

Reference 105. Maximum density is at 0.5°K but a gently sloping plateau exists up to 2°K. The $He^3$ target was designed to run at 1.5°K so that the density would not be greatly affected by temperature changes, while the expense of maintaining this temperature is not prohibitive. An average temperature was calculated for each run using the observations described above. The mean over the 100 or so runs was 1.53°K with a variance of 0.03°K. The mean density was 0.0802 gm/cc with a variance of 0.0002. Variations within a run were larger with T ranging between 1.45 and 1.6°K (except for brief periods of higher values when the liquid $He^4$ reservoir needed replenishing). We estimate the resulting uncertainty in the density for a given run as 1/2%.

The target cup was in the shape of a cylinder with spherical caps on each end. The axis of the cylinder was along the central ray of the photon beam. The maximum length of the target was 10.4 cm, with the radius equal to 3.78 cm. As the measured cross-sections are inversely proportional to the length of the target (for a given number of events collected), it is important to establish the effective length accurately. By effective length, I mean the length of a right circular cylinder target which produces the same event rate as the actual one. Using the radial dependence of the beam intensity discussed in Appendix D, and the known shape of the spherical caps, I calculate an effective length of 3.94 inches, and estimate the error at 1/2%.

The beam was checked daily to assure that it was centered on the target; it never wandered by more than 0.05 inches.

The only uncertainty associated with the target was whether the

liquid $He^3$ contained bubbles. As the various heat shields prevented the target cup from being observed directly, we must rely on indirect evidence. That it took at least twelve hours for the entire liquid $He^3$ to boil entirely without any $He^4$ cooling argues strongly against bubbling: if the lifetime of a bubble were one second, only 1/40,000 of the $He^3$ would be in the form of bubbles at any one time. Further, the target was operated at 1.7°K below the boiling point. I estimate the heat generated by ionization of the $He^3$ by electron-positron pairs in the beam at about one calorie per hour. As the beam was about 2-3/8 inches in diameter, this heat source was not localized, and was unimportant.

A telescope consisting of three scintillation counters aimed at the target was designed to monitor whether the target was full. However, as shielding was added around the spark chambers during the course of the experiment, the monitor telescope was blocked. For the portion of the experiment when it was working, the monitor revealed no fluctuation from run to run beyond 5% or so. The measured cross-sections also show this kind of consistency among the various runs.

We conclude there was no significant bubbling in the target, and no correction for such an effect has been made.

G. Calibration of the Analyzing Magnet

The calibration of the analyzing magnet used in the experiment was done with the so-called floating wire technique. The computer controlled method of data-taking using magnetostrictive wands is described in detail in Reference 108. This Appendix discusses the principle of the floating wire technique briefly, summarizes its application to the present experiment, and derives a correction for the effect of gravity on the calibration.

1. Principle of the Method

The floating wire technique is based on the similarity of the equation of motion of a charged particle in a magnetic field, and the equation for the curvature of a current carrying wire in the same field. For a particle with moment $\bar{P}$, velocity $\bar{V}$ and charge e,

$$d\bar{P}/dt = e\bar{V} \times \bar{B}$$

where $\bar{B}$ is the magnetic field. Letting $\hat{\ell} = \bar{P}/P$ be the unit tangent to the trajectory and $ds \equiv vdt$ be the arc length,

$$d\hat{\ell}/ds = (e/P)\ \hat{\ell} \times \bar{B} \qquad (G.1)$$

Neglecting gravity, a wire under (uniform) tension T, carrying current I obeys

$$d\hat{\ell}/ds = (I/T)\ \hat{\ell} \times \bar{B} \qquad (G.2)$$

Thus the "orbit" of a wire suspended in the field exactly follows a possible trajectory of a particle with momentum

$$P = eT/I$$

In practical units, this is

$$P(\text{MeV/c}) = 2.9398\ T\ (\text{grams})/I(\text{amps}) \qquad (G.3)$$

Note that in a field free region, both a particle's trajectory and wire "orbit" are straight lines. A correction for the effect of gravity is discussed in Section 4.

2. Orbits in the Mid-Plane of the Magnet Gap

The momentum analyzing properties of a magnet can be investigated by measuring representative floating wire orbits. Only orbits lying in the mid-plane of the magnet gap were measured. Corrections for orbits not in this plane were made using a procedure discussed in Section 3.

Figure 6.10 illustrates the orbit parameters which were measured. Two rectangular coordinate frames were defined, one on either side of the magnetic field region. The z-axes were in the direction of the particle's flight, and the x-axes lay in the mid-plane of the magnetic field. For each orbit considered, the slopes and intercepts of the straight line segments of this orbit were determined, as well as its equivalent momentum, calculated from equation (G.3). Thus for each orbit, five parameters were measured: P, $x_1$, $\tan \theta_1$, $x_2$, $\tan \theta_2$ where the $x_i$ are the intercepts and $\tan \theta_i$ are the slopes. An orbit in the mid-plane is completely determined by three parameters so that any two may be expressed as a function of the other three. In this experiment the $x_i$ and $\theta_i$ are known and P is desired. To take full advantage of the data, $\theta_1$ and $\theta_2$ were combined into $\theta = \theta_1 - \theta_2$, and P was expressed as a fourth order polynomial in $x_1$, $x_2$ and $\tan \theta$.

$$P = P_o + a_1 x_1 + a_2 x_2 + a_3 \tan \theta \ldots\ldots + a_{34} x_1 x_2 \tan^2 \theta$$

The orbit which would have all slopes and intercepts zero is called the

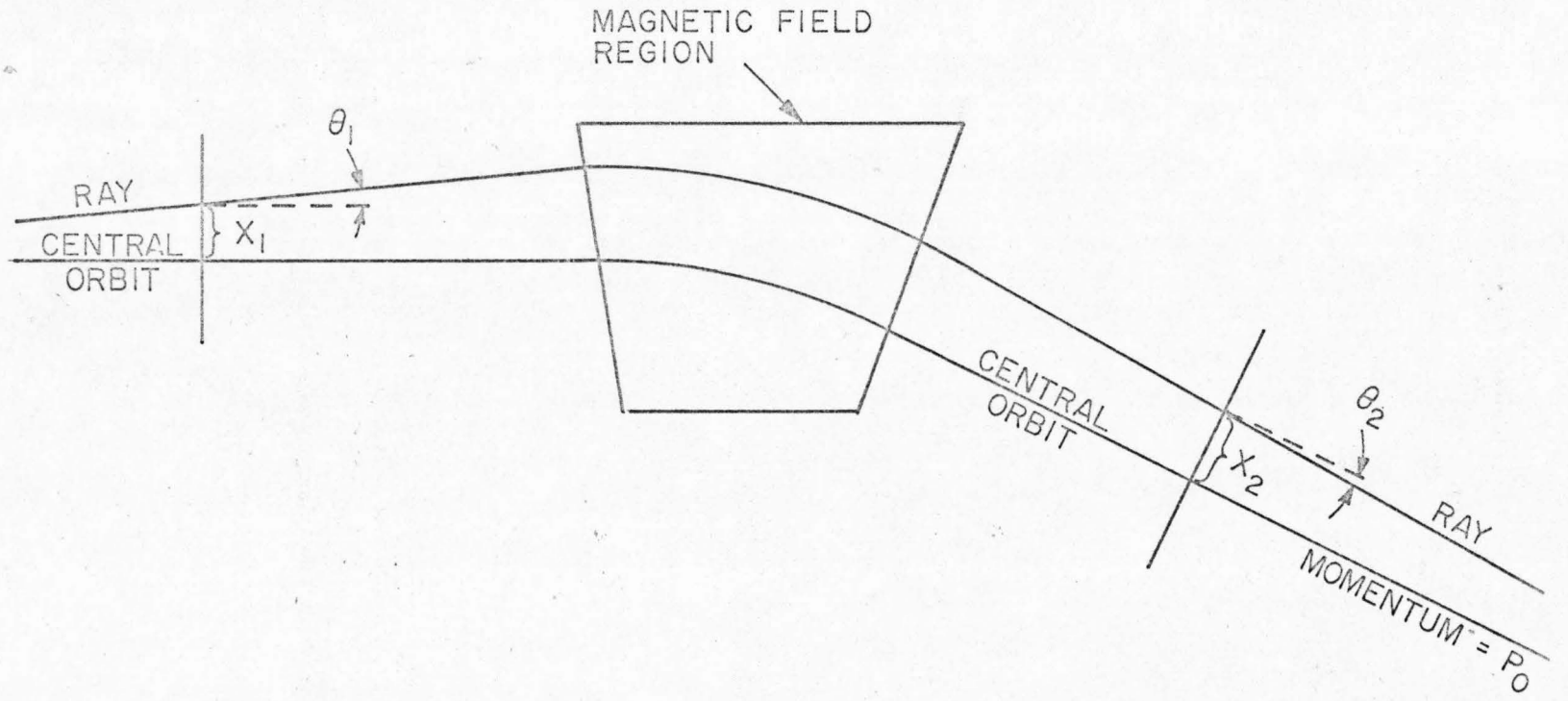


Figure 6.10 Orbits Measured in the Magnet Calibration

central orbit, and its equivalent momentum is called the central momentum, which is just the constant $P_o$.

During the experiment, twenty-seven different magnetic field strengths were used ranging from 2.8 to 11.1 kilogauss. In principle, only the constant $P_o$ should change from setting to setting while the 34 $a_i$'s remain fixed as they depend only on the shape of the field. To test this, approximately 180 orbits were measured at each of four field strengths and the thirty-five constants calculated by a least-squares fit. By considering $\Delta P = (P-P_o)/P_o$, one magnet setting could be compared against the other. The r.m.s. value for $\delta = \Delta P_{calculated} - \Delta P_{measured}$ was typically 0.3% for any one setting, and using the coefficients $a_i$ from one setting to calculate $\Delta P$ for another also gave an r.m.s. value of $\delta = 0.3\%$. Hence the assumption that the shape coefficients $a_i$ are independent of $P_o$ is justified. The orbits from all four settings were then combined to calculated

$$\Delta P = a_1 x_1 + a_2 x_2 + \ldots . a_{34} x_1 x_2 \tan^2 \theta$$

A least squares fit using 432 out of 542 orbits gave $\delta_{r.m.s.} = 0.2\%$, which is taken as the accuracy of the fit.

The value of $P_o$ must be known for the other twenty-three settings of the field strength to complete the analysis. At each setting, six orbits were measured, and $P_o$ calculated using the $a_i$ from the four settings discussed above. Also, at all settings, an NMR probe measured the field strength which is proportional to $P_o$. The proportionality constant was calculated for all settings and found to be the same to within 0.2%.

In addition to fitting P as a function of $x_1$, $x_2$ and tan $\theta$, fits were made to $x_2$ and $\theta_2$ as functions of $x_1$,$\theta_1$ and $\Delta P$. These fits are used in the geometric efficiency calculation to determine the acceptance of the magnet.

3. Properties of Orbits not in the Mid-Plane

If a particle trajectory does not lie in the mid-plane of the magnet, it will in general follow a helical path. Defining $\alpha$ as the angle of the helix with respect to the mid-plane, equation (G.1) shows that the projection of the orbit onto the mid-plane is exactly that of a particle with momentum P$\cos\alpha$ whose orbit is in the mid-plane. Thus if $x_1$, $x_2$,$\theta_1$ and $\theta_2$ are measured for a helical orbit, and P is calculated using the fit described in the previous section, a correction

$$P = P_{fit}/\cos\alpha$$

must be made. In the present experiment, $\alpha$ was limited to $|\alpha| \leq .04$ radians. This correction is at most 0.1%. In making this correction, $\alpha$ need not be determined precisely.

The difficulty in measuring $\alpha$ is that the non-uniform fringe fields of the magnet cause $|\alpha|$ to increase as the particle passes through them. Thus the slope with respect to the mid-plane of the straight segments of a particle trajectory is different before and after it passes through the field. This effect is not important in determining the particle's momentum, but is very important in determining the acceptance of the magnet. The "defocusing" which occurs in the direction perpendicular to the mid-plane reduces the effective width of the magnet gap. A 5% error in this dimension will manifest itself as a

systematic 5% in the final scattering cross-section.

In earlier calibrations of the magnet[109], a first order theory was used to relate the properties of orbits outside the mid-plane to those lying in it[110]. Let the y axis be perpendicular to the mid-plane of the magnet. The theory relates the slope and intercept of an orbit projected into the y-z plane after the magnet to the projected slope and intercept before it. There are six constants to be determined, and in the first order theory, the fits for $x_2$ and $\theta_2$ in terms of $x_1, \theta_1$ and $\Delta P$ give six relations involving these constants. In addition, four of the six parameters can be determined to within about 1% from the physical dimensions of the magnet. The consistency among these ten relations for the six constants is not good. Taking different subsets of the relations, the predictions for the defocusing effect vary by 5%. In face of this discrepancy, the above use of the first order theory was abandoned.

As an alternative, it was conceived that the observation of particles in the magnet in the course of the experiment itself could be used to calculate the defocusing. This was possible because the wire spark chambers determined the particles' tracks both before and after the magnet. In practice, this was difficult because of multiple Coulomb scattering. An additional complication was that the "fan" veto counters on the pole faces were removed in this experiment. This left the question of whether the particles scattered off the pole tips to be answered by the slopes and intercepts of the tracks in the wire chambers. Again, multiple scattering made the approach less reliable than desired.

To calculate the defocusing effect, clean tracks were used from

two runs in which the particles' momenta were high, and hence multiple Coulomb scattering was minimized. A reasonable first order fit was achieved of the form

$$y(\text{exit of magnet}) = 1.14\ y(\text{at target}) + 162.0\ y'\ (\text{at target})$$

The R.M.S. deviation of observed and predicted values was 0.17". The last previous calibration of the magnet[109] used the fit

$$y(\text{exit}) = 1.22\ y(\text{target}) + 174.0\ y'(\text{target})$$

The magnet's pole tips differed slightly from the present configuration when this fit was made. The most reasonable fit obtained by using first order magnet theory for the present configuration was

$$y(\text{exit}) = 1.11\ y(\text{target}) + 166.0\ y'(\text{target})$$

The first fit was used in the data anlysis. Based on the discrepancy between it and the third fit, the possible systematic error is taken as 3%.

4. Correction for Gravity

Both equations (G.1) and (G.2) must be corrected for the effect of gravity. However, the correction to (G.1) is neglible since all the protons and deuterons in the experiment had velocities greater than 0.1 c, and a particle traveling at 0.1 c for a distance of twenty feet falls about $10^{-13}$ meter. Equation (G.2) in the presence of gravity becomes

$$T\frac{d\hat{\ell}}{ds} + \frac{dT}{ds}\hat{\ell} - \rho g\hat{x} + I\hat{\ell}X\bar{B} = 0$$

where, for this section, $\hat{x}$ is vertical, and the y-z plane horizontal. In the present case, $\hat{\ell}$ lies in the x-z plane, and $\bar{B}$ is in direction $\hat{y}$. The vector equation may be decomposed into components along the (orthogonal) directions $\hat{\ell}$ and $d\hat{\ell}/ds$ yielding

$$\frac{dT}{ds} = \rho g \sin\theta \qquad (\text{along } \hat{\ell})$$

and $$T\frac{d\theta}{ds} = \rho g \cos\theta - IB \quad (\text{along } d\hat{\ell}/ds)$$

where $\theta$ is the angle between $\hat{\ell}$ and $\hat{z}$ and $d\theta/ds = |d\hat{\ell}/ds|$

By noting that $ds = \sin\theta\, dx$, the first equation can be integrated to give

$$T(x) = T_o\left(1 + \frac{\rho g}{T_o} x\right)$$

Since $\frac{\rho g}{T_o} \sim 10^{-6}$ cm$^{-1}$ and $x \lesssim 20$ cm

this effect will be neglected.

The second equation can be written

$$-\frac{d\theta}{ds} = \frac{IB}{T} - \frac{\rho g}{T}\cos\theta \qquad (G.4)$$

Since the radius of curvature of the orbit is $R = -1/(d\theta/ds)$, it varies with $\theta$ and is slightly larger than in the absence of gravity. As $\rho g/T$ is small, it is a good approximation to replace $\cos\theta$ by its average. In this approximation, $d\theta/ds$ is constant so that the orbit is circular. By comparing with equation (G.1), the equivalent momentum of the wire in the presence of gravity is

$$P = P_1 \left(\frac{1}{1 - \frac{P_1}{B} \cdot \frac{\rho g}{2.94\ T} \cdot (\cos\theta)_{ave}}\right)$$

where $P_1 = 2.94\ T/I$. The size of this effect is about 0.1% for this experiment.

Summing up, the effect of gravity on the wire <u>inside</u> the magnetic field is to flatten the orbit slightly so as to make the equivalent momentum higher.

Outside of the magnetic field region, the wire orbit no longer consists of straight lines, but of catenaries, as illustrated in Figure

6.11. Inside the magnet, the orbit is circular to a good approximation but outside the catenary orbit rises above the ideal straight line extension of the orbit inside the magnet. The catenary is described by equation (G.4) with B = 0. If we take T and cos θ to be constant, the catenary is approximated by a parabola. Defining D(s) as the perpendicular displacement between the ideal orbit and the actual parabolic orbit,

$$D(s) = 1/2\ s^2 \frac{\rho g}{T} \cos \theta$$

where S is measured from the effective edges of the magnet field.

In practice, the wire orbit analysis was done by fitting a straight line to the parabola by sampling the orbit at four points. Corrections to the slope and intercept were made using a fit to the expression for D(s) at the same four points. The corrections to the slope were of the order of five milliradians, while the intercepts changed by as much as 0.2 inches.

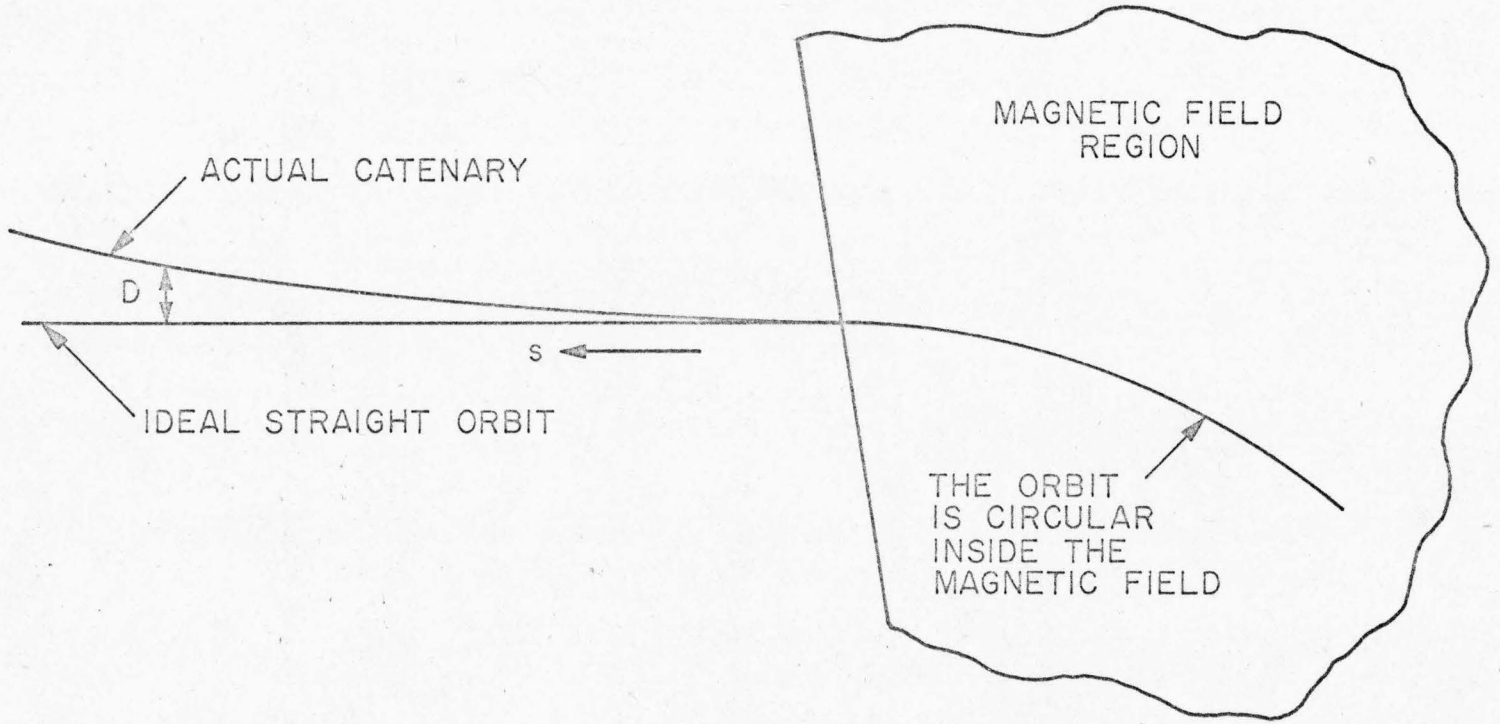


Figure 6.11 The Correction for Gravity in the Magnet Calibration

H. Example of the Background Subtraction Procedure

We illustrate the subtraction procedure by considering it for a particular run, number 74, in detail. In this run, the proton was detected in the magnet array.

The first step is to use the pulse height in counter RS1 (see Figure 3.6) to throw out events in which no deuteron was observed in the range array. To obtain a clear indication of the minimum pulse height caused by a deuteron, the RS1 spectrum was plotted for events having a coplanarity within $\pm 1^{o}$ and a missing mass excess within $\pm 10$ MeV/$c^2$, as in Figure 6.12. The ratio of foreground to background events in this sample is very high. For this case, a pulse height of 350 was taken as the minimum for deuterons. In the remaining steps of the subtraction process, only events with RS1 pulse heights above this minimum were considered. There were 944 such events in run 74. Figures 6.13 and 6.14 show distributions of coplanarity and mass excess for these events.

Next, the extent of the values of coplanarity and missing mass excess for foreground events is determined. By considering only events with a very high RS1 pulse height, the background can be suppressed. Figures 6.15 and 6.16 show the coplanarity and mass excess for events with RS1 pulse height greater than 800. From this foreground, events were conservatively estimated to have coplanarities within $\pm 5^{o}$ and mass excesses within $\pm 60$ MeV/c . All events lying outside these limits are taken as belonging to the background and constitute the sample $N_o$ discussed earlier. There were 277 such events, leaving 667 events as the

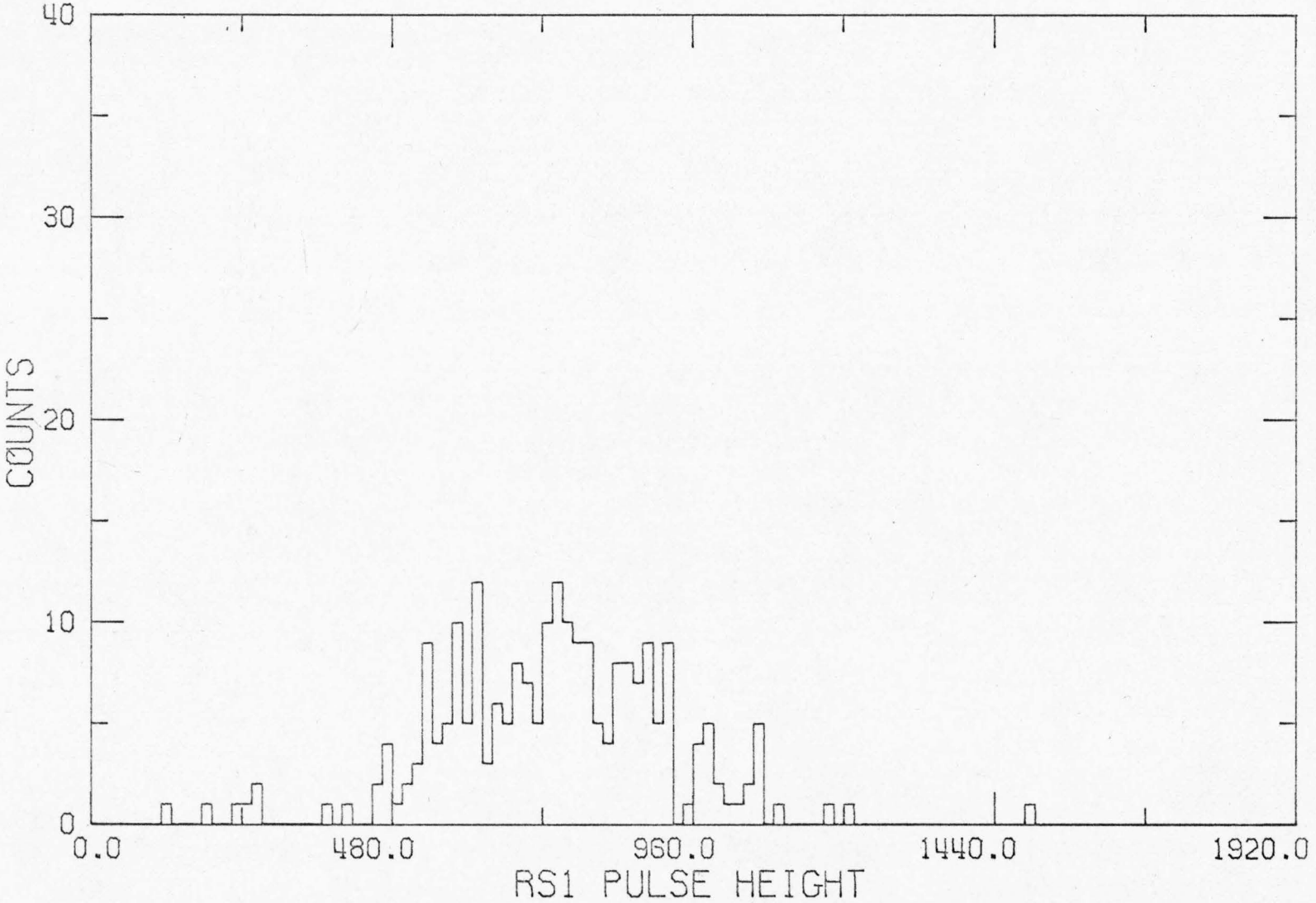


Figure 6.12 The Pulse Height Spectrum in Counter RS1 for Events with Small Coplanarities and Missing Masses

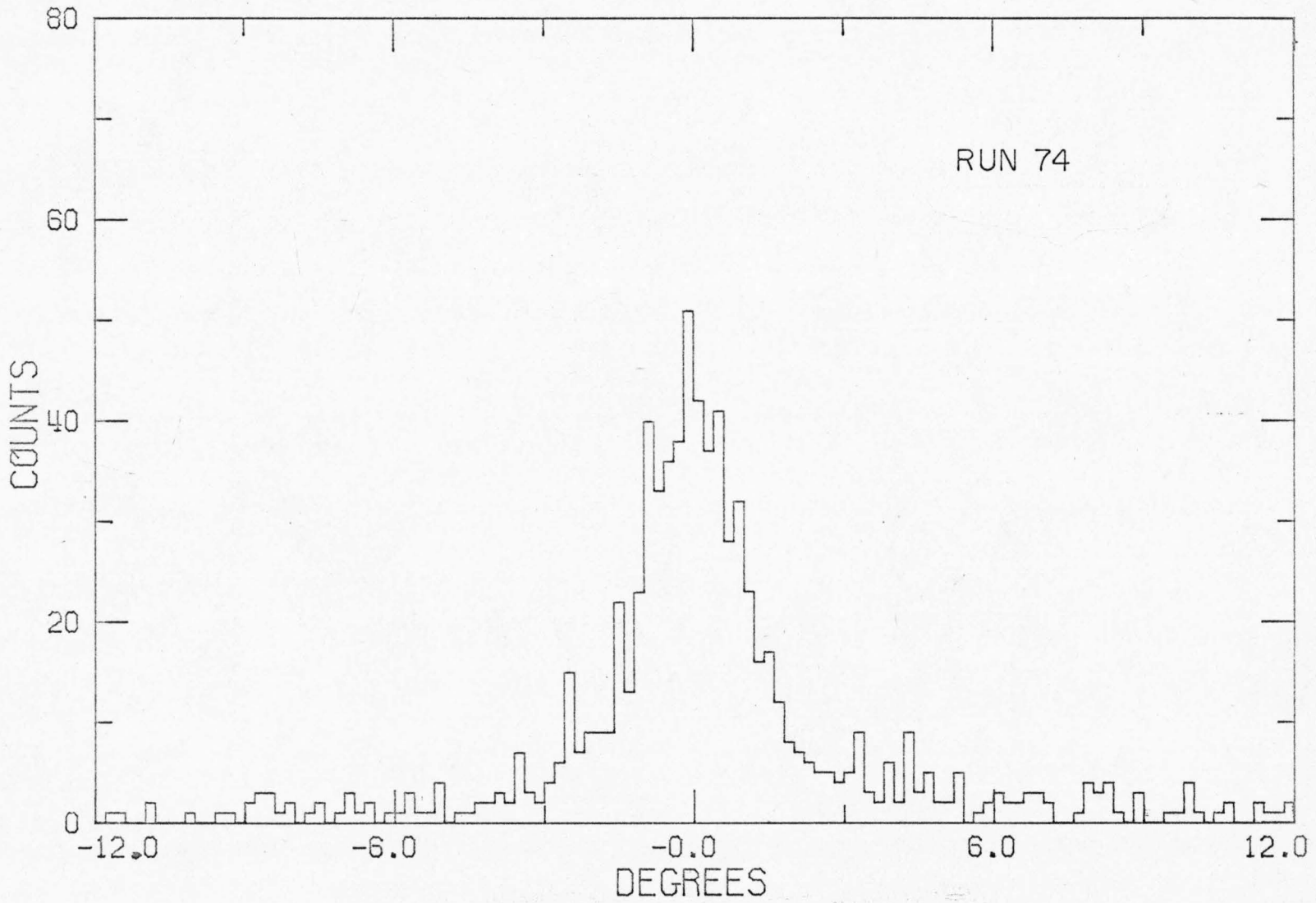


Figure 6.13 The Coplanarity Distribution for Foreground and Background Events

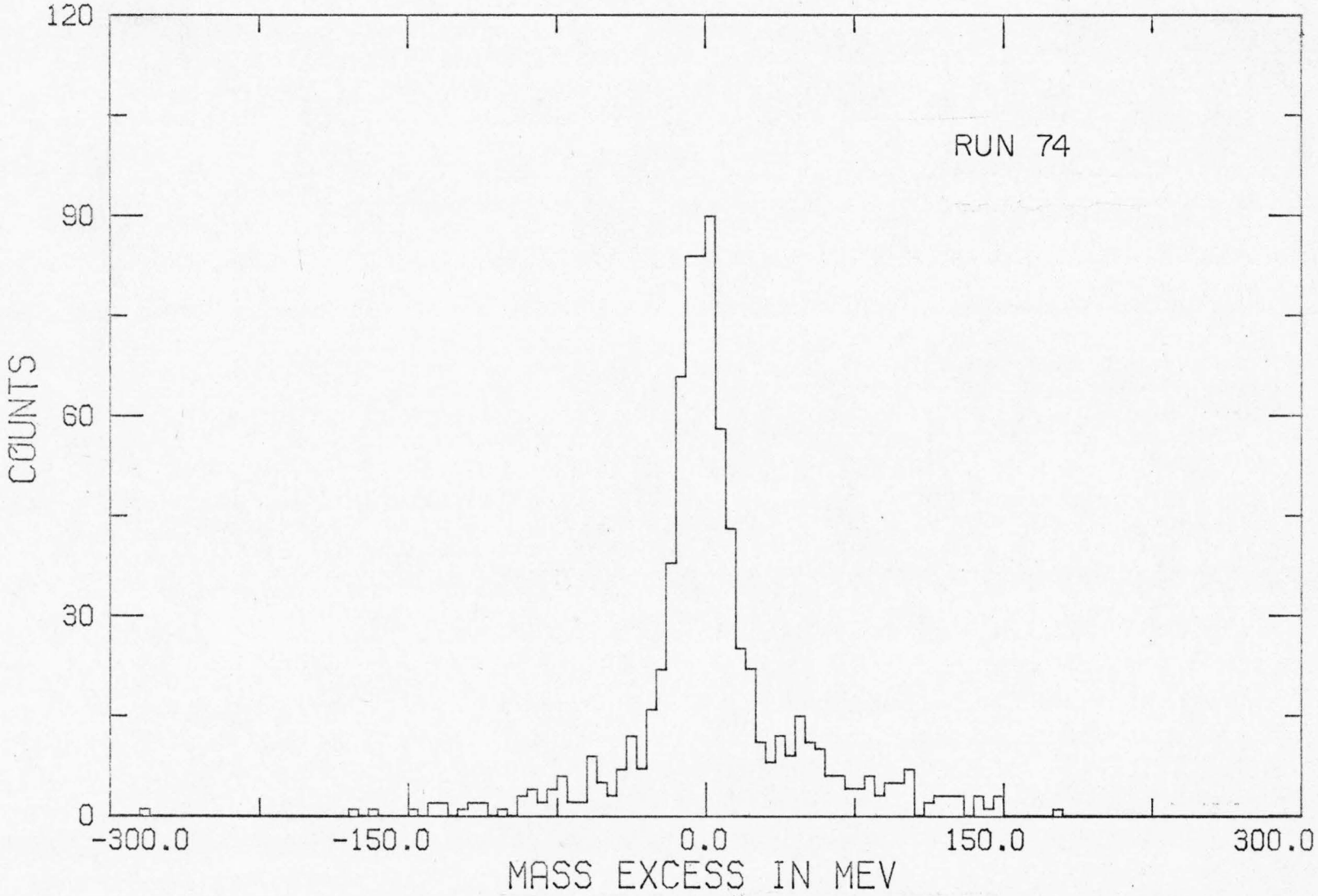


Figure 6.14 The Missing Mass Distribution for Foreground and Background Events

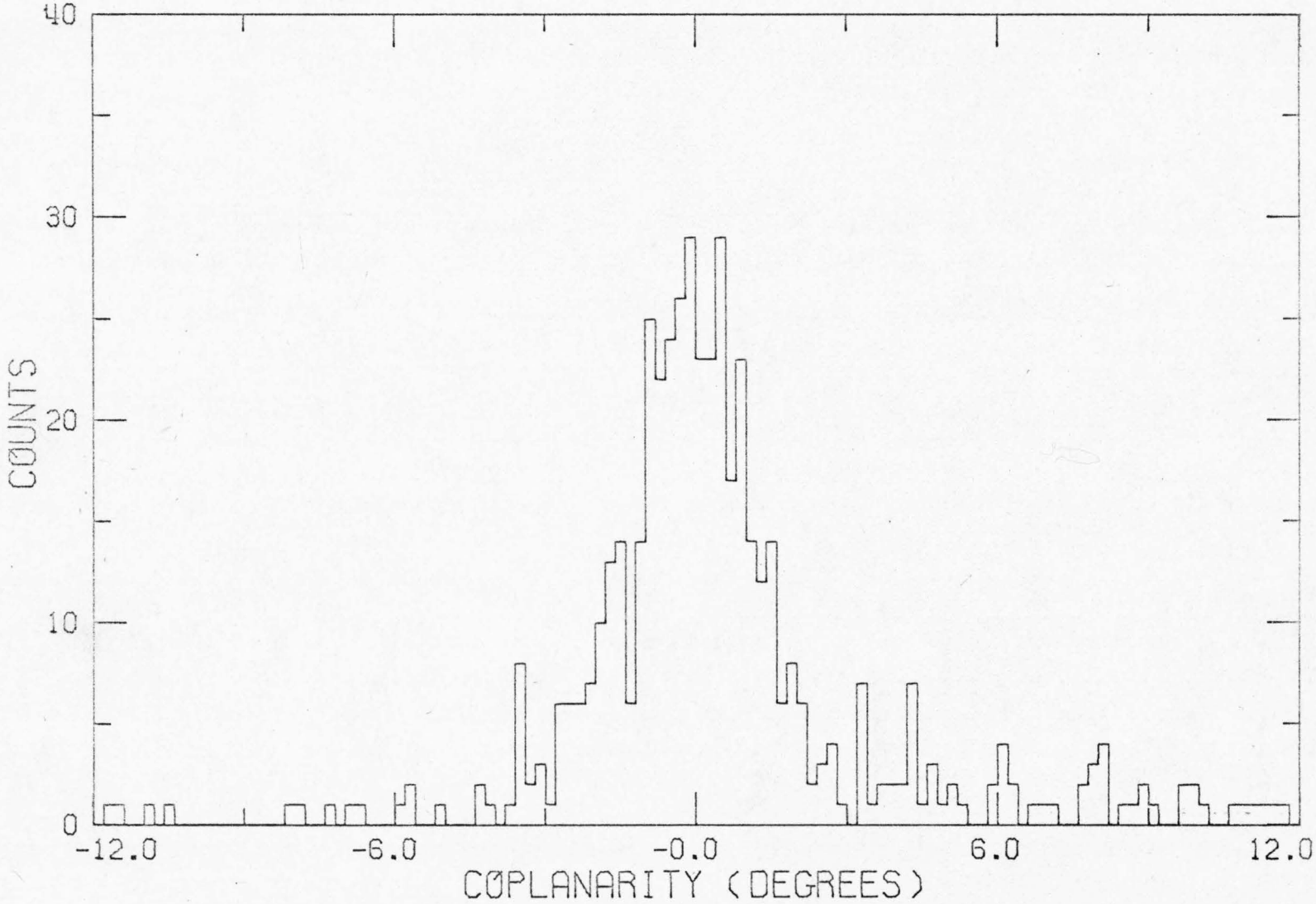


Figure 6.15 The Coplanarity Distribution for Events with Large Pulse Heights in Counter RS1

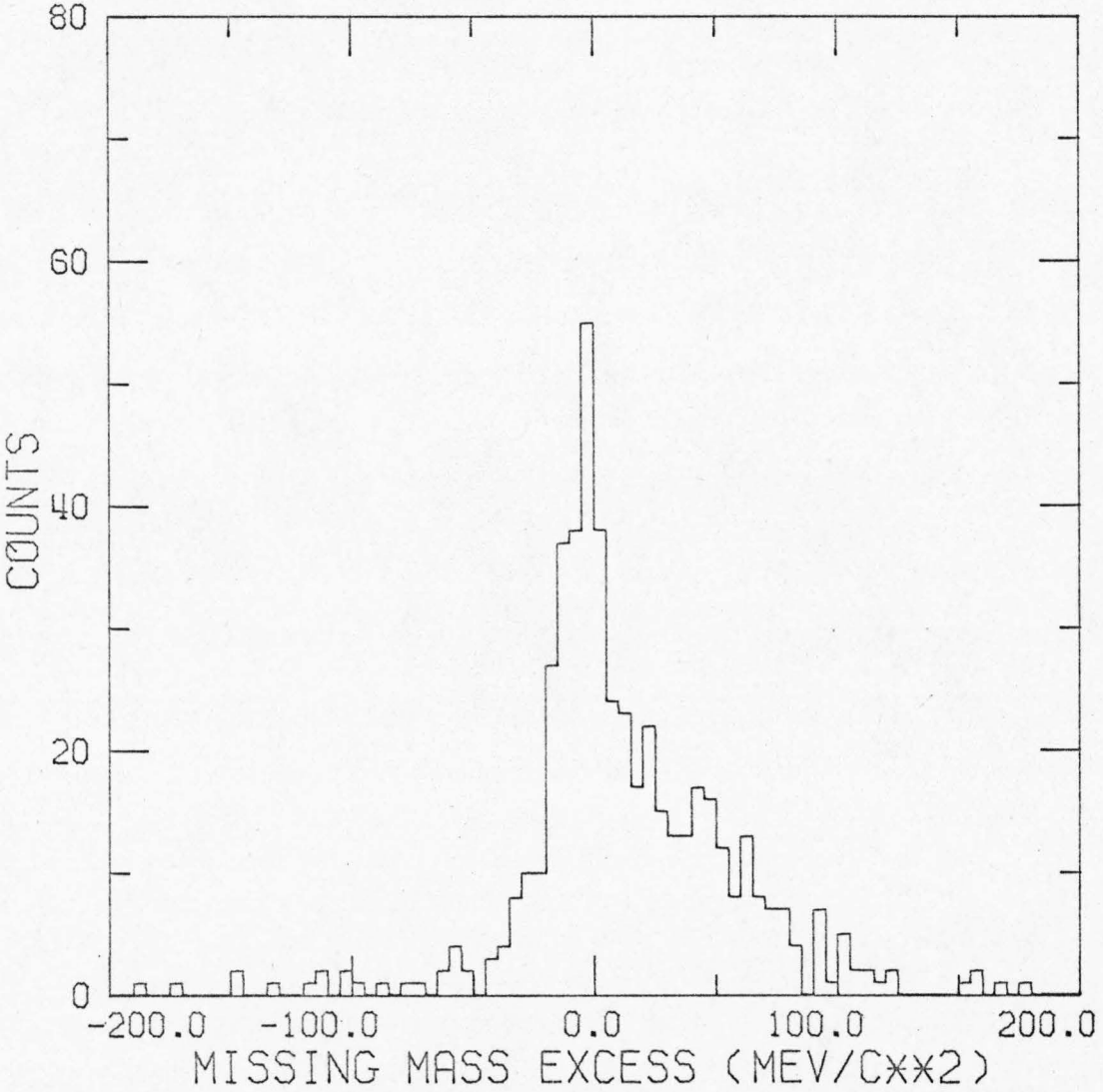


Figure 6.16 The Missing Mass Distribution for Events with Large Pulse Heights in Counter RS1

mixture of foreground and background to be separated.

The 277 definite background events were used to simulate the entire background sample by a Monte Carlo calculation. Lists were made of the intersections of the tracks with counters RS1 and MS2, and of the momenta measured in the magnet. Multiple Coulomb scattering caused the reconstruction of event vertices in the $He^3$ target to be uncertain for most runs. Therefore, a list of possible event vertices was made up using a random number generator on a computer, with the restriction that the vertices must lie within the boundaries of the target, and have a radial distribution as that given in Appendix D. From these lists, 5000 'events' were constructed by choosing at random one value from each list and combining these into a single event. As there were eight lists of length 277, there are $8^{277}$ different 'events' which might be constructed in this way. Figure 6.17 and 6.18 show the coplanarity and mass excess distributions for these 5000 'events'. These have shapes as might be inferred for the background events in Figures 6.13 and 6.14. Of the simulated background events, 1132 were inside the foreground region as defined above, and 3868 outside. Thus $277 \cdot 1132/3868 = 81.1$ background events are predicted to lie in the foreground region.

Figures 6.19 and 6.20 show the results of the background subtraction in coplanarity and missing mass excess. The spectra of Figures 6.17 and 6.18 have been normalized to 81.1 events inside the foreground region and then subtracted from the spectra of Figures 6.13 and 6.14.

Finally, we can obtain the corrected distribution of events as

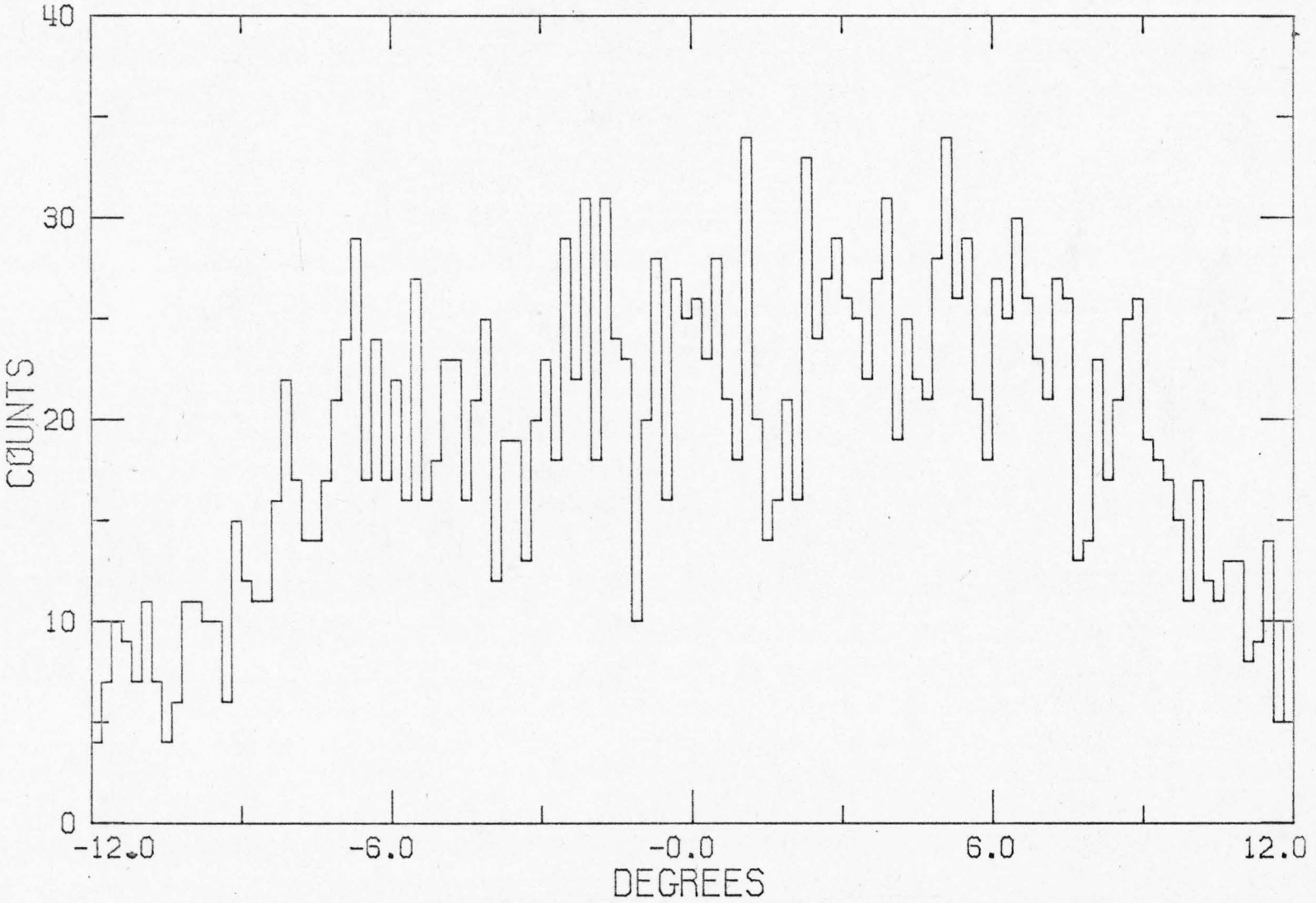


Figure 6.17 The Coplanarity Distribution for Background Events Generated by the Monte Carlo Calculation

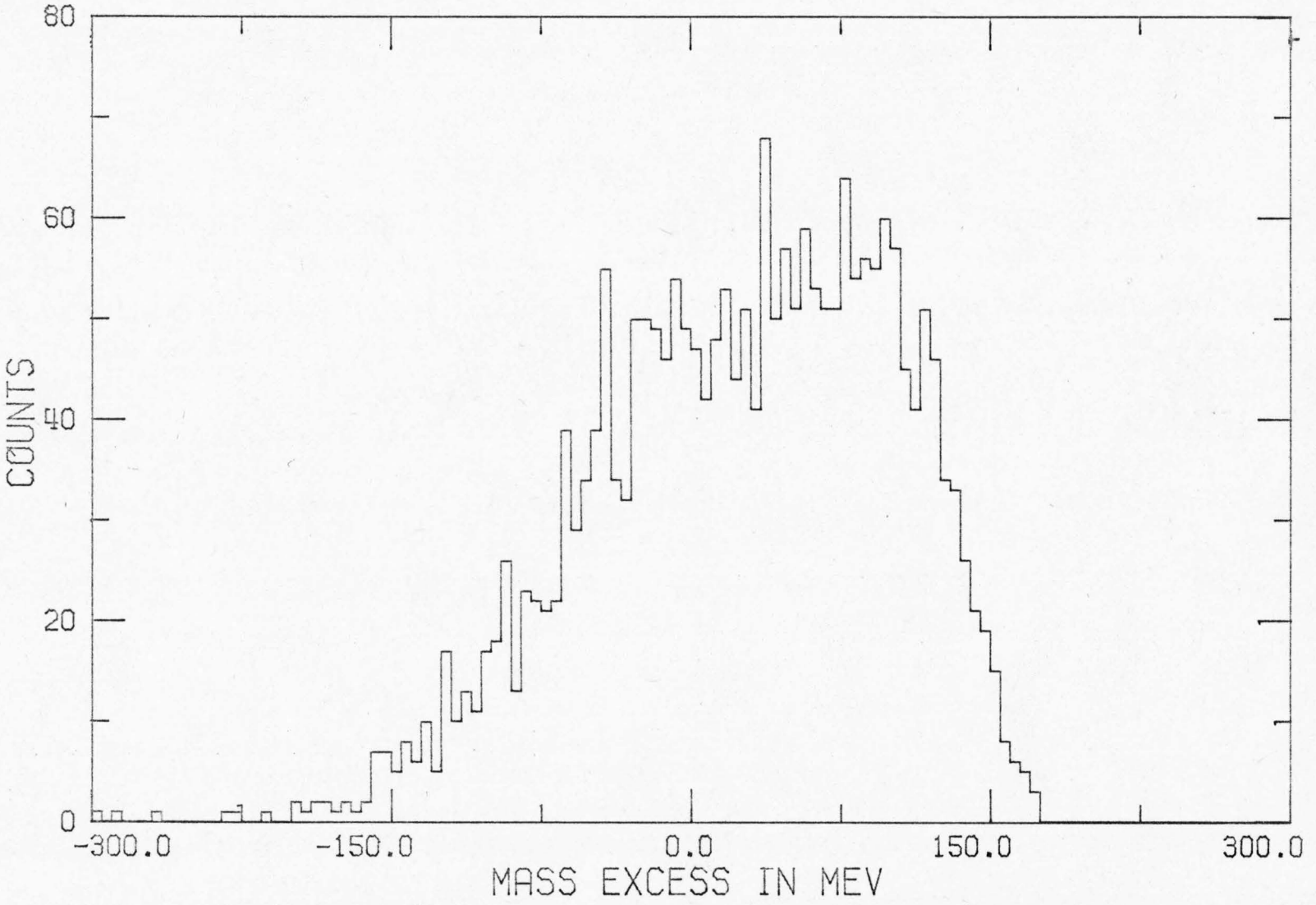


Figure 6.18 The Missing Mass Distribution for Background Events Generated by the Monte Carlo Calculation

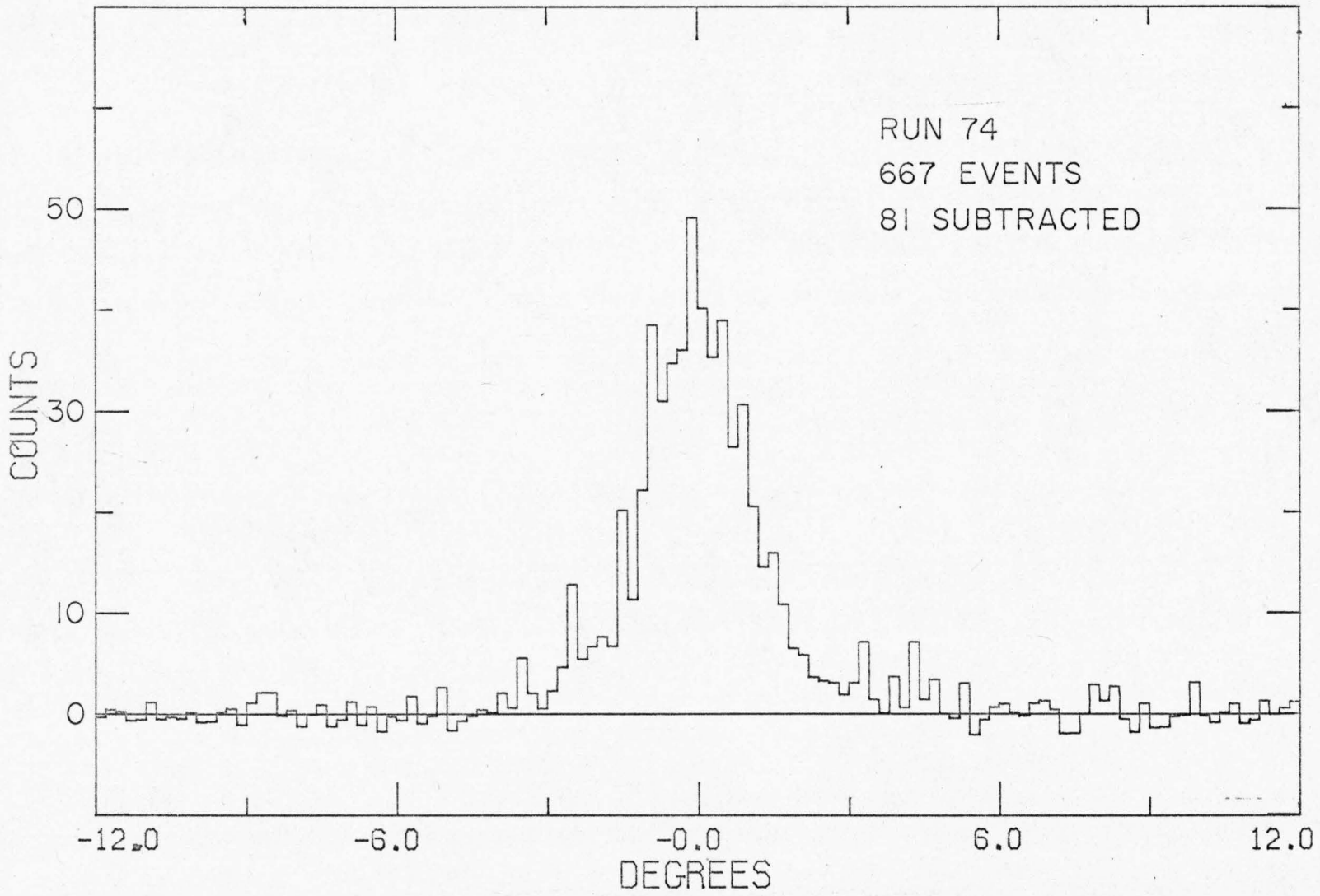


Figure 6.19 The Subtracted Coplanarity Distribution

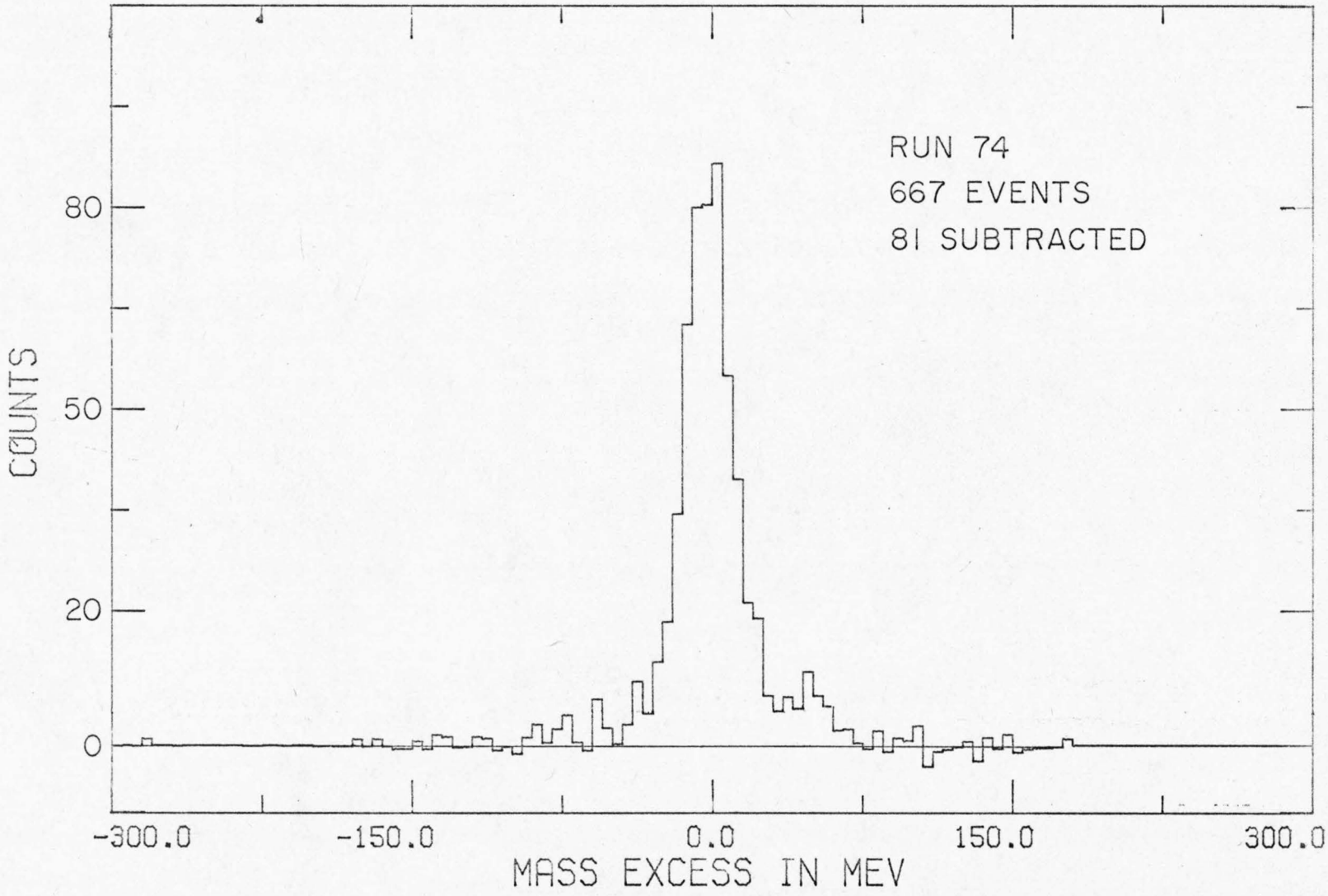


Figure 6.20 The Subtracted Missing Mass Distribution

a function of photon energy. Figure 3.8 shows the distribution of all 667 events in the foreground region and (in black) the distribution of the 81.1 background events. The difference between these distributions is the final result of the background subtraction procedure.

The subtraction process is very similar for runs in which deuterons rather than protons are detected in the magnet array. The only difference is that the values of the time of flight and MS3 pulse height play the role of the RS1 pulse height discussed above.

I. Survey of Possible Reciprocity Tests

In general, a reciprocity test of time reversal invariance in the electromagnetic interaction compares the forward and reverse reactions $\gamma + A \leftrightarrow B + C$. Particle A must be a stable (or long-lived nucleus) with no bound excited states. As noted in Chapter I, if a bound excited state $A^*$ exists the reaction $B + C \rightarrow A^* + \gamma$ followed by the decay $A^* \rightarrow A + \gamma$ can be experimentally confused with $B + C \rightarrow A + \gamma$, and might invalidate the reciprocity test. The possible target nuclei are p, n (in deuterium), d, $He^3$, t (half-life ~12 years), $He^4$ and $Li^6$. The possibilities for B and C are the same as for A with the addition of charged pions.

All reactions $B + C \rightarrow A + \gamma$ will be subject to the background $B + C \rightarrow A + \pi^o$. It will be much easier to eliminate the background if the beam particle B is charged, so that a beam of well-defined momentum may be used.

All reactions with a neutron target will actually have to be observed with a deuterium target, making a subtraction for the unwanted proton reaction. This is difficult and would tend to obscure the significance of the reciprocity test.

In all reactions $B + C \rightarrow A + \gamma$ in which B is a nucleus, there is a maximum laboratory angle for particle A, generally near $10^o$. Measurement of the extreme center of mass frame angles requires detection of particle A at very small lab angles. This is much easier with a beam of small spatial dimensions, which is simpler to obtain with a charged than with a neutral beam.

As discussed in Chapter I, any T-violation must involve the

production of a nucleon resonance, of which the $\Delta(1236)$ is the lightest. The $\Delta$ decays into a nucleon and a pion, so that if particle B (or C) is not a pion, a final state interaction is necessary to absorb the pion permitting B and C to be nuclei. It would appear that reactions with an external pion would have strongest contributions due to $\Delta$ production, and therefore provide the best test of T-invariance. However, all such reactions prove to be rather difficult experimentally. Of the reactions where B and C are both nuclei, I feel that reasonably strong $\Delta$ production can occur if the $\Delta$ can coexist with either B or C in an intermediate state; the only final state interaction needed is the absorption of a pion by the spectator nucleus.

We now consider the possible reactions in turn. The remarks apply to beam energies suitable for $\Delta$ production.

1. $\gamma + p \leftrightarrow n + \pi^+$

The forward reaction is probably the most well measured of all reactions under consideration. However, in inverse reaction, $\pi^+ + n \rightarrow p + \gamma$ is quite difficult for two reasons: (a) a deuterium target must be used, and (b) the protons have very low kinetic energy, equivalent to a range of only 0.1 gram at the worst angle. A complete angular distribution is impossible.

2. $\gamma + n \rightarrow p + \pi^-$

A deuterium correction must be made for the forward reaction, but this is somewhat simplified in that the entire final state can be measured and from this the neutron fermi momentum can be calculated. The inverse reaction has a neutral final state, and the neutrons

produced at large angles have low kinetic energies (15 MeV at $\theta_{C.M.} = 140^{o}$). Because of these experimental complications, it is hard to evaluate the presently observed[111] discrepancy in terms of a T-violation.

3. $\gamma + d \leftrightarrow n + p$

The forward reaction has been well measured, as mentioned in Chapter I. To eliminate backgrounds $\gamma + d \rightarrow n + p + \pi^{o}$ or $p + p + \pi^{-}$, either the neutron should be observed, or a 'synchrotron subtraction' performed. The inverse reaction must be performed with a neutron beam, which can be obtained with only fair momentum resolution.

4. $\gamma + He^{3} \rightarrow p + d$

Both the forward and inverse reactions are more accessible than for reactions (3) since the p and d are charged. Disadvantages are the lower cross-section and less prominent appearance of the $\Delta$. In observing the inverse reaction, it is advantageous to use a deuteron beam and a proton target rather than the opposite. This is because a deuteron beam of 900 MeV is needed for $\Delta$ production while a proton beam need only be 450 MeV. Therefore, the laboratory energies of the $He^{3}$ and $\gamma$ are much larger, and more easily observable, if a deuteron beam is used. The maximum lab angle for the $He^{3}$ is only $9^{o}$ in this case, so the deuteron beam must be well collimated if the small angle $He^{3}$ are to be detected.

5. $\gamma + He^{3} \leftrightarrow \pi^{+} + t$

While these reactions should have a large $\Delta$ production, they are difficult experimentally. In the forward reaction, the tritium must be detected to have confidence that the reaction occurred. However,

the maximum kinetic energy of the tritium is 50 MeV, and it would be almost impossible to measure a complete angular distribution. Likewise, in the inverse reaction the $He^3$ has a maximum energy of 53 MeV.

6. $\gamma + t \rightarrow n + d$

Measurement of the forward reaction would involve the radiation hazard of a tritium target. These reactions offer no advantages over reactions (3).

7. $\gamma + t \rightarrow \pi^- + He^3$

These reactions suffer from the same disadvantages of reactions (5), with the addition of the radiation safety problem.

8. $\gamma + He^4 \leftrightarrow p + t$

These reactions appear the most promising possibility for a new reciprocity test. Based on data[78] at $90^o$(c.m.), the cross-section is about 0.1 that of reactions (3), with an even more prominent 'bump' due to $\Delta$ production. The tritium is produced with fairly low energy ( 40 MeV) in the forward reaction, requiring care. For the inverse reaction it is advantageous to use a tritium beam (1200 MeV) rather than a proton beam. The maximum lab angle of the $He^4$ would then be $6.5^o$.

9. $\gamma + He^4 \leftrightarrow d + d$

While these reactions are quite accessible to experiment, they have a very low cross-section. The indistinguishability of the two spin-one deuterons forbids them from forming the $^1P_1$ state needed for electric dipole transitions. While this transition is probably not important for $\Delta$ production, the latter is suppressed by a complicated final-state interaction needed to absorb the decay pion internally.

An experiment[112] at a photon energy of 265 MeV reports a cross-section 60 times smaller than that for $\gamma + He^4 \rightarrow p + t$.

10. $\gamma + Li^6 \leftrightarrow d + He^4$

11. $\gamma + Li^6 \leftrightarrow He^3 + t$

While all of these reactions have measureable values of their kinematic parameters, it is unlikely that $\Delta$ production is very important in them as complicated final state interactions are necessary.

Based on this survey, I recommend the reactions $\gamma + He^4 \leftrightarrow p + t$ as the best candidate for an additional reciprocity test of T-invariance. They appear to have a strong signal due to $\Delta$ production and are experimentally tractable. Finally, as tritium is involved, they would be very 'hot' experiments.

## VII. FOOTNOTES AND REFERENCES


1. J. H. Christenson, J. W. Cronin, V. L. Fitch and R. Turlay, Phys. Rev. Letters 13, 138 (1964).
2. G. Lüders, Annals of Physics 2, 1 (1957).
3. J. Bernstein, G. Feinberg and T. D. Lee, Phys. Rev. 139, B1650 (1965).
4. The evidence for parity conservation is not at all conclusive for interactions involving virtual photons. A kinematic factor of $q^2$ ($q$ = 4-momentum of photon) in a possible parity violating amplitude suppresses any effect in most experiments. A search for an asymmetry in the inelastic scattering of polarized electrons with unpolarized protons would be the most sensitive experimental test of parity non-conservation independent of the question of time reversal violation.
5. Ernest M. Henley, Annual Review of Nuclear Science 19, 367 (1969).
6. S. Barshay, Phys. Rev. Letters 17, 49 (1966).
7. T. D. Lee, Phys. Rev. 140, B959 (1965).
8. L. B. Okun, Physics Letters 23, 595 (1966).
9. William B. Frazer, Phys. Rev. 150, 1244 (1966).
10. J. C. Keck and A. V. Tollestrup, Phys. Rev. 101, 360 (1956).
11. R. Kose, W. Paul, K. Stockhorst and K. H. Kissler, Zeitschrift für Physik 202, 364 (1967).
12. J. Buon, V. Gradco, J. Lefrancois, P. Lehmann, B. Merkel and P. Roy, Physics Letters 26B, 595 (1968).

13. D. I. Sober, D. G. Cassel, A. J. Sadoff, K. W. Chen and P. A. Crew, Phys. Rev. Letters 22, 430 (1969).

14. R. L. Anderson, R. Prepost and B. H. Wiik, Phys. Rev. Letters 22, 651 (1969).

15. D. F. Bartlett, C. E. Friedberg, K. Goulianos, I. S. Hammerman and D. P. Hutchinson, Phys. Rev. Letters 23, 893 (1969).

16. B. L. Schrock, J. F. Detoeuf, R. P. Haddock, M. J. Longo, K. K. Young, S. S. Wilson, D. Cheng, J. Sperinde and V. Perez-Mendez, in High-Energy Physics and Nuclear Structure, edited by S. Devons (Plenum Press, New York, 1970).

17. D. F. Bartlett, C. E. Frieberg, P. E. Goldhagen and K. Goulianos, Phys. Rev. Letters 27, 881 (1971).

18. Bryce L. Schrock, Roy P. Haddock, Jerome A. Helland, Michael J. Longo, Stephen S. Wilson, Kenneth K. Young, David Cheng and Victor Perez-Mendez, Phys. Rev. Letters 26, 1659 (1971).

19. A. Donnachie, in Proceedings of the 1971 International Symposium on Electron and Photon Interactions at High Energies, edited by N. B. Mistry (Laboratory of Nuclear Studies, Cornell University, 1972).

20. This statement is, however, a subject of controversy among nuclear physicists. For a recent summary of the experimental situation see K. H. Bray, S. N. Bunker, Mahavir Jain, K. S. Jayaraman, G. A. Moss, W. T. H. van Oers, D. O. Wells and Y. I. Wu, Phys. Rev. C3, 1771 (1970).

21. The 'range' array is so-called because it was originally intended

to observe the range of the particle in carbon. To this end, a sandwich of ten plates of carbon and ten wire chambers was constructed behind counter RS3 (Figure 2.4). However, most deuterons would never reach the sandwich. Further, the chambers proved troublesome. Data were taken with the sandwich when protons were detected in the range array, but not used in later analysis; the corresponding deuteron in the magnet was so clearly identified that the proton range information was superfluous. In a moment of imagination it was even conceived that the nuclear scattering of protons in the carbon might be used to obtain information on the spin polarization of the protons.

22. Alvin V. Tollestrup, CTSL Internal Report No. 31 (1967), unpublished.

23. Alvin V. Tollestrup and Ricardo Gomez, CTSL Internal Report No. 35 (1967), unpublished.

24. Charles Y. Prescott, CTSL Internal Report No. 38 (1968), unpublished.

25. Shiu-uh Cheng, Ph.D Thesis, CalTech (1970), unpublished.

26. J. R. O'Fallon, L. J. Koester, Jr., J. H. Smith and A. I. Yavin, Phys. Rev. 141, 889 (1966).

27. G. Goggi, G. C. Mantovani, A. Piazolli, D. Scannicchio, A. Piazza and R. Rinzivillo, Nuovo Cimento 58A, 901 (1968).

28. R. Guardiola and J. L. Sanchez-Gomez, Nuovo Cimento 1A, 243 (1971).

29. Leon Rochester, Ph.D Thesis, CalTech (1968), unpublished.

30. Joseph F. Janni, Technical Report AFWL-TR-65-150, National Techni-

cal Information Service, Springfield, Virginia (1966).

31. Fits for the (pp) and (np) cross-sections as a function of kinetic energy were made using data compiled by MacGregor et al[32]. The (pp) cross-section was fitted assuming the angular distribution to be flat using the value at $90^{o}$ (center of mass frame). This causes only about a 1% discrepancy between the fit and the criteria that the scattering occur at angles greater than $3^{o}$ or $5^{o}$. The total cross-section was used for (np) scattering. The coefficient $A^{-0.26}$ in the (pA) cross-section reflects the fact that roughly an $A^{2/3}$ dependence is to be expected. It was determined from proton-nucleus scattering data taken by Johansson et al[33], and is independent of the proton's kinetic energy in the range 10 - 600 MeV. The coefficient $1.2\ A^{-0.17}$ in the (nA) cross-sections holds only for A greater than 2; for A less than 2, it is 1.0. It was determined from the neutron-nucleus scattering data of Ashmore et al[34] and applies to neutron kinetic energies 10 - 350 MeV. In calculating the (dA) cross-sections from those for (pA) and (nA), the proton and neutron kinetic energies are taken as 1/2 that of the deuteron. The two factors 0.83 and 0.56 come from using the appropriate combinations of the elastic, inelastic and stripping cross-sections for deuteron-carbon scattering at 650 MeV given in reference 35; this is the only data in the literature containing the necessary information on deuteron-nucleus scattering. As most of the nuclear scattering in the experiment is due to carbon, the resulting fit should be

quite good.

32. Malcolm H. MacGregor, Richard A. Arndt and Robert M. Wright, UCRL-50426 (1968), unpublished.

33. A. Johansson, U. Svanberg and O. Sundberg, Arkiv für Physik 19, 527 (1961).

34. A. Ashmore, R. G. Jarvis, D. S. Mather and S. K. Sen, Proceedings of the Physical Society 70A, 745 (1957).

35. L. M. C. Dutton, J. D. Jafar, H. B. Van der Raay, D. G. Ryan, J. A. Stiegelmair and R. K. Tandon, Physics Letters 16, 331 (1965); J. D. Jafar, T. J. MacMahon, H. B. Van der Raay, D. H. Reading, K. Ruddick and D. G. Ryan, Nuovo Cimento 48A, 165 (1967); J. D. Jafar, H. B. Van der Raay, D. G. Ryan, J. A. Stiegelmair and R. K. Tandon, Nuclear Physics A161, 105 (1971).

36. M. L. E. Oliphant, P. Harteck and Lord Rutherford, Proceedings of the Royal Society A144, 692 (1934).

37. Fred Hoyle, Frontiers of Astronomy, (Mentor Books, New York, 1957) p. 68.

38. H. A. Bethe, Phys. Rev. 55, 434 (1938).

39. S. C. Curran and J. E. Strothers, Proceedings of the Royal Society A172, 72 (1939).

40. W. A. Fowler, C. C. Lauritsen, and A. V. Tollestrup, Phys. Rev. 76, 1767 (1949).

41. D. H. Wilkinson, Philosophical Magazine 43, 659 (1952).

42. G. M. Griffiths and J. B. Warren, Proceedings of the Physical Society A68, 781 (1955).

43. G. M. Griffiths, E. A. Larson and L. P. Robertson, Canadian Journal of Physics 40, 402 (1962).

44. G. M. Griffiths, M. Lal and C. D. Scarfe, Canadian Journal of Physics 41, 724 (1963).

45. W. Wölfli, R. Bösch, J. Lang, R. Müller and P. Marmier, Physics Letters 22, 75 (1966).

46. K. N. Geller, E. G. Muirhead and L. D. Cohen, Nuclear Physics A96, 397 (1967).

47. D. Bachelier, M. Bernas, I. Brissaud, C. Detraz, J. P. Didelez, H. Langevin-Joliot, J. Lee and P. Radvanyi, Physics Letters 21, 697 (1966); also in Few Body Problems, edited by Guy Paic and Ivo Slaus, (Gordon and Breach, New York, 1968).

48. J. P. Didelez, H. Langevin-Joliot, Z. Maric and V. Radojevic, Nuclear Physics A143, 602 (1970).

49. B. D. Belt, C. R. Bingham, M. L. Halbert and A. van Der Woude, Phys. Rev. Letters 24, 1120 (1970);
A. van Der Woude, M. L. Halbert, C. R. Bingham and B. D. Belt, Phys. Rev. Letters 26, 909 (1971).

50. L. I. Schiff, Phys. Rev. 52, 242 (1937).

51. Mario Verde, Helvitia Physica Acta 23, 453 (1950).

52. J. C. Gunn and J. Irving, Philosophical Magazine 42, 1353 (1951).

53. C. Rossetti, Nuovo Cimento 14, 1171 (1959).

54. U. Eichmann, Zeitschrift für Physik 175, 115 (1963).

55. K. Bösch, J. Lang, R. Müller and W. Wölfli, Physics Letters 15, 243 (1965).

56. V. N. Fetisov, Physics Letters 21, 52 (1966); Nuclear Physics A98, 437 (1967); Soviet Journal of Nuclear Physics 4, 513 (1966).

57. R. I. Dzhibuti, V. I. Mamasakhlisov and T. S. Macharadze, Soviet Journal of Nuclear Physics 2, 40 (1966).

58. C. M. Bailey, G. M. Griffiths and T. W. Donnelly, Nuclear Physics A94, 502 (1967); Physics Letters 24B, 222 (1967).

59. G. Barton, Nuclear Physics A104, 289 (1967).

60. I. M. Barbour and A. C. Phillips, Phys. Rev. Letters 19, 1388 (1967); Phys. Rev. C1, 165 (1970).

61. Benjamin F. Gibson, Nuclear Physics B2, 501 (1967).

62. J. M. Knight, J. S. O'Connell and F. Prats, Phys. Rev. 164, 1354 (1967).

63. J. S. O'Connell and F. Prats, Physics Letters 26B, 197 (1968).

64. N. J. Carron, Phys. Rev. 168, 1095 (1968).

65. J. S. Levinger and H. A. Bethe, Phys. Rev. 78, 115 (1950).

66. J. S. Levinger, Nuclear Photodisintegration, (Oxford University Press, London, 1960).

67. L. Cranberg, Bulletin of the American Physical Society 3, 173 (1958).

68. B. L. Berman, L. J. Koester and J. H. Smith, Phys. Rev. Letters 10, 527 (1963); Phys. Rev. 133, B117 (1964).

69. A. N. Gorbunov and A. T. Varfolomeev, Physics Letters 5, 149 (1963); Physics Letters 11, 137 (1964); Soviet Physics JETP 20, 20 (1965).

70. J. B. Warren, K. L. Erdman, L. P. Robertson, D. A. Axen and J. R. MacDonald, Phys. Rev. 132, 1691 (1963).

71. E. Finckh, R. Kosiek, K. H. Lindenberger, V. Meyer-Berkhout, N. Nücker and K. Schlüpmann, Physics Letters 7, 271 (1963).

72. C. Becchi, G. E. Manuzio, L. Meneghetti and S. Vitale, Physics Letters 8, 322 (1964).

73. V. N. Fetisov, A. N. Gorbunov and A. T. Varfolomeev, Nuclear Physics 71, 305 (1965).

74. J. R. Stewart, R. C. Morrison and J. S. O'Connell, Phys. Rev. 138, B372 (1965).

75. H. M. Gerstenberg and J. S. O'Connell, Phys. Rev. 144, 834 (1966).

76. P. Picozza, C. Schaerf and R. Scrimaglio, Nuovo Cimento 55A, 206 (1968).

77. G. Goggi, G. C. Mantovani, A. Piazzoli, D. Scannicchio, A. Piazza and R. Rinzivillo, Nuovo Cimento 58A, 902 (1968).

78. P. Picozza, C. Schaerf, R. Scrimaglio, G. Goggi, A. Piazzoli and D. Scannicchio, Nuclear Physics A157, 190 (1970).

79. B. L. Berman, S. C. Fultz and P. F. Yergin, Phys. Rev. Letters 24, 1494 (1970).

80. H. Bock and H. Walenta, Zeitschrift für Physik 238, 56 (1970).

81. F. L. Fabbri, P. Picozza and C. Schaerf, Nuovo Cimento Letters 3, 63 (1972).

82. Nancy M. O'Fallon, Louis J. Koester and James H. Smith, preprint, University of Illinois (1972).

83. The $90^{o}$ Points of References 33 and 73 were extracted from the total cross-sections and angular shape functions published in those papers.

84. H. Collard, R. Hofstadter, E. B. Hughes, A. Johannson, M. R. Yearian, R. B. Day and R. T. Wagner, Phys. Rev. 138, B57 (1965).

85. J. S. McCarthy, I. Sick, R. B. Whitney and M. R. Yearian, Phys. Rev. Letters 25, 884 (1970).

86. L. M. Delves and A. C. Phillips, Reviews of Modern Physics 41, 497 (1969).

87. R. D. Amado, Annual Review of Nuclear Science 19, 61 (1969).

88. C. W. Akerlof, W. H. Ash, K. Berkelman, C. A. Lichtenstein, A. Ramanauskas, and R. H. Siemann, Phys. Rev. 163, 1482 (1967).

89. A. Johansson, Phys. Rev. 136, B1030 (1964).

90. B. F. Gibson and G. B. West, Nuclear Physics B1, 349 (1967).

91. For an early version of this work, see Abraham Seiden, CTSL Internal Report No. 49, (1970), unpublished.

92. Malcolm H. MacGregor, Richard A. Arndt and Robert M. Wright, Phys. Rev. 169, 1128 (1968); 173, 1272 (1968).

93. R. L. Walker, Phys. Rev. 182, 1729 (1969).

94. J. S. Levinger, Phys. Rev. 84, 43 (1951).

95. See Reference 81.

96. Henry A. Thiessen, CTSL Internal Report No. 21, (1965), unpublished.

97. Steven J. Yellin, Ph.D Thesis, California Institute of Technology (1971).

98. Frank B. Wolverton, Manual for BPAKI, Thick Radiator Bremsstrahlung Computer Program (unpublished).

99. Donald E. Groom, CTSL Internal Report No. 12, (1964), unpublished.

100. R. Littauer, Review of Scientific Instruments 25, 148 (1954).

101. R. R. Wilson, Nuclear Instruments and Methods 1, 101 (1957).

102. Henry A. Thiessen and Jerome Pine, CTSL Internal Report 22, (1966), unpublished.

103. O. L. Meadors, Henry Asuki, (private communication).

104. Petroleum Analytical Research Corp., Houston, Texas.

105. The Properties of Liquid and Solid Helium, J. Wilks (Clarendon Press, Oxford, 1967).

106. John C. Wheatley, American Journal of Physics 36, 181 (1968).

107. J. R. Clement, E. H. Quinnell, M. C. Steele, R. A. Hein and R. L. Dolecek, Review of Scientific Instruments 24, 545 (1953).

108. C. Y. Prescott, S. U. Cheng and K. T. McDonald, Nuclear Instruments and Methods 76, 173 (1969).

109. See for example, F. Wolverton, CTSL Internal Report No. 36, (1968), unpublished.

110. See for example, Klaus G. Steffen, High Energy Beam Optics (Interscience Publishers, New York, 1965).

111. P. A. Berardo, R. P. Haddock, B. M. K. Nefkens, L. J. Verhey, M. E. Zeller, A. S. L. Parsons and P. Trudel, Phys. Rev. Letters 26, 201 (1971).

112. J. G. Asbury and F. J. Loeffler, Phys. Rev. 137, B1214 (1965).